HİTİT
UNIVERSITY

ISSN 2149-2123

JOURNAL OF SCIENCE & ENGINEERING

HITTITE

HJSE Official Journal of Graduate School of Natural & Applied Sciences, Hitit University www.hjse.hitit.edu.tr

Volume 1, Issue 1, 2014

www.hjse.hitit.edu.tr

HITTITE
JOURNAL OF SCIENCE & ENGINEERING

Hydrogen storage performance of synthesized compound was determined both experimentally and theoretically by using Materials Studio which is one of the molecular simulation software and adsorption measurement equipment.

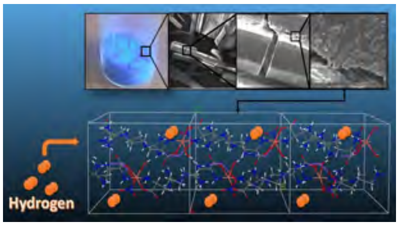

It was observed that midgut of the *Notonecta viridis* and *Notonecta maculata* are almost similar.

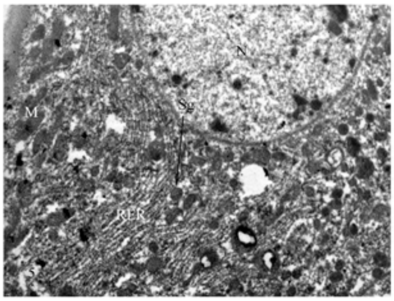

The cold water entering the heat exchanger at the inner channel flows across the fin and flows out at the inner channel. Such pin-fins show potential for enhancing the heat transfer rate in pin-fin cross flow heat exchangers.

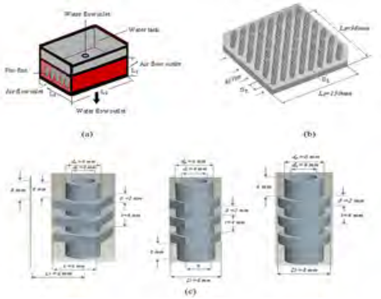

Improvements of the design and preparation of selective binding sites via metal coordination interactions in molecularly imprinted polymers (MIPs) is reviewed in this article.

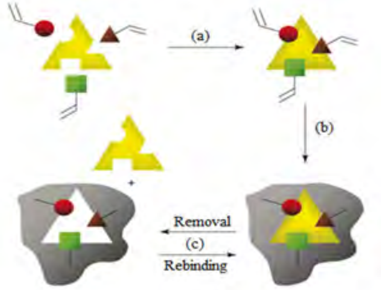

The power consumed by the compressor, heating capacity of indoor unit, the absorbing heat capacity of outdoor unit, coefficient of performance of the heat pump, suction and discharge pressures of the compressor were investigated according to the outdoor temperatures.

JOURNAL OF SCIENCE & ENGINEERING
HITTITE

Antioxidant and Antimicrobial Activities with GC/MS Analysis of the Morus alba L. Leaves 37-41

by Asiye Aslı Emniyet

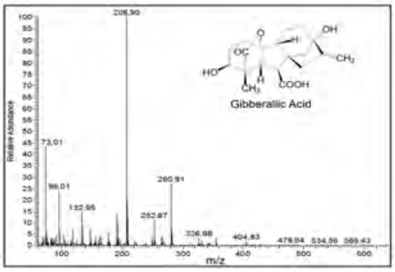

Several compounds analysed in ethanol extracts of *Morus alba* L. leaves with GC/MS technique. The antimicrobial and antioxidant activities were determined in extracts. So this research supports of using this plant leaves in some pharmacological and medical processes.

Separation and Purification of Lipase Using Cu Nanoparticle Embedded poly(HEMA-MATrp) Cryogels 43-50

by Kadir Erol

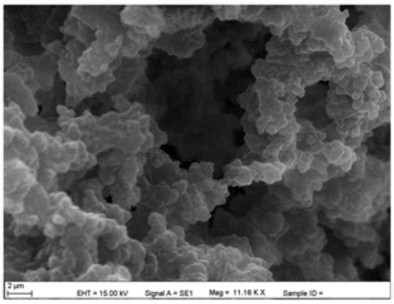

Cryogels have been quite extensively used as the adsorbents due to their macropores and interconnected flow channels. In this study, adsorption of lipase enzyme onto copper nanoparticles embedded poly(2-hydroxyethyl methacrylate-N-methacryloyl-L-tryptophan), poly(HEMA-MATrp) cryogels was studied.

Mixed Ligand Complexes of Acesulfame/Nicotinamide with Earth Alkaline Metal Cations MgII, CaII, BaII and SrII. Synthesis and Characterization 51-57

by Omer Yurdakul

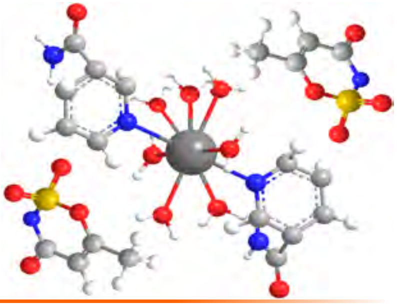

In the scope of this study, acesulfame (ace, acs)-nicotinamide (na) mixed ligand complexes of Mg(II), Ca(II), Sr(II) and Ba(II) were synthesized for the first time. Possible formulas for complexes were determined as $[Mg(H_2O)_4(na)_2](acs)_2$, $[Ca(H_2O)_6(na)_2](acs)_2$, $[Sr(H_2O)_7(na)_2](acs)_2$, $[Ba(H_2O)_7(na)_2](acs)_2$).

Owner
Prof. Dr. Reha Metin ALKAN
on behalf of Hitit University

Editor-in-chief
Prof. Dr. Ali Kılıçarslan

Associate Editors
Assoc. Prof. Dr. D.Ali Köse
Asst. Prof. Dr. Öncü Akyıldız

Production
Dr. Kazım Köse

Editor's Office
Tel: +90 364 227 45 33 / 12 36
Fax: +90 364 227 45 35
Email: alikilicarslan@hitit.edu.tr

Subscription Service:
Tel: +90 364 227 45 33 / 12 82
Fax: +90 364 227 45 35
Email: hjse@hitit.edu.tr

EDITORIAL BOARD

Dr. Mike Beckett	Bangor University, Bangor, England.
Dr. İbrahim Dinçer	Uoit Ontario University, Ontario, Canada.
Dr. Mohamad S. Quato	Central Michigan University, Michigan, USA.
Dr. Thanos Salifoglou	Aristotle University of Thessaloniki, Thessaloniki, Greece.
Dr. Wojciech Nogala	Polish Academy of Sciences, Poland
Dr. Yusuf Ayvaz	Süleyman Demirel University, Isparta, Turkey.
Dr. Adil Denizli	Hacettepe University, Ankara, Turkey.
Dr. Ali Gencer	Ankara University, Ankara, Turkey.
Dr. Metin Gürü	Gazi University, Ankara, Turkey.
Dr. Murat Hoşöz	Kocaeli University, Kocaeli, Turkey.
Dr. Sadık Kakaç	TOBB University of Economics and Technology, Ankara, Turkey
Dr. Tarık Ömer Oğurtanı	Middle East Technical University, Ankara, Turkey
Dr. Ender Suvacı	Anadolu University, Eskişehir, Turkey
Dr. Ali Topçu	Hacettepe University, Ankara, Turkey
Dr. Ali Kılıçarslan	Hitit University, Çorum, Turkey
Dr. Satılmış Basan	Hitit University, Çorum, Turkey
Dr. Vedat Deniz	Hitit University, Çorum, Turkey
Dr. Aydın Özlük	Hitit University, Çorum, Turkey
Dr. Menderes Suiçmez	Hitit University, Çorum, Turkey
Dr. Seçil Şatır	Hitit University, Çorum, Turkey
Dr. Abdurrahman Asan	Hitit University, Çorum, Turkey
Dr. Kazım Savaş Bahçeci	Hitit University, Çorum, Turkey
Dr. Naki Çolak	Hitit University, Çorum, Turkey
Dr. Faruk Gökmeşe	Hitit University, Çorum, Turkey
Dr. Hakan Güngüneş	Hitit University, Çorum, Turkey
Dr. Bülent Kabak	Hitit University, Çorum, Turkey
Dr. Dursun Ali Köse	Hitit University, Çorum, Turkey
Dr. İrfan Kurtbaş	Hitit University, Çorum, Turkey
Dr. Uğur Adnan Sevil	Hitit University, Çorum, Turkey
Dr. İbrahim Sönmez	Hitit University, Çorum, Turkey
Dr. Fatma Muazzez Şimşir	Hitit University, Çorum, Turkey
Dr. Dilber Esra Yıldız	Hitit University, Çorum, Turkey

Journal Name	: HITTITE JOURNAL OF SCIENCE AND ENGINEERING
Year	: 2014
Managing Editor	: Prof. Dr. Ali KILIÇARSLAN
Managing Office	: Hitit University Graduate School of Natural and Applied Sciences
Managing Office Tel	: +90 364 666 11 11
Publication Language	: English
Publication Type	: International Article
Delivery Format	: 2 times a year (semi-annually)
Print ISSN	: 2149-2123
Publisher	: Bir Medya
Publisher Address	: Yeniyol Mah. Gazi 12. Sok. No:9/13 ÇORUM
Publisher Tel	: +90 364 225 66 64

On behalf of the Editorial Board and my Associate Editors, I am very happy to announce the publication of the first issue of Hittite Journal of Science and Engineering (HJSE).

Almost two years ago, as the Graduate School of Natural and Applied Sciences (GSNAS) of Hitit University, we have begun the efforts to make HJSE. In every stage from the beginning to now, the president of Hitit University, Prof. Dr. Reha Metin Alkan and I (as the director of GSNAS and Editor-in Chief of HJSE) have regular meetings to discuss the issues regarding to the determination of the scope, structure, format of the journal and the related legal procedures. Firstly, the Editorial team consisting of the Editor-in-Chief, Associate Editors and Production Editor is decided to publish HJSE as an open-access online journal followed by a hard copy publication with a pre-determined format. Secondly, the Editorial Board members from the national and international universities were determined. Thirdly, our website (www.hjse.hitit.edu.tr) was officially launched and started to accept submissions online. Finally, printed booklets introducing HJSE were sent to the universities in Turkey and distributed in many national and international conferences. The electronic versions of these booklets were also sent by emails to the academic personnel of these universities.

All these efforts bear their fruit with this very first issue. The issue contains eight manuscripts from the disciplines of chemistry, biology, chemical engineering and mechanical engineering. These manuscripts were reviewed and corrected according to the reviewer's comments and the first issue of Hittite Journal of Science and Engineering was born. I would like to express my gratitude to all our authors and contributing reviewers.

First of all, I would like to thank to the President of Hitit University, Prof. Dr. Reha Metin Alkan, for supporting and motivating HJSE in every respect. Thanks are also due to the Associate Editors of HJSE, namely Dr. Dursun Ali Köse, for completing the legal procedures that are necessary for the publication of HJSE and contributing to the Editorial Board and Dr. Öncü Akyıldız, for designing and arranging the web site of HJSE in detail and to follow the editorial workflow required by the Open Journal Systems (OJS). Special thanks are due to our Production Editor, Dr. Kazım Köse for arranging the proofs of the papers submitted to the journal, designing the web site of HJSE and collaborating with Associate Editor Dr. Öncü Akyıldız.

I invite the researchers and scientists from all branches of science and engineering to join us by sending their best papers for publication in Hittite Journal of Science and Engineering.

Dr. Ali Kılıçarslan

Editor-in-Chief

Director of Graduate School of Natural and Applied Sciences of Hitit University

Hittite Journal of Science and Engineering, 2014, 1 (1) 01-05
ISSN NUMBER: 2149-2123
DOI: 10.17350/HJSE19030000001

Porous Metal-Organic Cu(II) Complex of L-Arginine; Synthesis, Characterization, Hydrogen Storage Properties and Molecular Simulation Calculations

Zeynel Ozturk[1,2*], Dursun Ali Kose[3], Abdurrahman Asan[1] and Goksel Ozkan[4]
[1] Hitit University, Department of Chemical Engineering, Corum, TURKEY
[2] Hitit University, Alternative Energy Systems and Biomedical Research Centre, Corum, TURKEY
[3] Hitit University, Department of Chemistry, Corum, TURKEY
[4] Gazi University, Department of Chemical Engineering, Ankara, TURKEY

ABSTRACT

Cu(II)-arginine coordination compound was synthesized and characterized by using DSC, DTA, EA, FT-IR, XRD, SEM and EDX analysis techniques and then the hydrogen storage properties were investigated. Hydrogen storage performance of synthesized compound was determined both experimental and theoretically by using Materials Studio which is one of the Molecular simulation software and adsorption measurement equipment. It is found out that the arginine compound uptakes approximately 1.2 wt. % experimentally and 0.8 wt. % theoretically hydrogen in 77K and 100 bars pressure. Also the surface characteristics was calculated and also the possible cites which could uptake hydrogen in a single lattice cell were determined. At the end of this research, in addition to drug and other applications of L-arginine, it is proved that could be used as a part of adsorbent for hydrogen storage application.

Article History:
Received: 2014/08/07
Accepted: 2014/12/25
Online: 2014/12/31

***Correspondence to**: Zeynel Ozturk*
Hitit University, Faculty of Engineering,
Department of Chemical Engineering,
Corum, Turkey
Tel: +90 (364) 226-4533 (1261)
Fax: +90 (364) 227-4535
E-Mail: zeynelozturk61@yahoo.com

Key Words:
Hydrogen Storage; Cu-II compound; L-Arginine; Coordination Compound; Molecular Simulation.

INTRODUCTION

Most known alternative to fossil fuel energy system is widely researched hydrogen economy in the other name hydrogen energy system [1]. The main obstacle to use hydrogen economy in daily life is to store hydrogen as an energy carrier, safely and economically [2-3]. In order to store hydrogen, compressed and liquid gas systems [4] have been being used but for safely and more profitable storage there are many choices such as, metal hydrides [5], carbon nanotubes [6-7], metal organic frameworks (MOFs) [8] which are needed to be improved. Some target values are set for storing acceptable amount of hydrogen to use in portable systems by US DOE (4.5 wt. % by 2007, 6 wt. % by 2010 and 9 wt. % by 2015) [9] and these target are being cited widely by international community. In order to reach the targets, researchers have been working on alternative storage medias and systems which are safe and widely useful for mobile applications like automobile and portable power systems. Weak forces act a great role in physical sorption (also called as physisorption) in solid hydrogen storage medias and reaches great numbers within low temperatures down to 77K. With common usage areas such like gas sorption [8], gas separation [10], catalyst [11-12]; MOFs have a great sorption ability for hydrogen. For instance, Yaghi and co-workers reported that IRMOF-1, IRMOF-8, IRMOF-11, IRMOF-18 and MOF-177 uptakes hydrogen wt.% 1.32, 1.5, 1.62, 0.89 and 1.25 respectively at 77K and 1 bar [13]. With reticular structure, Cu(II)-arginine complex could be called as a MOF structured complex. Too many MOF structured complex are synthesized by using metal or metal clusters with benzene di-, tri- (or more) carboxylic acids widely but amino acids are not used as building block. Amino acids are used for biological or pharmaceutical applications in general such as vascular effects of dietary of arginine or effects for immunity [14-15]. In addition to other applications, in this work a novel Cu(II)-arginine coordination compound is synthesized and characterized to use for hydrogen storage which is not used before, then the storage properties are calculated. To calculate hydrogen storage performances and surface area of synthesized materials molecular simulation calculation was employed which was previously performed by Han et al. and Cao et al. [16-17].

The main aim of the research was to investigate hydrogen storage capability of Cu(II) compound of arginine. And also to have feedbacks from the simulations to improve experimental set up.

EXPERIMENTAL

Throughout the experiments, all chemicals used for the synthesis were of reagent grade and $Cu(NO_3)_2.6H_2O$ and L-arginine (Sigma-Aldrich) were used as received. For the synthesis of Cu (II)-arginato complex firstly sodium-arginate salt was prepared by using arginine and $NaHCO_3$. After that $Cu(NO_3)_2.6H_2O$ solution was mixed with sodium-arginate solution and stirred for two hours. The dark blue complex was obtained after four weeks and then was filtered off and dried in air. A view of molecular structure of reagents and synthesized complex with the crystal reticular form is shown in Figure 1.

For characterization, FT-IR data was collected in the 400-4000 cm^{-1} wave number ranges. Thermal decomposition data was collected in the temperature range of 298-1173K under nitrogen atmosphere to investigate thermal stability. For the investigation of thermal stability TGA analysis was performed and also DTG and DTA data were collected simultaneously with TG data. In order to check the accuracy of suggested molecular structure elemental analysis for C, H and N was realized. To determine crystal structure of complex, single crystal sample was mounted on a glass fiber and XRD data collected with graphite-monochromated MoKα radiation at 296K by using STOE IPDSII diffractometer. SEM images captured by using Zeiss EVO 60 Scanning Electron Microscopy (SEM) and also electron dispersive spectroscopy (EDX) analysis actualized that the details are given in supplementary file. HPVA-100 (Micromeritics Instrument), volumetric hydrogen storage performance test station was used to determine hydrogen uptake value of complex experimentally. After 12 hours degas under vacuum and 373K temperature, sample was transferred to hydrogen storage test aperture. In eight different pressures which reaches up to 92 bars were the adsorption and desorption measurement steps. Molecular simulation software Materials Studio (MS) was used to calculate surface area and hydrogen storage performances. Sorption module with force fields gives almost the exact values when compared with the experimental measurements [18]. In this work, hydrogen uptake values are calculated for 77, 273 and 298K temperatures and 0-100 bar pressure range by using modified universal force field (UFF). The modification enables temperature dependent quantum effect on physical adsorption which was described by Dimitrakakis et al. [19] also the Lennard Jonnes parameters

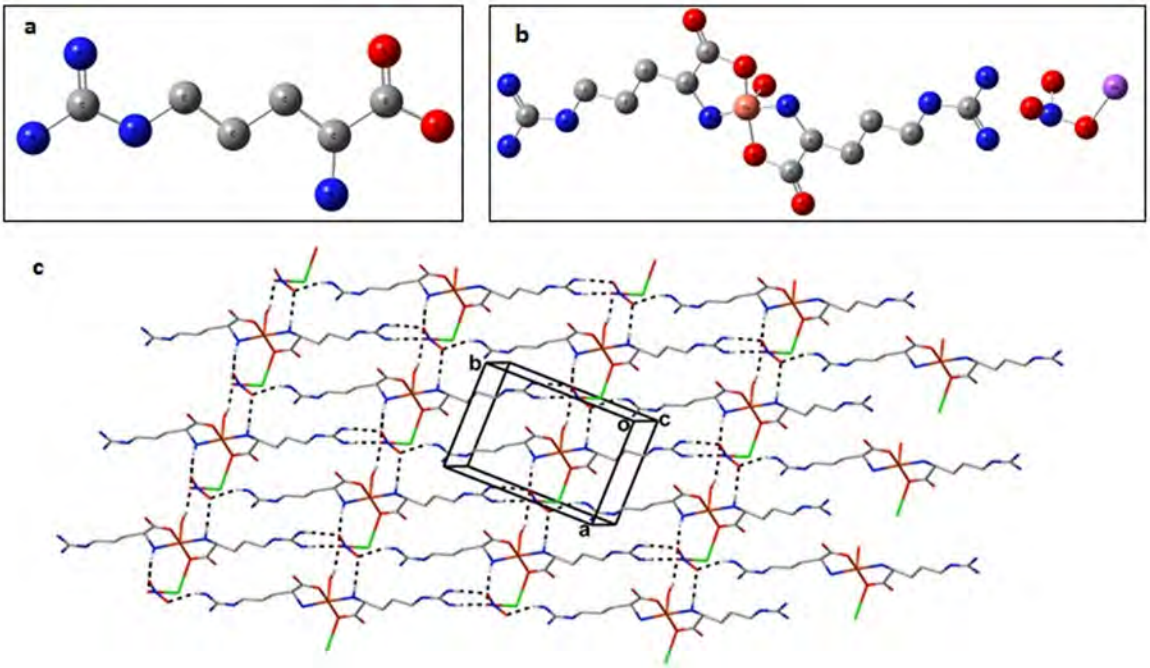

Figure 1. a) Molecular structure of arginate, b) general view of unit, c) crystal packing arrangement of complex.

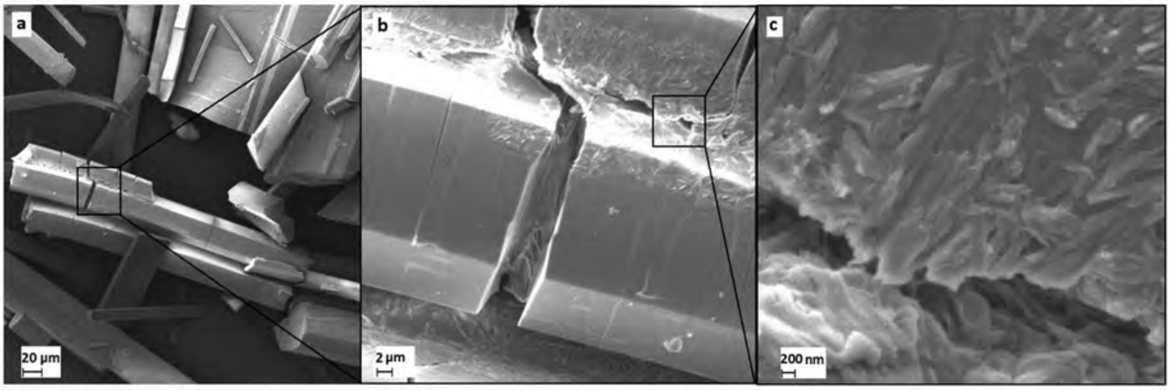

Figure 2. SEM images of complex a) in 500X, b) in 4000X and c) 20000X

are changed to 0.074 kcal/mol potential at 3.31 Å distance which was set previously by Fischer et al [20].

RESULTS AND DISCUSSION

It can be inferred from the IR spectra that the strong and broad absorption band in 3600-3000 cm^{-1} corresponds to asymmetric and symmetric stretching vibrations of aqua molecules. In the region of 1676 cm^{-1} and 1580 cm^{-1} strong coordination carboxylate group bands exhibit. The aim of thermal analysis study was not describing decomposition steps because of only stable temperature range was determined. According to TGA data approximately up to 473K, Cu complex of arginine was stable. Molecular formula was predicted as $[Cu(Arg)_2(H_2O)]NaNO_3$ and then confirmed by elemental analysis with 26.13(27.96), 5.12(5.83), 24.38(24.47) data for C, H and N contents found (calculated) % according to elemental analysis. According to crystallographic data, which is given in supplementary information in detail, $NaNO_3$ existence in crystal structure and the interactions via this molecule enables reticular form of crystal Perfect crystals are shown in Figure 2 which were captured and it is shown that the crystal packing or in the other word nanoparticles are not spherical or cubical geometry as like IRMOF-8 crystal or MIL-101TM crystals but poly crystalline [21-23].

The PCT diagram (Figure 3b) which seems like type 4 adsorption isotherm according to IUPAC classification [24]. According to experimental measurements, maximal uptake measured at the highest pressure which was 92 bars, 1.74 wt. % hydrogen at 77K (Figure 3a). The amount is also comparable to the common MOF structured materials for instance Li et al. [25] reported 3.42 and 2.05 wt. % hydrogen adsorption for Ni(II) and Co(II) based metal-organic coordination compounds at the same conditions. In another work, Yang et al. [26] reported that FMOF1 coded metal-organic structure constructed with Ag cluster was uptake 2.33 wt. % hydrogen at similar conditions.

Results for the molecular simulation calculations are shown in Figure 3b. As it is expected, the arginine compound

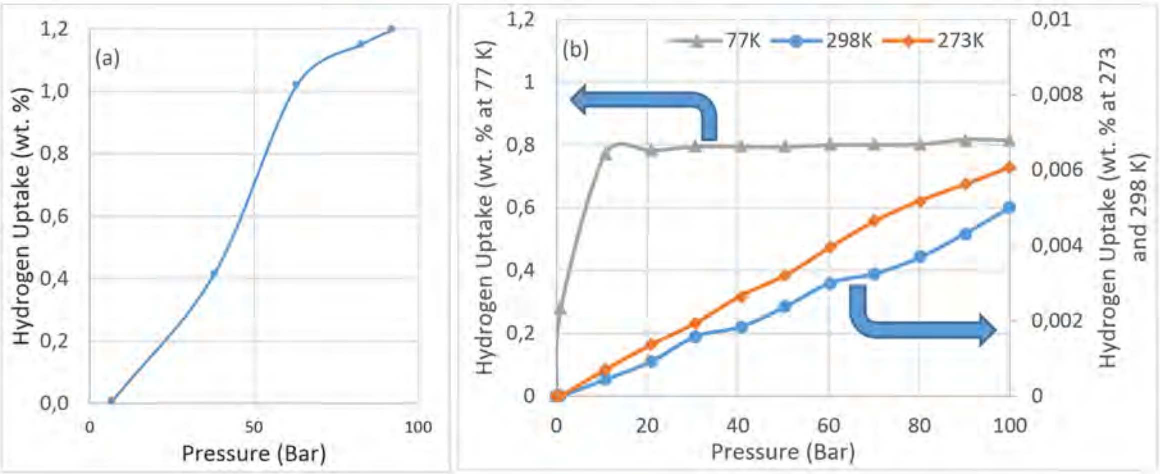

Figure 3. Hydrogen uptake isotherms, a) experimental data, b) simulated data

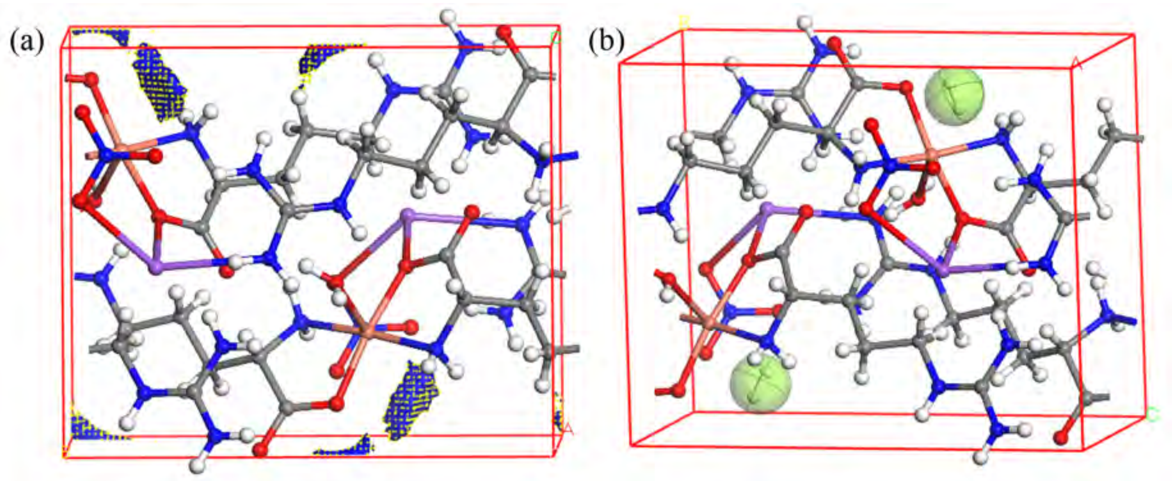

Figure 4. Possible places for hydrogen storage a) blue shells represent accessible solvent surface and b) green ellipsoids are the hydrogen molecules inside the unit cell.

uptakes maximum hydrogen at 77 K and 100 bars pressure, the amount was approximately 0.8 wt. % hydrogen. This value decreases with increasing temperatures which was 0.006 wt. % and 0.005 wt. % for 100 bars pressure, 273K and 373K respectively.

Surface area was calculated according to Solvent surface method with 0,15Å grid interval. By the way, the solvent surface area of single lattice was 16.68Å^2, in the common unit 97.47 m^2/g for nitrogen gas which has 1.097 Å van der Waals radii. Also the possible places for hydrogen storage in a single cell are simulated by using software and the places are almost similar which are given in Figure 4. Small surfaces in Figure 4.b are the places that could not store hydrogen because the radius of hydrogen is not convenient for those places.

CONCLUSIONS

Cu(II)-arginine complex as hydrogen storage material, was synthesized and characterized. Then its storage performance was determined. It is found out that the arginine which is an amino acid, uptakes acceptable amount of hydrogen when used as ligand in compound. In addition to its other applications hydrogen storage application of L-arginine amino acid shows average performance with 0.75wt.% in 77K-100 bars pressure theoretically and 1.7461 wt.% in 77K-92.02 bars experimentally. In such performances for meso-porous materials, it is possible to face differences between experimental measurements and theoretical calculations depends on force fields for simulations and spillover effect for experiments [27].

In conclusion, using an amino acid to synthesize coordination compound that is used for hydrogen storage in special conditions maybe is not the best application but if it is compared to other MOF structured coordination compound amino acids shows acceptable performance.

[CCDC 796731 contains the supplementary crystallographic data for this paper. These data can be obtained free of charge from The Cambridge Crystallographic Data Centre via www.ccdc.cam.ac.uk/data request/cif.]

ACKNOWLEDGEMENTS

We acknowledge to UNIDO-ICHET for their support and Hitit University Scientific Research Project Fund with the project number of MUH19001.14.003.

REFERENCES

1. Crabtree GW, Dresselhaus MS, Buchannan MV. The Hydrogen Economy. Physics Today 57 (2004) 39–46.
2. Rowsell JLC, Yaghi OM. Strategies for Hydrogen Storage in Metal-Organic Frameworks. Angewandte Chemie 44 (2005) 4670-4679.
3. Muradov NZ, Veziroglu TN. From hydrocarbon to hydrogen-carbon to hydrogen economy. International Journal of Hydrogen Energy 30 (2005) 225–237.
4. Zuttel A. Materials for hydrogen storage. Materials Today 6 (2003) 24–33.
5. Bogdanovic B, Schwickardi M. Ti-doped alkali metal aluminium hydrides as potential novel reversible hydrogen storage materials. Journal of Alloys and Compounds 253 (1997) 1–9.
6. Dillon AC, Jones KM, Bekkedahl TA, Kiang CH, Bethune DS, Heben MJ. Storage of hydrogen in single-walled carbon nanotubes. Nature 386 (1997) 377–379.
7. Ozturk Z, Baykasoglu C, Celebi AT, Kirca M, Mugan A. Hydrogen storage in heat welded random CNT network structures. International Journal of Hydrogen Energy 40 (2015) 403–411.

8. Hu YH, Zhang L. Hydrogen storage in metal-organic frameworks. Advanced Materials 22 (2010) E117–E130.
9. U.S. Department of Energy, EERE, Hydrogen, Fuel cells & Infrastructure Technologies Program,Multi–Year RD&D Plan, 2005. http://www.eere.energy.gov/hydrogenandfuelcells/mypp/pdfs/storage.pdf
10. Li JR, Kuppler RJ, Zhou HC. Selective gas adsorption and separation in metal-organic frameworks. Chemical Society Reviews 38 (2009) 1477–1504.
11. Luzan SM, Talyzin AV. Hydrogen adsorption in Pt catalyst/MOF–5 materials. Microporous and Mesoporous Materials 135 (2010) 201–205.
12. Fu Y, Su D, Chen Y, Huang R, Ding Z, Fu X, Li Z. An Amine–Functionalized Titanium Metal-Organic Framework Photocatalyst with Visible–Light–Induced Activity for CO_2 Reduction. Angewandte Chemie 14 (2012) 3364-3367.
13. Rowsell JLC, Milward AR, Park KS, Yaghi OM. Hydrogen Sorption in Functionalized Metal–Organic Frameworks. Journal of the American Chemical Society 126 (2004) 5666–5667.
14. Prelli RB, Klevin KP, Herrington DM. Vascular effects of dietary l–arginine supplementation. Atherosclerosis 162 (2002) 1–15.
15. Nieves JrC, Langkamp–Henken B. Arginine and immunity: a unique perspective. Biomedicine & Pharmacotherapy 56 (2002) 471–482.
16. Han SS, Goddard WA. Lithium–doped metal–organic frameworks for reversible H2 storage at ambient temperature. Journal of the American Chemical Society 129 (2007) 8422–8423.
17. Cao D, Lan J, Wang W, Smit B. Lithium–doped 3D covalent organic frameworks: high–capacity hydrogen storage materials. Angewandte Chemie International Edition in English 48 (2009) 4730–4733.
18. Wood BCD, Tan B, Trewin A, Su F, Rosseinsky MJ, Bradshaw D, Sun Y, Zhou L, Cooper I. Microporous Organic Polymers for Methane Storage. Advanced Materials 20 (2008) 1916–1921.
19. Dimitrakakis GK, Tylianakis E, Froudakis GE. Pillared Graphene: A New 3–D Network Nanostructure for Enhanced Hydrogen Storage. Nano Letters 8 (2008) 3166–3170.
20. Fisher M, Hoffmann F, Fröba M. Preferred Hydrogen Adsorption Sites in Various MOFs–A Comparative Computational Study. ChemPhysChem 10 (2009) 2647–2657.
21. Wang CY, Tsao CS, Yu MS, Liao PY, Chung TY, Wu HC, Miller MA, Tzeng YR. Hydrogen storage measurement, synthesis and characterization of metal-organic frameworks via bridged spillover. Journal of Alloys and Compounds 2008. doi:10.1016/j.jallcom.2009.11.203.
22. Yang J, Zhao Q, Li J, Dong J. Synthesis of metal-organic framework MIL–101 in TMAOH–$Cr(NO_3)_3$–H_2BDC–H_2O and its hydrogen–storage behavior. Microporous and Mesoporous Materials (2009). doi:10.1016/j.micromeso.2009.11.001.
23. Chen H, Lin SL. A combined experiment and molecular dynamics simulation study on the influence of the crosslinking on the crystallization of comb fluorinated acrylate copolymers. Journal of Materials Science 49 (2014) 986–993.
24. Recommendations: Reporting Physisorption Data for Gas/Solid Systems with Special Reference to the Determination of Surface Area and Porosity, IUPAC Commission on Colloid and Surface Chemistry Including Catalysis, Pure Applied Chemistry 57 (1985) 603.
25. Recommendations for the Characterization of Porous Solids, IUPAC Commission on Colloid and Surface Chemistry, Pure Applied Chemistry 66 (1994) 1311.
26. Li Y, Xie L, Yang R, Li X. Favorable Hydrogen Storage Properties of M(HBTC)(4,4′–bipy)•3DMF (M = Ni and Co). Inorganic Chemistry 47 (2008) 10372–10377.
27. Yang C, Wang X, Omary MA. Fluorous Metal–Organic Frameworks for High–Density Gas Adsorption. Journal of the American Chemical Society 129 (2007) 15454–15455.
28. Assfour B, Leoni S, Yurchenko S, Seifert G. Hydrogen storage in zeolite imidazolate frameworks. A multiscale theoretical investigation. International Journal of Hydrogen Energy 36 (2011) 6005–6013.

Hittite Journal of Science and Engineering, 2014, 1 (1) 07-11
ISSN NUMBER: 2149-2123
DOI: 10.17350/HJSE19030000002

Investigation of Midgut's Ultrastructure of *Notonecta viridis* Decourt, 1909 and *Notonecta maculata* Fab., 1794 (Hemiptera: Notonectidae)

Menderes Suicmez and Rana Ozmen
Hitit University, Department of Molecular Biology and Genetics, Corum, TURKEY

ABSTRACT

In this study, midgut's ultrastructure of the *Notonecta viridis* and *Notonecta maculata* was examined under transmission electron microscope (TEM). It was observed that midgut of the *Notonecta viridis* and *Notonecta maculata* are almost similar. Digestive canal is divided into three parts as foregut, midgut and hindgut. Midgut is wider and longer part than other parts of digestive canal. Midgut's heamasoel side is covered with muscular tissue and connective tissue and lumen side is covered with epithelial tissue. Epithelial layer consists of three different cells: Endocrine cells, regenerative cells and enterocytes cells. Endocrine cells possess secretory granules in the cytoplasm and they have the basement membrane folding in basal. Regenerative cells are small undifferentiated cells which are responsible for cellular regeneration. Enterocyte cells have many mitochondria and deep basal membrane folding in basal.

Article History:
Received: 2014/08/18
Accepted: 2014/11/19
Online: 2014/12/31

***Correspondence to**: Menderes Suicmez,*
Hitit University, Faculty of Arts and Science, Department of Molecular Biology and Genetics, Corum, Turkey
Tel: +90 (364) 227-7000 (1669)
Fax: +90 (364) 227-7005
E-Mail: menderessuicmez@hitit.edu.tr

Key Words:
Notonecta viridis; *Notonecta maculata*; Midgut; Ultrastructure

INTRODUCTION

Apparently, since insects have so many species and perceived as harmful organisms, it has brought to mind the idea of avoidance of these organisms and fighting with them. Insects which we accept both harmful as well as beneficial even have important functions in maintaining the ecological balance [1]. Insect body is divided into three parts as head, thorax and abdomen. Head segments are completely fused and the boundaries of segments cannot be distinguished in adults [2].

In generally, insects get their nutrients by biting-chewing or sucking but internal parasite larvae get their nutrients through the body surface. Types of diet and food types of insects are as follows feeding with various parts of plants (herbivores), feeding with peat moss (saprophytes), feeding with small insects or other animals, feeding with fungi and bacteria, feeding with feces, carrion and blood, and those feeding with the filtrate.

Digestive canal of insects is divided into three parts as front, middle and last intestine. Pre and post intestine is ectodermic and coated with chitin-cuticle but midgut is endoderm origin and not coated [3]. *Notonecta viridis* and *Notonecta maculata* (Hemiptera: Notonectida) are capable of feeding predators and this situation impede excessive reproduction of other insects in the aquatic environment. Because these species are fed everyday by eating 24-28 mosquito larvae, they help to provide the balance of food chain in the aquatic environment. So, by preventing excessive reproduction of mosquitoes, they have an important place as ecological for the reduction of the demand for insecticides [1].

MATERIAL AND METHOD

Specimens were placed in 3% glutaraldehyde in 0.1 M phosphate buffer at pH 7.2 for 3 h at room temperature. After rinsing in phosphate buffer, the specimens were postfixed in 1% buffered osmium

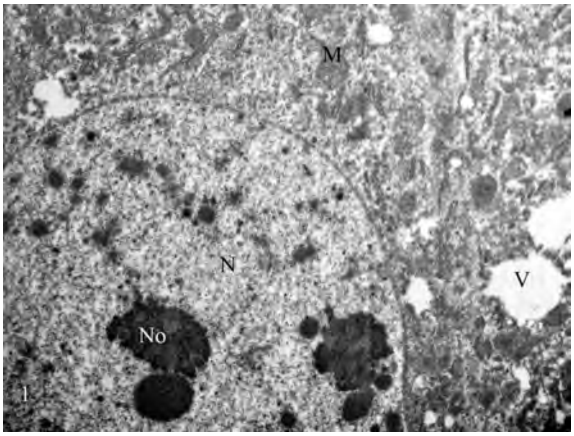

Figure 1. *Enterocyte cell in the midgut of N. maculata*; **No:** Nucleolus, **M:** Mitochondria, **N:** Nucleus, **V:** Vacuol (TEM, x 6 000)

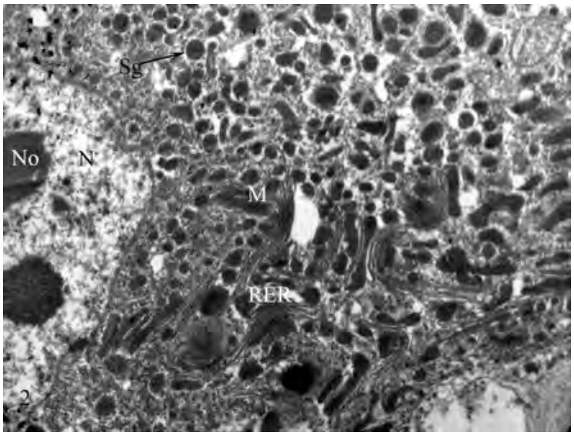

Figure 2. *Enterocyte cell in the midgut of N. viridis*. **No:** Nucleolus, **N:** Nucleus **Sg:** Secretory granules, **M:** Mitochondria, **RER:** Rough endoplasmic reticulum (TEM, x8 000)

tetroxide at pH 7.2 for 3 h at 4 °C. They were then dehydrated and embedded in araldite. Thin sections were stained with uranyl acetate and lead citrate [4] and examined using a Zeiss Libra120 electron microscope.

RESULTS

The digestive canal of *N. maculata* and *N. viridis* consists of foregut, midgut and hindgut like other Hemiptera. Foregut consists of eosophagus and partially enlarged proventriculus. Midgut found in the abdomen is wider and longer from other parts of the digestive canal. Hindgut has many folds in the abdomen. The total length of the digestive canal is 1.5 to 2 times than the length of insects. Morphologically, digestive canals of both species are seen similar. Midgut is surrounded by a single layer of epithelial tissue from inside and by a layer of muscle and connective tissue from outside. Midgut epithelium consists of three different cell types such as endocrine cells, enterocytes and regenerative cells. It is seen that they are almost similar to each other considered to the ultrastructure of epithelial cells of *N. viridis* and *N. Maculata*. A large and smooth nucleus and non-homogenously distribute chromatin in the nucleus are seen in the enterocytes cells of *N. maculata*. The same nucleus type, in a similar manner, is seen at *N. viridis*. However, more intense amounts of intracellular inclusions are seen in the enterocytes cells of *N. viridis* and the density of intracellular mitochondria is almost equal to each other (Figures 1 and 2).

Regenerative cells exist in epithelial tissue separately or in groups in basal position round or oval-shaped cells that are responsible for cellular regeneration contain rough endoplasmic reticulum and mitochondria which are not very dense within the cell. The chromatin shows a homogeneous dissemination and there are obvious nucleoli in nucleus. It is observed that basal membrane foldings extending into the cell in basal portion (Figures 3 and 4).

The most significant content is the secretory granule in endocrine cells of the intestine of these two species feeding

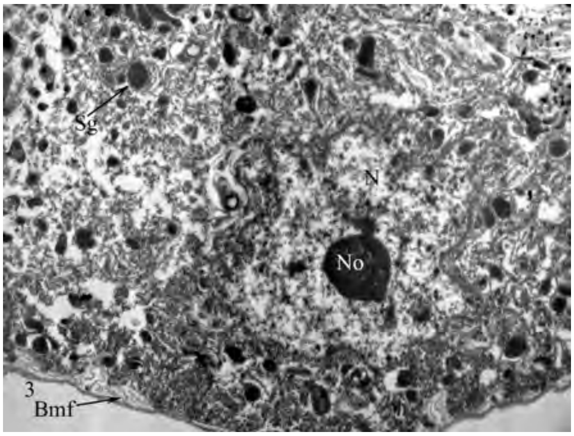

Figure 3. Regenerative cell in the midgut of N. maculata **N**: Nucleus, **Bmf**: Basal membrane folding, **No**: Nucleolus, **Sg**: Secretory granule (TEM, X6000)

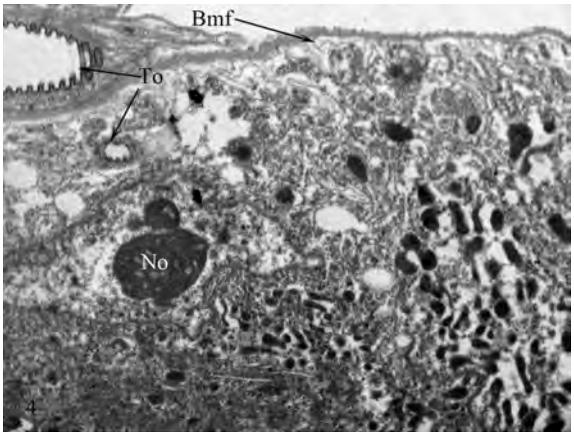

Figure 4. Regeneratif cell in midgut of *Notonecta viridis*. **Bmf:** Basal membrane folding, **No:** Nucleolus, **To**: Tracheol (TEM, X 8 000).

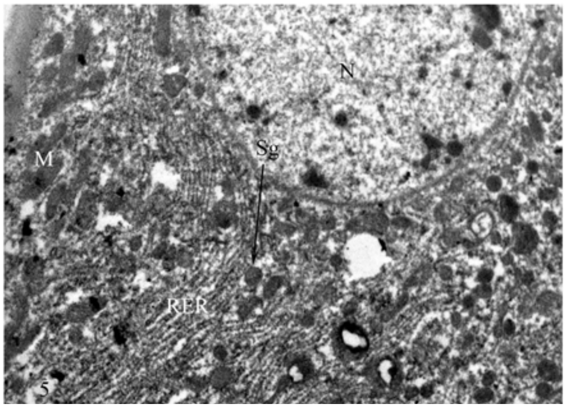

Figure 5. Endocrine cell in midgut of N. maculata. **Sg**: Secretory granule, **RER**: Rough endoplasmic reticulum, **M**: Mitochondria, **N**: Nucleus (TEM, X 8 000)

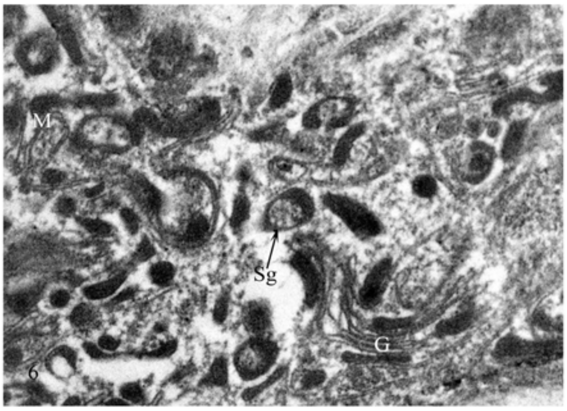

Figure 6. Endocrine cell in midgut of *N. maculata.* **M:** Mitochondria, **Sg:** Secretory granüle, **G:** Golgi apparatus (TEM, X 16 000)

with animal foods. Furthermore, the cell is seen very rich in terms of mitochondria and rough endoplasmic reticulum (Figure 5 and 6). Vacuole-like structures and also Golgi apparatus are observed in the cells. Mitochondria and the density of rough endoplasmic reticulum are higher than other cell types.

It is observed that *N. viridis*' endocrine cells are much more intense endoplasmic reticulum (Figure 7). It is observed density of basal membrane foldings in basal portions of these cells and there are mitochondria between these basal membrane foldings (Figure 8).

The reason of both enterocytes and endocrine cells contain secretory granules in greater amounts is probably duo to their tasks related to digestive and secretory. Both enterocytes and endocrine cells contain secretory granules in greater amounts since probably making tasks are related to digestive and secretory. These secretory granules are spread approximately the same amount on each side of the cell.

DISCUSSION

The digestive canal of *N. viridis* and *N. maculata* contains similar structures as in many species of Hemiptera which are searched before. However, Barber et al. [5] reported that midgut consists of four parts including the first, second, third and fourth ventriculus and there are Malpighian tubules at the junction of the midgut and last intestine.

The midgut epithelium consists of regenerative cells, enterocyte cells and endocrine cells as reported by Demir and Suiçmez [6]. As stated in many studies [7-12], we have observed significantly larger nucleus, nucleolus and the RER cisternae in the cytoplasm of the midgut cells of both species.

Several authors [7, 8, 10, 14-18] reported the existence of enterocytes cells responsible for absorption which were observed in the midgut of *N. maculata* and *N. viridis*.

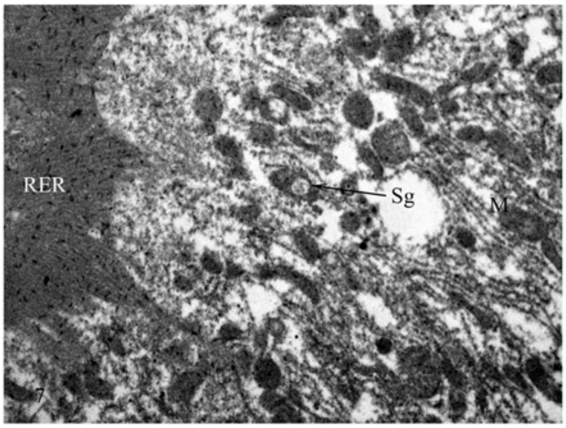

Figure 7. Endocrine cell in midgut of *N. viridis.* **Sg:** Secretory granule, **RER:** Rough endoplasmic reticulum, **M:** Mitochondria (TEM, x10 000)

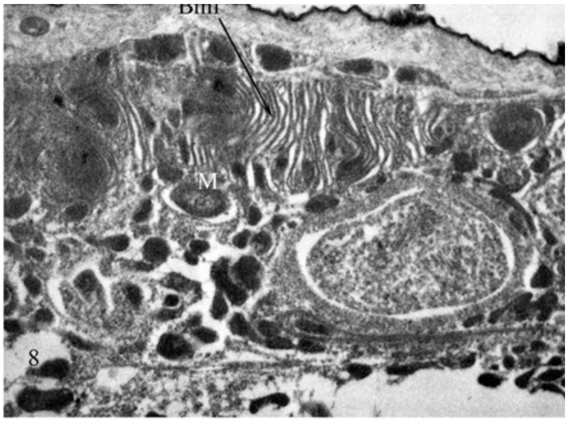

Figure 8. Endocrine cell in midgut of *N. viridis.* **M:** Mitochondria, **Bmf:** Basal membrane folding (TEM, x10 000)

The nucleus of *N. maculata* enterocyte cells are quite large and smooth and cover a large portion of the cell as indicated by Fialho et al., Hung et al. [8, 15]. Nucleus has a few nucleoli as stated by Rost-Roszkowska and Undrul [17] and nucleolus are seen significantly in the nucleus as stated by Gül et al. [14].

A large number of rough endoplasmic reticulum surrounded by mitochondria were observed in the cytoplasm of enterocyte cells in *N. maculata* and *N. viridis* as reported by authors [6-8, 11, 12, 15, 17, 19].

Glycogen granules and spherical crystals weren't able to mark which were observed before [7, 8]. Ferritin granules and large lysosomal bodies weren't detected either as mentioned by Taha et al. [20]. In enterocyte cells, Golgi apparatus couldn't be observed clearly in any other region of the midgut as indicated by Nardi et al. [19]. Transparent electron vesicles which were stated by Billen and Buschinger, Rost-Roszkowska and Undrul [16, 17] could not be observed in a very clear way in our study.

We observed the digestive cells and regenerative cells that can differentiate into endocrine cells in the study of both species we dealt, as stated by other authors [6, 7, 11, 12, 15, 19]. Hung et al. and Levy et al. supported that a large number of basal membrane infoldings, which are formed by invaginations made into the cells of the basal membrane of regenerative cells, are associated with mitochondria [11,15]. Rough Endoplasmic Reticulum and Smooth Endoplasmic Reticulum cisternae that were mentioned by Hung et al., Levy et al. and Nardi et al. [11, 15, 19] were also observed in the cells of both species we examined. Hung et al. indicated that there are no microvilli extensions in the apical parts of these cell types [15]. During the differentiation epithelium of midgut, it couldn't observe phosphate and Urospherite structures which contains carbonate chloride but non-uric acid as confirmed by Rost-Roszkowska and Undrul [17].

As Habibi et al. mentioned endocrine cells are shorter than the enterocyte cells and have no microvilli extensions in the apical parts as in enterocytes cells [13]. There are more secretory granules in endocrine cells than in other cells [6,12,14,21]. It suggests that these cells are specialized cells to make secretion. It is supported by Rost-Roszkowska et al. that very obvious basal membrane foldings are seen in the basal portion endocrine cells [21]. Rost-Roszkowska et al. and Demir and Suiçmez reported that these cells are directly related to the synthesis and secretion functions since they contain well-developed rough endoplasmic reticulum and mitochondria [6, 21].

CONCLUSIONS

N. viridis and *N. maculata* are aquatic insects and maintain their presence in the aquatic environment. These insects which meet their food from aquatic organisms also fulfill important functions in maintaining the ecological balance. As we mentioned earlier; these insect species consume the mosquito larvae as nutrient and this prevents their excessive proliferation and they can provide their population remain in balance in that region.

Thanks to these features, they have an important place to combat mosquitoes as an alternative way. Because these species are predators, they control the population of the species and also prevent their excessive proliferation. However, it's an inevitable reality that they are either directly or indirectly affected from the adverse changes in their environment. When evaluated with this aspect these species are also used as indicator organisms in the aquatic environment which they live. There are too many chemicals in soil and water as a result of so many agricultural activities. These chemicals are getting through to organisms in various ways. It will be impossible to sustain their existence over time as *N.viridis* and *N. maculata* are also negatively affected by these chemicals as in other organisms.

ACKNOWLEDGEMENTS

This research was supported by the Hittite University Scientific Research Projects (Project No. FEF03.10.003). We are indebted to the Hitit Universty Scientific Research Projects for financial support of this research. I also express thanks to Mr. Mehmet Aydınkal for correcting the English of the manuscript. I specially thank Prof. Dr. Mustafa Duran, who identified the species.

REFERENCES

1. Aldemir A, Boşgelmez A. *Alburnus orontis* (Cypriniformes:Cyprinidae) ve *Notonecta viridis* (Hemiptera: Notonectidae)'in Sivrisinek Larvaları Üzerindeki Predasyonu. Doktora Tezi, Kafkas Üniversitesi Fen–Edebiyat Fakültesi, Biyoloji Bölümü, Kars. Hacettepe Üniversitesi Fen Fakültesi, Biyoloji Bölümü, Ekoloji ABD, Beytepe, Ankara. 2003.
2. Demirsoy A, Türkan İ, and Gündüz, E. Genel Biyoloji. Palme Yayıncılık, Ankara, 2011.
3. Salman S. Omurgasız Hayvanlar Biyolojisi, Palme Yayıncılık, Ankara, 2006.
4. Ozban N, Özmutlu Ö. Mikropreparasyon Yöntemleri. İ.Ü. Fen Fakültesi Yayınlarından, İstanbul, 1991.

5. Barber Dan T,Cooksey Lynita M, Abell, Dawid W. A Study of the Anatomy of the Alimentary Canal of *Brochymena quadripustulata* (Hemiptera: Pentatomidae), Arkansas Academiy of Science Proceedings 34 (1980) 16–18.
6. Demir F, Suiçmez M. Investigation of Digestive Tract of *Sphex flavipennis* Fabrius, 1793 (Hymenoptera: Sphecidae): Morphology and Ultrastructure. Gazi University Journal of Science GU J Science 24(3) (2011) 397–405.
7. Rocha LLV, Neves CA, Zanuncio JC, Serrao J.E. Digestive Cells in the Midgut of *Triatoma vitticeps* (Stal, 1859) Different Starvation Periods. Comptes Rendus Biologies 333 (2010) 405-415.
8. Fialho MCQ, Zanuncio JC, Neves CA, Ramalho FS, Serrão JE. Ultrastructure of the Digestive Cells in the Midgut of the Predator *Brontocoris tabidus* (Heteroptera: Pentatomidae) After Different Feeding Periods on Prey and Plants. Annals of the Entomological Society of America 102(1) (2009) 119–127.
9. Rost–Roszkowska MR, Kubala KA, Nowak B, Pilarczyk S, Klag J. Ultrastructure of Alimentary Tract Formation in Embryos of Two Insect Species: *Melasoma saliceti* and *Chrysolina pardalina* (Coleoptera, Chrysomelidae). Arthropod Structure & Development 36 (2007) 351–360.
10. Bution Murillo L, Caetano FH. The Midgut of *Cephalotes* ants (Formicidae: Myrmicinae): Ultrastructure of the Epithelium and Symbiotic Bacteria. Micron 41 (2010) 448-454.
11. Levy SM, Falleiros AMF, Gregórıo EA, Arrebola NR, Toledo LA. The Larval Midgut of *Anticarsia gemmatalis* (Hübner) (Lepidoptera: Noctuidae): Light and Electron Microscopy Studies of the Epithelial Cells. Brazilian Journal of Biology 64(3B) (2004) 633–638.
12. Pinheiro DO, Silva MD, Gregório EA. Mitochondria in the Midgut Epithelial Cells of Sugarcane Borer Parasitized by *Cotesia flavipes* (Cameron, 1891). Brazilian Journal of Biology 70 (2010) 163–169.
13. Habibi J, Coudron TA, Backus EA, Brandt SL, Wagner RM, Wright MK, Huesing JE. Morphology and Histology of the Alimentary Canal of *Lygus hesperus* (Heteroptera: Cimicomoropha: Miridae). Annals of the Entomological Society of America 101(1) (2008) 159–171.
14. Gül N, Sayar H, Özsoy N, Ayvalı C. A Study on Endocrine Cells in the Midgut of *Agrotis segetum* (Denn.and Schiff.) (Lepidoptera:Noctuidae). Turkish Journal of Zoology 25 (1999) 193–197.
15. Hung C, Lin T, Lee W. Morphology and Ultrastructure of the Alimentary Canal of the Oriental Fruit Fly, *Bactrocera dorsalis* (Hendel) (Diptera: Tephritidae) (2) The Structure of the Midgut. Zoological Studies 39(4) (2000) 387–394.
16. Billen J, Buschinger A. Morphology and Ultrastructure of a Specialised Bacterial Pouch in the Digestive Tract of *Tetraponera* Ants (Formicidae, Pseudomyrmecinae). Arthropod Structure & Development 29 (2000) 259–266.
17. Rost–Roszkowska MM, Undrul A. Fine Structure and Differentiation of the Midgut Epithelium of *Allacma fusca* (Insecta: Collembola: Symphypleona). Zoological Studies 47(2) (2008) 200–206.
18. Neves CA, Gitirana LB, Serrão JE. Ultrastructure of the Midgut Endocrine Cells in *Melipona quadrifasciata anthidioides* (Hymenoptera, Apidae). Brazilian Journal of Biology 63(4) (2003) 683–690.
19. Nardi BJ, Miller LA, Bee CM, Lee RE Jr, Denlinger DL. The Larval Alimentary Canal of the Antarctic Insect, *Belgica antarctica*. Arthropod Structure & Development 38 (2009) 377-389.
20. Taha N, Abdel–Meguid A, El–ebiarie A, Tohamy AA. Ultrastructure of the Midgut of the Early Third Larval Instar of *Chrysomya megacephala* (Diptera: Calliphoridae). Journal of American Science 6(10) (2010) 1–6.
21. Rost–Roszkowska MM, Chechelska A, Fradczak M, Salitra K. Ultrastructure of Two Types of Endocrine Cells in The Midgut Epithelim of *Spodoptera exiqua* Hûbner, 1808 (Insecta, Lepidoptera, Noctuidae). Zoologica Poloniae 53 (2008) 27–35.

Hittite Journal of Science and Engineering, 2014, 1 (1) , 13-20
ISSN NUMBER: 2149-2123
DOI: 10.17350/HJSE19030000003

Thermal Performance and Pressure Drop of Different Pin-Fin Geometries

Isak Kotcioglu[1], Gokhan Omeroglu[1] and Sinan Caliskan[2,*]
[1] Atatürk University, Department of Mechanical Engineering, Erzurum, TURKEY
[2] Hitit University, Department of Mechanical Engineering, Corum, TURKEY

ABSTRACT

The purpose of this study is to show the performance of hexagonal, square and cylindrical pin-fin arrays in improving heat transfer. In the present study, the thermal performance and pressure drop of the pin-fin heat exchanger are studied. The heat exchanger consists of cylindrical, hexagonal and square pin-fins. These types of pin-fins are capable of producing beneficial effects in transport enhancement and flow control. The pin-fins were arranged in an in-line manner. The relative longitudinal pitch ($S_L/D=2$), and the relative transverse pitch were kept constant ($S_T/D=2$). Air and water are used as working fluids in shell side and tube side, respectively. The inlet temperatures of air are between 50 and 90° C. The cold water entering the heat exchanger at the inner channel flows across the fin and flows out at the inner channel. Such pin-fins show potential for enhancing the heat transfer rate in pin-fin cross flow heat exchangers.

Article History:
Received: 2014/09/12
Accepted: 2014/12/22
Online: 2014/12/31

***Correspondence to**: Sinan Calıskan,*
Hitit University, Faculty of Engineering,
Department of Mechanical Engineering,
Corum, Turkey
Tel: +90 (364) 227-4533
Fax: +90 (364) 227-4535
E-Mail: sinancaliskan2000@yahoo.com

Key Words:
Thermal performance; Pressure drop; Cylindrical, Hexagonal and square fins

NOMENCLATURE

A	: Cross-sectional area of the test channel [m^2]
A_{total}	: Total heat dissipation area of pin-fins [m^2]
A_{base}	: Bottom area of the test channel [m^2]
A_f	: Fin surface area on one side of an exchanger [m^2]
A_o	: Minimum free-flow area [m^2]
D	: Pin-fins diameter [m]
D_{ch}	: Hydraulic diameter of the channel [m]
d_o	: Outer diameter of the tube [m]
d_i	: Internal diameter of the tube [m]
h	: Length of the hexagonal pin-fins [m]
k	: Conductivity [W/mK]
h_{av}	: Average convective heat transfer coefficient [W/m^{2}K]
L_1	: Height of the test section [m]
L_2	: Length of the test section [m]
L_3	: Width of the test section [m]
N_t	: Total number of pin-fins
N_f	: Number of pin-fins per unit length
Nu_D	: Pin-fin Nusselt number
Q	: Heat transfer rate [W]
s	: Length of the square pin-fins [m]
T	: Temperature [K]
t	: Distance between the pin-fins [m]
T_s	: Average surface temperature [K]
U	: Volumetric average fluid velocity [m/s]
S_L/D	: Relative longitudinal pitch
S_T/D	: Relative transverse pitch
ΔP	: Pressure drop [N/m^2]

Greek symbols

δ	: Plate thickness [m]
μ	: Fluid dynamic viscosity [kg /ms]
ρ	: Air density [kg/m^3]

Dimensionless numbers

f	: Friction factor
Re_D	: Pin-fin Reynolds number

Subscripts

c	: Circular
h	: Hexagonal
s	: Square
in	: Inlet
out	: Outlet
x, y	: Spanwise and streamwise direction, respectively

INTRODUCTION

Needs for small-size and light-weight heat exchanger devices in power, process, computer and aerospace industries have resulted heat transfer surfaces. In order to enhance heat transfer between the flowing fluid and closely-spaced pin fins, in the case of pin-fin heat exchangers, pin-fins can be mounted on the channel surfaces.

Jeng et al. [1] experimentally studied the pressure drop and heat transfer of a square pin-fin array in a rectangular channel by using the transient single-blow technique. The in-line square pin-fin array has smaller pressure drop than the in-line circular pin-fin array. The optimal inter-fin pitches of in-line square pin fin arrays are Xt = 2 and $X_L = 1.5$, its Nu_D^* is around 20% higher than that of the in-line circular pin-fin array. Vanfossen [2] studied heat transfer by short pin-fins in staggered arrangements. According to their results, longer pin-fins transfer more heat than shorter pin-fins and the array-averaged heat transfer with eight rows of pin-fins slightly exceeds that with only four rows. Their results also established that the average heat transfer coefficient on the pin surface is around 35% larger than that on the end walls.

Grannis and Sparrow [3] used the experiments to verify the accuracy of a numerical simulation of fluid flow through a diamond-shaped pin-fin array. They provided a correlation between the friction factor and the Reynolds number based on the results of numerical calculations.

Young et al. [4] experimentally examined the performs of pin-fin heat sinks having circular, elliptic, and square cross-section. The effect of pin-fin density on the heat transfer performance was examined. The elliptic pin-fin shows the lowest pressure drops. For the same surface area at a fixed pumping power, the elliptic pin-fin possesses the smallest thermal resistance for the staggered arrangement. Sparrow et al. [5] investigated pin-fin arrays both numerically and experimentally. The effects of length to diameter, array geometry, entrance length, and pin-fin shape have been reported.

Effects of height and width of hexagonal pin-fins, stream-wise and span-wise distances between pin-fins, and flow velocity on thermal resistance and pressure drop characteristics were investigated using Taguchi experimental design method by Yakut et al. [6]. They also determined the temperature distribution within the selected pin-fins. Chen et al. [7] carried out experiments regarding heat transfer and pressure drop coefficients in a rectangular duct with drop-shaped pin-fins. They reported the Nusselt number for a channel with drop-shaped pin-fins to be slightly higher than those of circular ones. Similarly, they also found out that the pressure drop of drop-shaped pin-fins is 42-51% less than that of circular ones.

Ricci and Montelpare [8] aimed to evaluate the convective heat transfer coefficient, i.e. the Nusselt number, of short pin-fins cooled by means of water in forced convection. In particular the work is focused on the geometry (circular, square, triangular, rhomboidal) shape effect for three pin-fins assembled in line and the thermal analysis is performed by using a quantitative infrared method developed in a previous work. The thermal analysis is related to ink flow visualizations in order to better understand the effects of the main flow field on the thermal exchange capacities of every pin-fin inside the line. Nusselt numbers and flow structural characteristics are presented by Won et al. [9] for a stationary channel with an aspect ratio of 8 and a staggered array of pin-fins between two of the surfaces. Local Nusselt numbers, measured on one end wall, are highest beneath primary and secondary horseshoe vortices located just upstream of individual pin-fins.

Hwang and Lu [10] made a study which is especially unique because three pin-fin configurations, each arranged in a staggered array, are considered in a trapezoidal duct, both with and without lateral flow ejection. Wang et al. [11]presented flow visualization and frictional results of enlarged pin-fin and tube heat exchangers with and without the presence of vortex generators. Two types of vortex generators and plain pin-fin geometry were examined in the study. Compared to the plain pin-fin geometry, the penalty of additional pressure drops of the proposed vortex generators is relatively insensitive to change of Reynolds number. As mentioned above, numerous works have been reported concerning the heat transfer and pressure drop for different pin-fin configurations.

Optimal spacing of a pin-fin in the span-wise and stream-wise directions has been determined by Kotcioglu et al. [12]. The experimental results showed that the use of hexagonal pin-fins, compared to square and cylindrical pin-fins, may lead to an advantage on the basis of heat transfer enhancement. The optimal inter-fin pitches are provided based on the largest Nusselt number under the same pumping power, while the optimal inter-fin pitches of hexagonal pin-fins were $S_T/D=2$ and $S_L/D= 2.8$.

The present study is an investigation of heat transfer characteristics and pressure drop in a channel with hexagonal, square and cylindrical pin-fins attached to upper and lower plates in an in-line arrangement. Effects of various relevant parameters on the heat transfer and pressure drop characteristics for different geometrical parameters are considered. According to the obtained results, heat transfer and differences among the channel f factor of the pin-fins are basically because of the geometrical shapes of the pin-fins, causing different flow patterns and vortices. Understanding these kinds of pin-fins, which are used widely in industry, is believed to give a rich contribution to elucidation of the phenomena in heat exchangers used in different applications.

EXPERIMENTAL

The channel flow experimental rig is shown in Figure 1. The rig consisted of a closed rectangular channel with a removable test section (16), blower (13), a data acquisition system (11), U-type manometer (8), heater (2), and thermocouples (17). The flow channel was constructed of wood of 20 mm thickness, had an internal cross section of 0.098 m width and 0.014 m height with a wall thickness of 0.01 m. Total length of the channel was 2 m. The system was operated in suction mode and positioned horizontally. A flow straightener (1) was fitted immediately after the inlet of the channel. In order to minimize the heat loss, the other surfaces of the heater were insulated by a combination of a 12 mm thick asbestos layer and a 20 mm thick glass. The thermostat (3), of which only the upper outside surface of the channel was heated, was located 0.25 m downstream of the flow straightener. Test section (16) was fitted 1.5 mm downstream of the inlet of the flow channel. The flow channel consisted of a wooden channel. The outlet of the flow channel length was at 0.90 m. The base plates of the test surface were made from two plates with aluminium alloy (ρ=2710 kg/m^3) as the rectangular channel of 5 mm thickness, 14 mm height, 98 mm width, and 130 mm length. Various type of pin-fins, which were made of the same aluminium material as the base plate, were attached between the bottom and upper surface of the base plates Figure 2 (a, b). Thermal glue was applied between the plate and the pin-fins for a better contact. The number of pin-fins can be adjusted to suit the required spacing between the pin-fins in the stream-wise direction. Twelve thermocouples were equally spaced along the base and top plate between the pin-fins for measurement of the bottom and top plate temperatures. They were equally spaced and in all cases positioned in the spaces between the pin-fins. Four thermocouples were used to measure the temperatures of the inlet and outlet of the air and water, respectively.

Analog signals from the experimental system were fed to the data acquisition card. All thermocouples were separately calibrated before being used in the experiments. While the air flow is passing from the horizontal direction of the channels, the water is passing from the vertical direction (see Figure 2a). The air transfers its heat to the water during this process. The pressure drop was determined using a glass tube U type manometer. The air flow temperature was controlled by a thermostat. Inlet temperature of the water

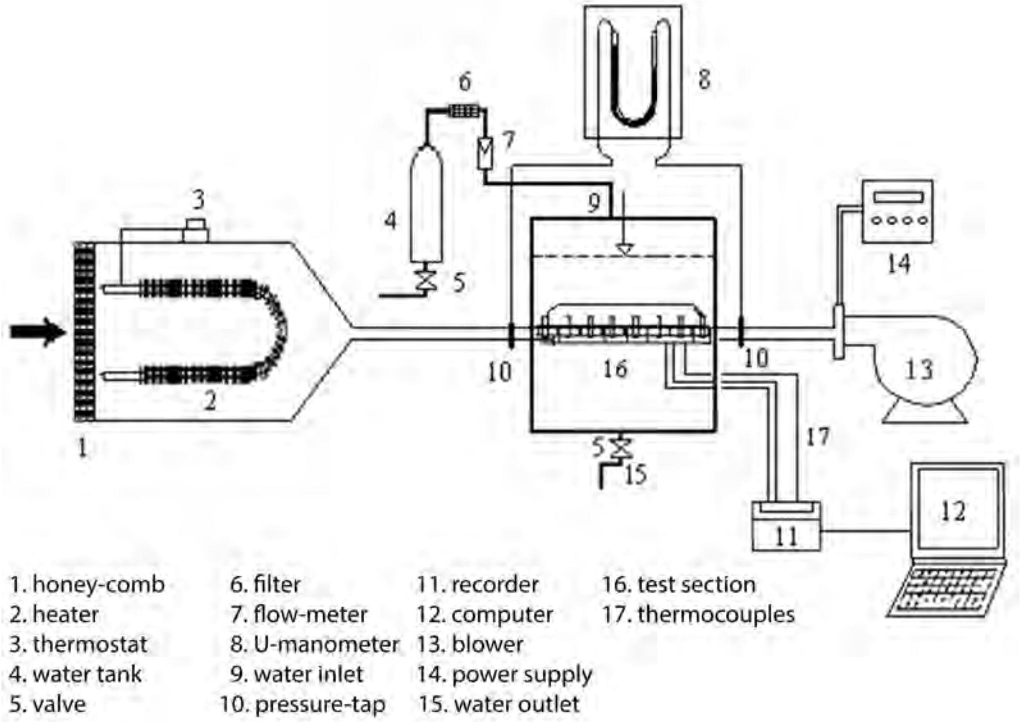

Figure 1. Schematic of experimental apparatus

was held between 17-20 °C. In the experiments, the duration to reach steady-state conditions was about 0.5-1 hour, depends on experimental conditions. The arrangement of the pin-fins on the test section is illustrated in Figure 2b.

Geometrical characteristics of the pin-fins are given Table 1.

Table 1. Geometrical characteristics of the pin-fins

	$A_o(m^2)$	$A_p(m^2)$	$A_f(m^2)$	$A\,(m^2)$
Hexagonal	0.000612	0.03175	0.0000880	0.03183
Square	0.000612	0.03175	0.0001436	0.03189
Circular	0.000612	0.03175	0.0001356	0.03188

Distance between pin-fins and number of pin-fins are given Table 2.

Table 2. Distance between pin-fins and number of pin- fins

Configuration	*Arrangement*	S_L/D =2 and S_T/D = 2		
		Nx	*Ny*	$N_{tot.}$
Hexagonal	*In- line*	6	8	48
Square	*In- line*	6	8	48
Circular	*In- line*	6	8	48

Geometrical properties of heat exchanger surface

The basic core geometry for an idealized single-pass cross-flow heat exchanger with an inline pin-fin arrangement is shown in Figure 2b. Total number of pin-fins, N_t is given as;

$$N_t = (L_2L_3)/S_TS_L \tag{1}$$

The total heat transfer area A consists of the area associated with the exposed pin-fins and header plates (primary surface area) A_p, and pin-fins (secondary surface area) A_f. For the circular, square and hexagonal fin, geometrical characteristics concerning the fin-tube outside surface are given as;

$$A_p=\pi d_o(L_1-\delta N_f L_1)N_t+1(L_2L_3-(\pi d_o^2/4)\ N_t) \tag{2}$$

Here ρ, is the plate thickness and N_f is the number of pin-fins per unit length. For the circular, square and hexagonal pin-fin, (secondary surface area) A_f is given respectively by;

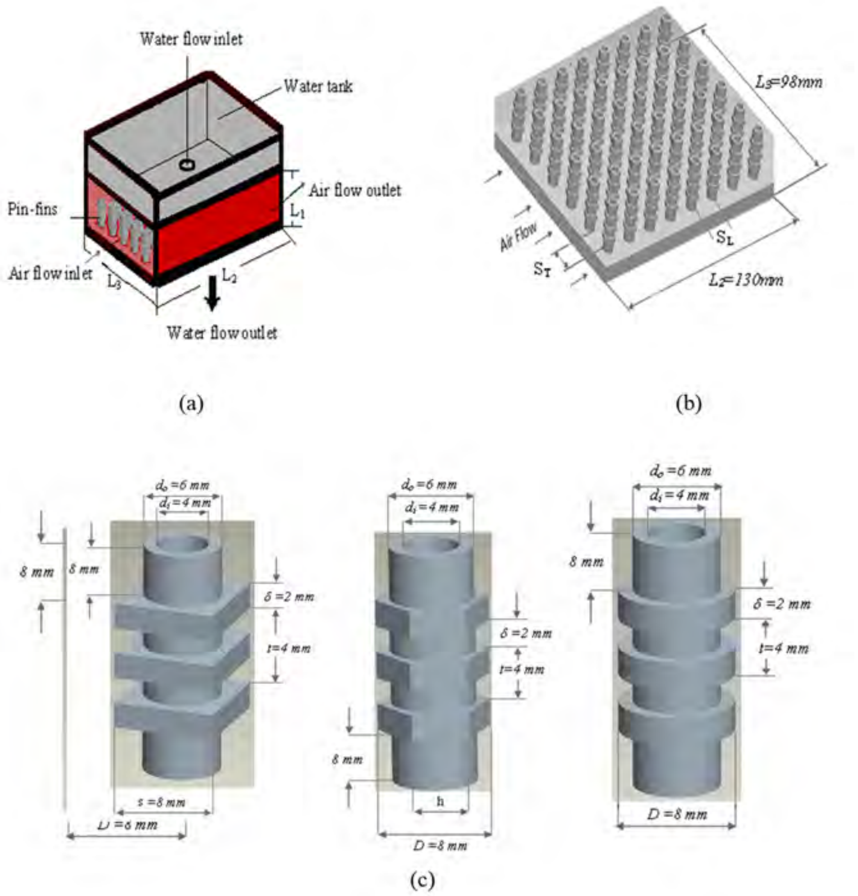

Figure 2. Shown are a) test section, b) upper view of the arrangement over the plate of hexagonal pin-fins, c) square, hexagonal, circular pin-fins, respectively.

$$A_{fc}=[2\pi(D^2-d_o{}^2)/4 + (\pi D\delta)]\ N_tN_fL_1 \quad (3)$$

$$A_{fs}=[s^2- (\pi d_o{}^2)/4 + (4s\delta)]\ N_tN_fL_1 \quad (4)$$

$$A_{fh}=[(2.59h^2- (\pi d_o{}^2/4) + (6h\delta)]\ N_tN_fL_1 \quad (5)$$

where D is the pin-fin diameter, d_0 is an outer diameter of the tube, δ is plate thickness, s is length of the square pin-fin and h is length of the hexagonal pin-fin. Total heat transfer area is then

$$A=A_p+A_f \quad (6)$$

Minimum free-flow area for inline arrangement is given by,

$$A_0=[(S_T - d_o)L_1 - (D-d_0)\ \delta N_fL_1](L_3/S_T) \quad (7)$$

Data reduction

The heat transfer modes of interest for the present system are conduction, convection and radiation through the air and water. The magnitude of each mode depends on the temperature of the pin-fin array's base, the assembly material and pin-fin geometry. Thus the heat balance equation for the whole system can be expressed as follows:

$$Q_{total}= Q_{conv.} + Q_{rad.} + Q_{loss} \quad (8)$$

In similar studies [13-16], it was reported that the total radiative heat-losses from a similar test surface would be about 0.5% of the total electrical heat-input. Therefore, the radiative heat loss could be neglected. Using these findings, together with the fact that the test section was well insulated and the readings of the thermo junction, placed at the outer surface of the heating section, was nearly equal to the ambient temperature. Then one could assume with some confidence that the last two terms of Eq. (8) may be ignored. Then, the Eq. (8) is reduced to

$$Q_{total} = Q_{conv.} \quad (9)$$

The steady-state convection heat transfer from the test section by convection can be expressed as,

$$Q_{conv.} = h_{av}A[\bar{T}_s - ((\bar{T}_{out}+\bar{T}_{in})/2)] \quad (10)$$

where $\bar{T}_s$ is average surface temperature of the base plate for the pin-fin assembly of the heat exchanger. $\bar{T}_{in}$ and $\bar{T}_{out}$ are the mean temperatures of the air flow at the inlet and the outlet, respectively. In all the calculations, the values of the thermo-physical properties of the air were obtained at the average bulk mean temperature from $\bar{T}_s = (\bar{T}_{out}+\bar{T}_{in})/2$. Either the projected or the total area of the test surface can be taken as the surface area in the calculations.

In the present experimental investigation, two types of Reynolds number were used to characterize the flow conditions. One is a Reynolds number based on the mean velocity (U) and the hydraulic diameter of the channel (D_{ch}) expressed as

$$Re=(\rho D_{ch}U)/\mu \quad (11)$$

Re is the channel Reynolds number. The other one is based on the maximum velocity through the pin-fins and the thickness of the pin-fins.

$$Re_D= (\rho DU_{max})/\mu \quad (12)$$

Re_D has been widely used as pin-fin Reynolds number in many pin-fin heat transfer studies. U_{max} is the maximum velocity through the fins and is given by

$$U_{max}=(A/(A-A_f)U) \quad (13)$$

where A is the cross-sectional area of the test channel and A_f is the frontal area of the pin-fins. In order to compare the results with those of other researches, this section applies the pin-fins Nusselt number Nu_D and $Re_D(U_{max}/U)$ to elucidate the relationship between the heat transfer and the maximum velocity of pin-fin array with various inter-fin pitches. For the present experimental setup, the values of $A/(A-A_f)$ are given in Table 3.

Table 3. Values of $A/(A-A_f)$ for $S_T/D=2$.

S_L/D	*Hexagonal*	*Square*	*Circular*
2	1.00277	1.00452	1.00427

The average Nusselt number is represented by pin-fin Nusselt number

$$Nu_D= (h_{av}D/k) \quad (14)$$

where is the average convective heat transfer coefficient and is the thermal conductivity of air. The friction factor (f) is defined as follows,

$$f=\Delta P/((L_2/D_{ch})\rho(U^2/2) \quad (15)$$

where is the density of air, the length of the test section, pressure drop, U average fluid velocity and D_{ch} channel hydraulic diameter.

Uncertainty analysis

By using the estimation method of Kline and McClintock [17] maximum uncertainty of mass flow rate was ±2.3%. The uncertainty in the pressure was 6.5%. The experimental results herein revealed that the uncertainties in the Reynolds number and Nusselt number were ±6.8% and ±7%, respectively. The individual contributions to the uncertainties for each of the measured physical properties are summarized in Table 4. A detailed error analysis is made to estimate the W_R uncertainty arising from different independent variables from the following equation

$$W_R=[(\partial RW_1/\partial x_1)^2+ (\partial RW_2/\partial x_2)^2+.....+(\partial RW_n/\partial x_n)^2]^{1/2} \quad (16)$$

Table 4. Uncertainties in the values of the relevant variables

Variable	Uncertainty (%)
Velocity of the air, U	0.5
Mean Temperature, T	0.25
Pressure, P	6.5
Hydraulic diameter of the channel,	0.1
Voltage, V	0.1
Current, I	0.72
Dynamic viscosity of the air,	0.045
Thermal conductivity of the air, k	0.33
Density of the air,	0.007
Re	0.068
Nu	0.070
f	0.065

RESULTS

Figures 3-6 shows the variation of the average bottom and top plate temperatures with air Reynolds number for two inlet air temperatures (50 and 90°C). As expected, the heat transfer rate depends on the cooling capacity rate of inlet air temperatures. Therefore, the average bottom plate temperature decreases with increasing of Reynolds number. However, this effect tends to diminish as Reynolds number increases. As shown in Figure 3, the average bottom plate temperature depends on the supplied heat to the cylindrical, hexagonal and square pin-fins. In addition, average bottom plate temperatures at higher hexagonal are lower than those from lower ones. Due to higher surface area, heat transfer from the surface to the air increases. Therefore, cylindrical pin-fins give lower bottom plate temperatures. The average top plate temperatures are higher than bottom plates. As shown in Figures 3-6, hexagonal pin-fin arrays increase heat transfer more by increasing the flow turbulence than circular and square pin-fin arrays. The growth of recirculation zones promote the mixing of fluid in the boundary layer, thereby enhancing the convective heat transfer.

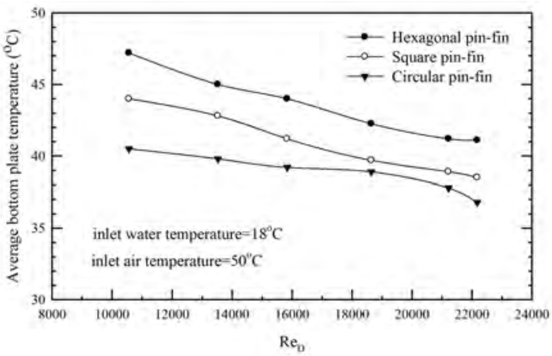

Figure 3. Variation of average bottom plate temperature with Reynolds number.

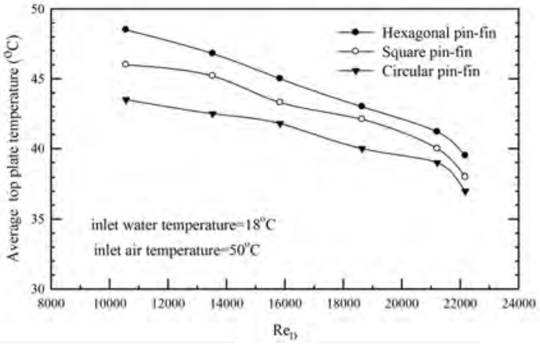

Figure 4. Variation of average top plate temperature with Reynolds number.

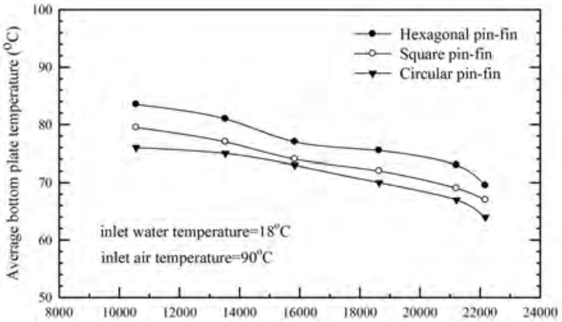

Figure 5. Variation of average bottom plate temperature with Reynolds number.

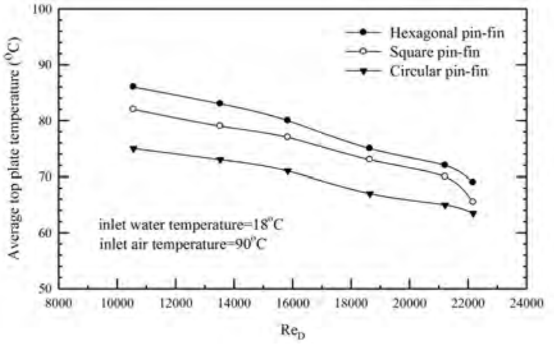

Figure 6. Variation of average top plate temperature with Reynolds number.

Figure 7 shows the variation of Nusselt number with air Reynolds number for square pin-fins for different inlet air temperatures. It can be seen that the Nusselt number tends to increases as air Reynolds number and inlet air temperatures are increased. For a given air Reynolds number, inlet air temperature has a significant effect on the Nusselt number.

Figure 8 shows the variation of the outlet air temperature with air Reynolds number for different pin-fins. Outlet air temperature tends to decrease as Reynolds number increases. As expected, when the Reynolds numbers are kept constant, pin-fins geometry has significant effect on the outlet air temperatures. Higher of fluid re-circulation or/and higher swirl flows change in the geometrical shapes, therefore the Nusselt number increases as shown in Figure 8.

Figure 9 depicts the friction factor (f) for the pin-fins as a function of the Reynolds number (Re_D). The circular pin–fins have smaller pressure drops than the hexagonal and square pin-fins. The results show that the pressure drop falls as Re number increases. These differences among the channel friction factor of the pin-fins are basically because of the geometrical shapes of the pin-fins causing different flow patterns and vortices.

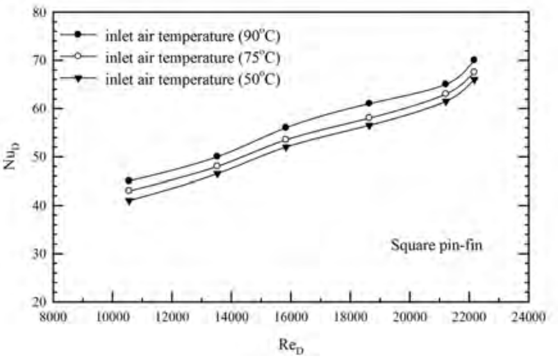

Figure 7. Variation of Nusselt number with Reynolds number for different inlet air temperatures.

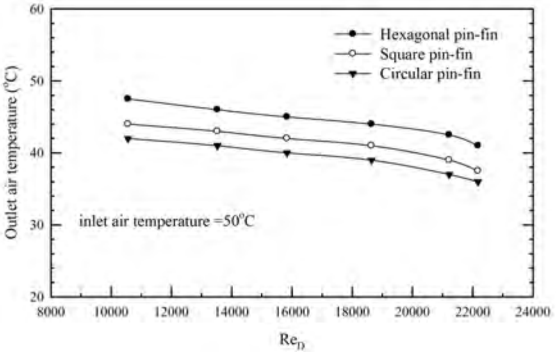

Figure 8. Variation of outlet air temperature with Reynolds number.

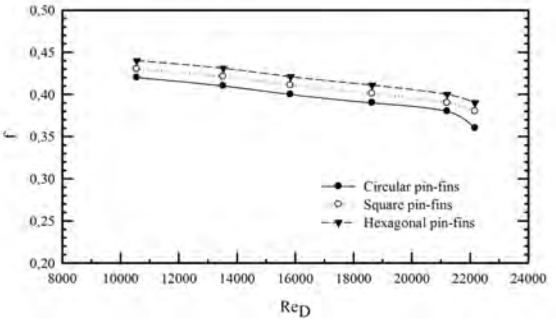

Figure 9. Duct friction factor as a function of Reynolds number.

CONCLUSIONS

Forced convection in a rectangular channel with various pin-fins geometries has been experimentally investigated. The pin-fins were inserted periodically into the rectangular channel. The effects of the geometrical parameters on the heat transfer and friction characteristics were determined. The following conclusions were drawn from the results of the present work:

- The average bottom and top plate temperatures decrease as air Reynolds number increases. The highest values of the bottom and top plate temperatures were obtained for the hexagonal geometry and 90°C inlet air temperature.
- The circular pin-fins array has a smaller pressure drop compared to the square and hexagonal pin-fins arrays.
- The Nusselt number increased with increasing inlet air temperature.

REFERENCES

1. Jeng TM, Tzeng SC. Pressure drop and heat transfer of square pin-fin arrays in in–line and staggered arrangements. International Journal of Heat and Mass Transfer 50 (2007) 2364–2375.

2. Vanfossen GJ. Heat transfer coefficients for staggered arrays of short pin-fins. Transactions of ASME, Journal of Heat Transfer 104 (1982) 268-274.
3. Grannis VB, Sparrow EM. Numerical simulation of fluid flow through an array of diamond–shaped pin fins. Numerical Heat Transfer Applications (Part A). 19 (1991) 381-403.
4. Yang KS, Chu WH, Chen IY, Wang CC. A comparative study of the airside performance of heat sinks having pin fin configurations. International Journal of Heat and Mass Transfer 50 (2007) 661-4667.
5. Sparrow EM, Larson ED. Heat transfer from pin–fins situated in an oncoming longitudinal flow which turns to cross–flow. International Journal of Heat and Mass Transfer 25 (1982) 603–614.
6. Yakut K, Alemdaroglu N, Kotcioglu I, Celik C. Experimental investigation of thermal resistance of a heat sink with hexagonal fins. Applied Thermal Engineering 26 (2006) 2262–2271.
7. Chen Z, Li Q, Meier D, Warnecke HJ. Convective heat transfer and pressure loss in rectangular ducts with drop–shaped pin fins. Heat and Mass Transfer 33 (1997) 219–224.
8. Ricci R, Montelpare S. An experimental IR thermographic method for the evaluation of the heat transfer coefficient of liquid–cooled short pin fins arranged in line. Experimental Thermal and Fluid Science 30 (2006) 381-391.
9. Won SY, Mahmood GI, Ligrani PM., Spatially–resolved heat transfer and flow structure in a rectangular channel with pin fins. International Journal of Heat and Mass Transfer 47 (2004) 1731–1743.
10. Hwang JJ, Lu CC. Lateral–flow effect on end wall heat transfer and pressure drop in a pin–fin trapezoidal duct of various pin shapes. ASME Paper No. 2000–GT–232, 2000.
11. Wang CC, Lo J, Lin YT, Wie CS. Flow visualization of annular and delta winglet vortex generators in fin–and–tube heat exchanger application. International Journal of Heat and Mass Transfer 45 (2002) 3803–3815.
12. Kotcioglu I, Caliskan S, Baskaya S. Experimental study on the heat transfer and pressure drop of a cross–flow heat exchanger with different pin-fin arrays. Heat and Mass Transfer 47 (2011) 1133-1142.
13. Tahat MA, Babus'Haq RF, Probert SD. Forced steady–state convections from pin-fin arrays. Applied Energy 48 (1994) 335–351.
14. El–Sayed SA, Mohamed MS, Abdel–latif AM, Abouda AE. Investigation of turbulent heat transfer and fluid flow in longitudinal rectangular–fin arrays of different geometries and shrouded fin array. Experimental Thermal and Fluid Science 26 (2002) 879–900.
15. Chen TY, Shu TH. Flow structures and heat–transfer characteristics in fan flows with and without delta–wing vortex generators. Experimental Thermal and Fluid Science 28 (2003) 273–282.
16. Jubran BA, Al–Salaymeh AS. Heat–transfer enhancement in electronic modules using ribs and ''film cooling–like'' techniques. International Journal of Heat and Fluid Flow 17 (1996) 148-154.
17. Kline SJ, McClinctock FA. Describing uncertainties in single–sample experiments. Mechanical Engineering 75 (1953) 3-8

Hittite Journal of Science and Engineering, 2014, 1 (1) 21-26
ISSN NUMBER: 2149-2123
DOI: 10.17350/HJSE19030000004

Metal Ion Coordination Interactions for Biomolecule Recognition: a Review

Emel Tamahkar[1,2] and Adil Denizli[3]
[1] Hitit University, Department of Chemical Engineering, Corum, TURKEY
[2] Hacettepe University, Bioengineering Division, Beytepe, Ankara, TURKEY
[3] Hacettepe University, Department of Chemistry, Beytepe, Ankara, TURKEY

ABSTRACT

Molecular imprinting is an effective method to create selective binding sites in polymeric matrices for biomolecule recognition. This review gives recent improvements of the design and preparation of selective binding sites via metal coordination interactions in molecularly imprinted polymers (MIPs) and focuses on particularly metal coordination bonds between biomolecules such as amino acids, peptides, proteins and templated polymers. The discussion will evaluate key parameters for molecular imprinting in the perspective of metal coordination.

Article History:
Received: 2014/10/04
Accepted: 2014/12/29
Online: 2014/12/31

Correspondence to: *Adil Denizli,*
Hacettepe University, Faculty of Science,
Department of Chemistry, Ankara, Turkey
Tel: +90 (312) 297 79 83
Fax: +90 (312) 297 6084
E-Mail: denizli@hacettepe.edu.tr

Key Words:
Metal ion coordination; Molecular imprinting; Metal chelation; Biomolecule recognition

INTRODUCTION

Molecular imprinting is an effective method to introduce highly selective binding sites into polymeric materials to specifically rebind template molecule in preference to analog molecules. The functional groups complementary to template molecule are led to form an assembly around template. Highly specific polymeric materials are obtained polymerising functional monomers and cross linking agents around this complex. Template molecule is then extracted and thus binding sites complementary to template are established (Figure 1) [1]. The molecular imprinted polymers (MIP)s are resistant to elevated temperature and pressure, inert to chemicals, stable and cheap [2].

The driving forces required for the binding between template and functional monomer are covalent bonds, non covalent bonds and metal coordination. The strength of the interactions between template and monomer is significant for the efficiency of the imprinting process [3, 4]. In covalent imprinting, the template molecule is bound to monomer with functional groups covalently. However, covalent bonding gives strong interactions between template and monomer, it has slow rebinding kinetics and harsh conditions are required for template removal after polymerization step [5].

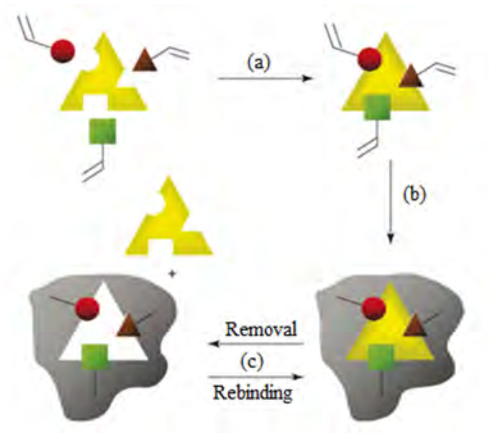

Figure 1. Representation of molecular imprinting process. Reprinted from ref. [1].

Non covalent imprinting relies on secondary interactions between template and monomer such as hydrogen bonding, van der Waals interactions and Coulomb forces. Despite water is common solvent for molecular imprinting since many biomolecules have limited solubility in organic media, the recognition capability is reduced due to weakness of hydrogen bonds. Also imprinting effect may be weakened in aqueous environment since polar solvents compete with hydrogen bonding interactions [6].

The principles of metal ion coordination in molecular imprinting process

Metal ion coordination with biological molecules is well suited to molecular recognition due to its specificity and stability. In metal coordination during imprinting process, metal chelating monomers are pre-complexed to metal ion, generally a transition metal ion, which, in turn, coordinates the template molecule. Metal ions are employed as mediator that directs functional monomer and template molecule to establish a high fidelity of imprint with high specificity [7-9]. Metal coordination has higher strength with respect to hydrogen bonding which makes it more stable in water for example, binding energy of the Cu^{2+} complex and imidazole residue of histidine is 4.8 kcal/mol and it is less than 1 kcal/mol for typical hydrogen bonding interaction [10]. Additionally metal coordination is a fast binding process and binding strength can be adjusted by choosing appropriate metal ion for a defined template molecule. Furthermore it is possible to replace the metal ion with another one to enhance the selectivity or use the MIP for different aim [11-13]. Therefore within this context metal coordination approach has an important potential for preparation of highly specific MIPs in aqueous medium.

The most important step of the preparation of the MIP is the prearrangement of the functional monomer, the metal ion and the template molecule. This ternary complex is then polymerized with cross linking agents initiated thermally or by UV light. After polymerization the template molecule is removed with appropriate agents. In order to use the material with other metal ions, it can be washed with complexing agents such as ethylenediaminetetraacetic acid (EDTA) to remove all the metal content then the other metal ion can be reloaded [14].

Key parameters for metal coordination

The selection of metal ion is one of the most important parameter to obtain specific recognition. Template molecule dominates the type of the metal ion used for imprinting process. The type of the metal ion defines binding strength of the template, metal ion and monomer complex and the spatial arrangement of this complexation [15]. In order to obtain high specificity, coordination mode of the metal ion and monomer complex should be determined. The molecularly imprinted polymers for the application of analyte extraction from biological fluids was prepared in aqueous medium with tetracyclines-a large family of common antibiotics–as template molecule, Fe^{2+} as mediator and methacrylic acid (MAA) as functional monomer (Figure 2) [12]. Different metal ions such as Mg^{2+}, Fe^{2+} and Cu^{2+} were complexed with tetracycline (TC) in the preparation of MIPs. It is found that Fe^{2+} could obtain high recognition capability due to specific coordination interactions between TC and MAA.

As mentioned the self assembly of template-monomer is the pre-organization and first step for the fabrication of MIPs. Utilizing metal ion as mediator assembles a bridge between template and monomer through coordination bond. (S)-Naproxen was complexed with 4-vinylpyridine through coordination with Co^{2+} and thus MIP with high selectivity was prepared [16]. Figure 3 shows the schematic presentation of this complex and also the binding of template and monomer via hydrogen bonding. It was shown that without metal ion which means by using only hydrogen bonding interactions, selectivity for template was reduced significantly. The stoichiometry of the complex used was determined with UV spectrum by titrating monomer and template. The optimization of monomer amount is required for the design of MIP since high amount of monomer results low adsorption capacity due to inefficient template removal and low amount of monomer causes incomplete organization of template in templated polymer matrix. In the same manner, the amount of metal ion plays important role to enhance selectivity. In order to form highly specific recognition sites complementary to template, the stoichiometric amount of metal ion to bridge the specific interaction between template and monomer with high stability is necessary due to structural and spatial complementary to template [17].

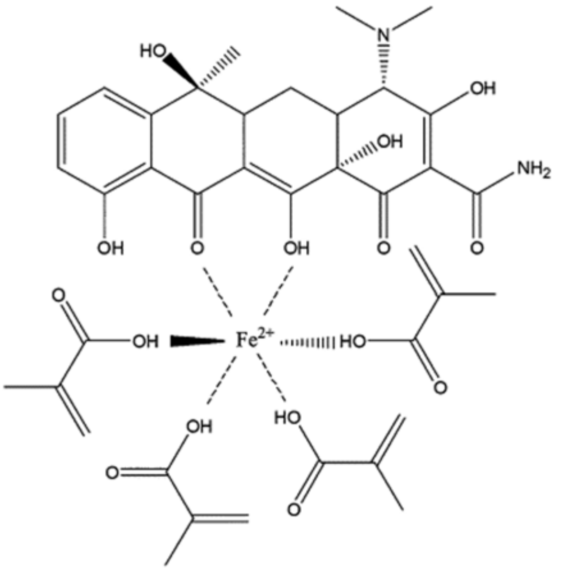

Figure 2. The schematic representation of complexation of TC/Fe^{2+}/MAA. Reproduced from ref. [12].

The other parameter is the influence of the anion used since it may participate in the recognition process.

Molecularly imprinted solid phase microextraction fiber was developed to recognize thiabendazole (TBZ) -a kind of fungicide- via the metal coordination interaction and it was found that enrichment properties in aqueous solutions were improved with respect to hydrogen bonding interactions. Four different copper salts as acetate, sulfate, nitrate and chloride were studied with respect to adsorption capacity and copper(II) acetate was found to show the highest adsorption capacity. This demonstrates that anion has an effect on the recognition process since it changes the size and shape of the metal-template-monomer complex [18].

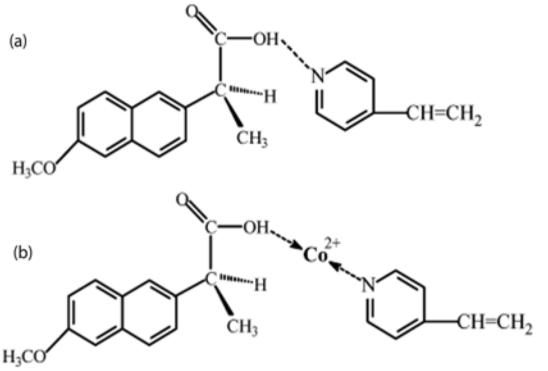

Figure 3. The binding interactions of MIP via a) H-bonding and b) metal coordination. Reprinted from ref. [16].

Metal coordination for bis(imidazole) recognition

Metal ion coordination with its specificity and stability is well suited procedure for molecular recognition of biological molecules which is exemplified by the chromatographic method namely IMAC (Immobilized Metal Affinity Chromatography) [19-21]. It has been developed by Porath and protein purification was achieved via binding of electron donor groups on protein surface and metal ion immobilized on the support surface [22]. The amino and carboxyl groups of amino acid participate in the fabrication of metal-amino acid complex. Especially, histidine containing peptides form more stable complex with metal ions due to metal coordination between metal ion and imidazole side chain of amino acid. The common chelating ligands are iminodiacetic acid (IDA), nitrilotriacetic acid (NTA) and tris carboxymethyl ethylene diamine (TED) are shown below (Figure 4).

The complementarity between metal ion and template molecule forms specific assembly prior to polymerization. After polymerization when template is removed from polymer matrix, a very specific binding cavity is formed as complementary to template due to this specific arrangement of functional groups around template molecule. In order to prepare selective abiotic receptors for 1,4-Bis(imidazol-1-ylmethyl)benzene (2 in Figure 5) which is analog of surface histidine bearing proteins, metal chelating monomer copper(II) (N-(4-vinylbenzyl)-imino) diacetic acid was pre-organized with template molecule and then polymerized in the presence of cross linking agent [5]. The affinity for molecule 2 was determined higher than the analog molecules 4,4'-Bis(imidazol-l-ylmethyl)biphenyl (4) and 1-Imidazol-l-ylmethyl)-4-(pyrrol-l-ylmethyl)benzene (6) which contain single imidazole. This bigger affinity may explain two point binding mechanism of the template to MIP and it shows that the templating is very critical for distribution of metal ions through the polymer matrix.

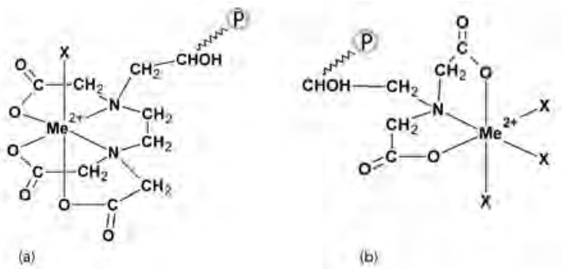

Figure 4. Metal coordination between metal ion (Me) and a) TED and b) IDA. Reproduced from ref. [22].

Metal coordination for amino acid, peptide and protein recognition

Amino acid imprinted polymers were developed via metal coordination for chiral separation of various amino acids from aqueous solutions [23]. MIPs were prepared with the complex of Cu^{2+}-N-(4-vinyl benzyl) iminodiacetic acid as functional monomer and template amino acid in

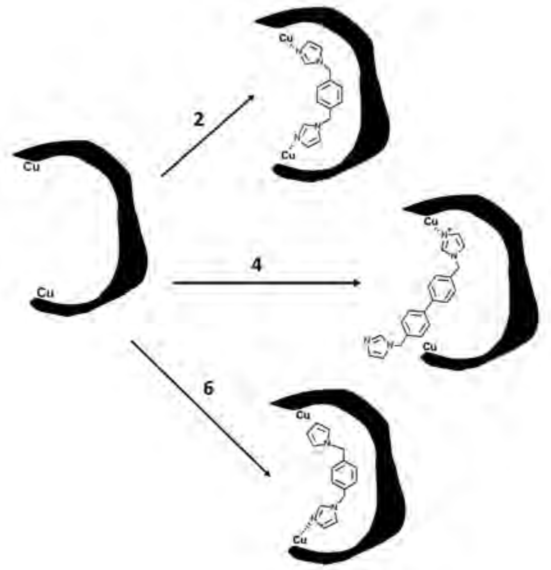

Figure 5. Schematic representation of binding of various bis(imidazole) molecules. Reproduced from ref. [5].

the presence of cross linkers. All the MIPs showed high enantioselectivity for the template amino acid and also it was reported that enantioselectivity depends on both size and shape of the side chain of the amino acid.

Hochuli et al. has been firstly developed a new quadridentate chelating ligand nitrilotriacetic acid (NTA) for protein purification via metal chelate chromatography [24]. It was reported that NTA forms more stable coordination interaction with both Cu^{2+} and Ni^{2+} than the interaction with IDA and each of these metals. NTA when complexed with Ni^{2+} occupies four positions in metal octahedral coordination sphere and leaving two for dipeptide His-Ala interaction [25]. It was achieved by selective polymeric receptors to separate between peptide sequence via strong coordination NTA, Ni and His-Ala.

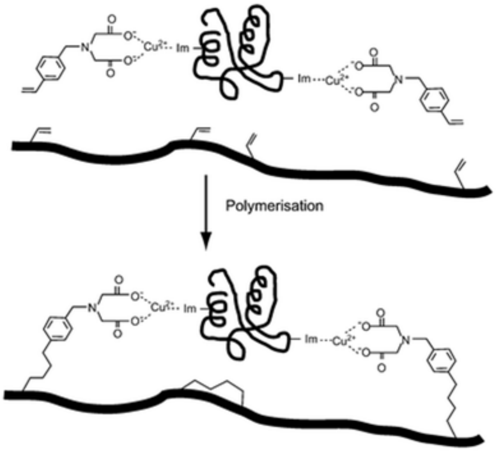

Figure 6. The schematic presentation of protein imprinting process with metal coordination. Reproduced from ref. [32].

Due to the complex and flexible structure of proteins, molecular imprinting process of these large molecules is still challenging task and reviewed by many scientists [26-29]. Proteins are not compatible with MIP process since MIP is synthesized in organic media and proteins are generally soluble in aqueous solutions [30]. Proteins are not resistant to environmental changes such as pH, temperature etc. [31]. Kempe et al. was first developed molecularly imprinting procedure for protein imprinting using the advantages of metal ion coordination interactions [32]. MIPs were prepared to recognize ribonuclease A (RNase A) through metal coordination utilizing N-(4-vinyl)-benzyl iminodiacetic acid (VBIDA) as metal chelating monomer and copper ion as mediator in the presence of the protein onto methacrylate-derivatized silica particles (Figure 6). There has been growing attention in metal mediated protein imprinted polymers [33-36]. All these studies show promising properties of metal coordination for the preparation of highly selective MIPs via stable and specific arrangement of metal ions with protein surface for protein separation and recognition.

A thermoresponsive macroporous hydrogel for lysozyme recognition was developed via molecular imprinting method based on metal coordination interaction between protein and metal ion [37]. (N-(4-vinyl)-benzyl iminodiacetic acid) (VBIDA) as metal chelate monomer was pre-organized with Cu^{2+} as mediator and lysozyme as template and then polymerized with NIPAAm (N-isopropylacrylamide) for thermoresponsiveness, AAm (acrylamide) for mechanical strenght and N,N-methylenebisacrylamide for cross linking. The Lysozyme-MIP prepared via metal coordination between VBIDA, Cu^{2+} and lysozyme demonstrated higher protein recognition than Lysozyme-MIP prepared via electrostatic interactions obtained with VBIDA and protein. Also it was confirmed with selectivity tests that metal coordination was important to positioning the binding groups around the template molecule. Porcine serum albumin (PSA) imprinted silica particles were prepared using IDA as metal chelating agent and copper as metal ion in the presence of (3-Aminopropyl)triethoxysilane (APTES) [38]. It was shown that PSA-MIP demonstrates highly specific recognition for template molecule in comparison with NIP and MIP-no metal ion coordination.

Proteins may undergo conformational changes in the presence of monomers and crosslinkers due to its vulnerable nature. It was reported that for lysozyme and bovine hemoglobin there was a significant change on conformational states of both proteins when in solution with various common monomers and crosslinkers [39]. This conformational change would impair the recognition sites targeting a certain protein molecule. In that study, epitope approach was offered to achieve efficient protein imprinting process. L-histidine imprinted polymers were developed via metal coordination between Cu^{2+} as mediator, L-histidine as template and N-methacryoyl-(L)-histidine (MAH) as metal-chelating monomer for selective separation of cytochrome c [40]. The chromatographic separation of L- histidine, cytochrome c and ribonuclease A was achieved.

Surface imprinted silica particles were prepared for hemoglobin recognition using a novel approach [41]. The template protein was immobilized onto surface via metal coordination prior to silanes polymerization. Hemoglobin was removed using different strategies and it was determined that the highest recognition capacity was obtained when 22% of hemoglobin was removed. These experimental results show that soft imprinted cavities were achieved to create which induce recognition of protein molecules by sub-stoichiometrically removal of template protein.

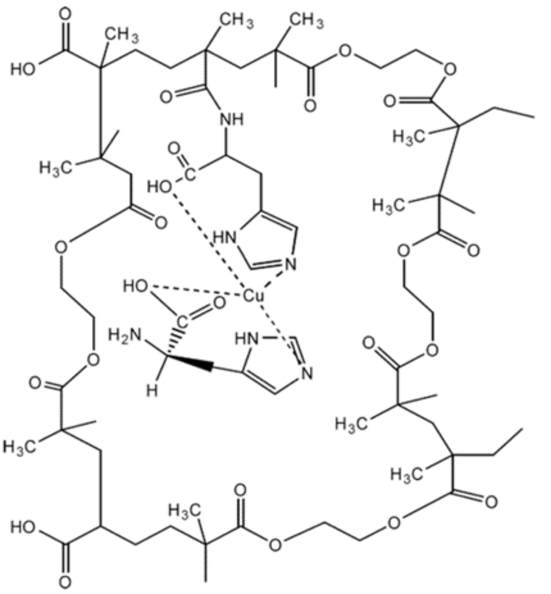

Figure 7. The representation of MAH-Cu^{2+}-L-histidine formation. Reprinted from ref. [40].

CONCLUSIONS

Molecular imprinting is considered as an important method to obtain highly specific recognitive polymeric matrices for protein recognition [42-47]. Within this review article many MIPs showing high selectivity prepared utilizing metal coordination interactions templating various molecules such as bis(imidazoles), amino acids, peptides and proteins have been mentioned. Molecular imprinting method utilizing metal coordination interactions is attractive to obtain highly specific and stable recognition sites for separation of biomolecules even like proteins.

REFERENCES

1. Ge Y, Turner APF. Too large to fit? Recent developments in macromolecular imprinting. Trends in Biotechnology 26 (2008) 218–224.
2. Vasapollo G, Sole RD, Mergola L, Lazzoi MR, Scardino A, Scorrano S, Mele G. Molecularly Imprinted Polymers: Present and Future Prospective. International Journal of Molecular Sciences 12 (2011) 5908–5945.
3. Bereli N, Saylan Y, Uzun L, Say R, Denizli A. l–Histidine imprinted supermacroporous cryogels for protein recognition. Separation and Purification Technology 82 (2011) 28–35.
4. Tatemichi M, Sakamoto M–a, Mizuhata M, Deki S, Takeuchi T. Protein–Templated Organic/Inorganic Hybrid Materials Prepared by Liquid–Phase Deposition. Journal of the American Chemical Society 129 (2007) 10906–10910.
5. Dhal PK, Arnold FH. Metal–coordination interactions in the template–mediated synthesis of substrate–selective polymers: recognition of bis(imidazole) substrates by copper(II) iminodiacetate containing polymers. Macromolecules 25 (1992) 7051–7059.
6. Hart BR, Shea KJ. Synthetic Peptide Receptors: Molecularly Imprinted Polymers for the Recognition of Peptides Using Peptide–Metal Interactions. Journal of the American Chemical Society 123 (2001) 2072–2073.
7. Huang J, Hu Y, Hu Y, Li G. Development of metal complex imprinted solid–phase microextraction fiber for 2,2′–dipyridine recognition in aqueous medium. Talanta 83 (2011) 1721–1729.
8. Huang J, Hu Y, Hu Y, Li, G. Disposable terbium (III) salicylate complex imprinted membrane using solid phase surface fluorescence method for fast separation and detection of salicylic acid in pharmaceuticals and human urine. Talanta 107 (2013) 49–54.
9. Lian H, Hu Y, Li G. Novel metal ion–mediated complex imprinted membrane for selective recognition and direct determination of naproxen in pharmaceuticals by solid surface fluorescence. Talanta 116 (2013) 460–467.
10. Mallik S, Johnson RD, Arnold FH. Synthetic Bis–Metal Ion Receptors for Bis–Imidazole "Protein Analogs". Journal of the American Chemical Society 116 (1994) 8902–8911.
11. Wang X, Xu Z, Bing N, Yang Z. Preparation and Aqueous Recognition of Metal Complex Imprinted Polymer Using N–vinyl–2–pyrrolidone as Functional Monomer. Chinese Journal of Chemical Engineering 15 (2007) 595–599.
12. Qu G, Zheng S, Liu Y, Xie W, Wu A, Zhang D. Metal ion mediated synthesis of molecularly imprinted polymers targeting tetracyclines in aqueous samples. Journal of Chromatography B 877 (2009) 3187–3193.
13. Lian H, Hu Y, Li G. Novel metal–ion–mediated, complex–imprinted solid–phase microextraction fiber for the selective recognition of thiabendazole in citrus and soil samples. Journal of Separation Science 37 (2014) 106–113.
14. Krebs JF, Borovik AS. Metallo–Network Polymers: Reversible CO Binding to an Immobilized Copper(I) Complex. Journal of the American Chemical Society 117 (1995) 10593–10594.
15. Striegler S. Designing selective sites in templated polymers utilizing coordinative bonds. Journal of Chromatography B 804 (2004) 183–195.
16. Li S, Liao C, Li W, Chen Y, Hao, X. Rationally Designing Molecularly Imprinted Polymer towards Predetermined High Selectivity by Using Metal as Assembled Pivot. Macromolecular Bioscience 7 (2007) 1112–1120.
17. Chaitidou S, Kotrotsiou O, Kiparissides, C. On the synthesis and rebinding properties of $[Co(C_2H_3O_2)2(z\text{–}Histidine)]$ imprinted polymers prepared by precipitation polymerization. Materials Science and Engineering: C 29 (2009) 1415–1421.
18. Wu L, Li Y. Metal ion–mediated molecular–imprinting polymer for indirect recognition of formate, acetate and propionate. Analytica Chimica Acta 517 (2004) 145–151.
19. Dhal PK, Arnold FH. Template–mediated synthesis of metal–complexing polymers for molecular recognition. Journal of the American Chemical Society 113 (1991) 7417–7418.
20. Mallik S, Johnson RD, Arnold FH. Selective recognition of bis–imidazoles by complementary bis–metal ion complexes. Journal of the American Chemical Society 115 (1993) 2518–2520
21. Türkmen D, Yavuz H, Denizli, A. Synthesis of tentacle type magnetic beads as immobilized metal chelate affinity support for cytochrome c adsorption. International Journal of Biological Macromolecules 38 (2006) 126–133

22. Sulkowski E. Purification of proteins by IMAC. Trends in Biotechnology 3 (1985) 1–7.
23. Vidyasankar S, Ru M, Arnold FH. Molecularly imprinted ligand–exchange adsorbents for the chiral separation of underivatized amino acids. Journal of Chromatography A 775 (1997) 51–63.
24. Hochuli E, Döbeli H, Schacher A. New metal chelate adsorbent selective for proteins and peptides containing neighbouring histidine residues. Journal of Chromatography A 411 (1987) 177–184.
25. Hart BR, Shea KJ. Molecular Imprinting for the Recognition of N–Terminal Histidine Peptides in Aqueous Solution. Macromolecules 35 (2002) 6192–6201.
26. Verheyen E, Schillemans JP, van Wijk M, Demeniex M–A, Hennink WE, van Nostrum CF. Challenges for the effective molecular imprinting of proteins. Biomaterials 32 (2011) 3008–3020.
27. Bossi A, Bonini F, Turner APF, Piletsky SA. Molecularly imprinted polymers for the recognition of proteins: The state of the art. Biosensors and Bioelectronics 22 (2007) 1131–1137.
28. Hillberg AL, Tabrizian M. Biomolecule imprinting: Developments in mimicking dynamic natural recognition systems. IRBM 29 (2008) 89–104.
29. Takeuchi T, Hishiya T. Molecular imprinting of proteins emerging as a tool for protein recognition. Organic & Biomolecular Chemistry 6 (2008) 2459–2467.
30. Levi L, Srebnik S. Simulation of Protein–Imprinted Polymers. 1. Imprinted Pore Properties. The Journal of Physical Chemistry B 114 (2009) 107–114.
31. Kryscio DR, Peppas NA. Critical review and perspective of macromolecularly imprinted polymers. Acta Biomaterialia 8 (2012) 461–473.
32. Kempe M, Glad M, Mosbach K. An approach towards surface imprinting using the enzyme ribonuclease A. Journal of Molecular Recognition 8 (1995) 35–39.
33. Bereli N, Andaç M, Baydemir G, Say R, Galaev IY, Denizli A. Protein recognition via ion–coordinated molecularly imprinted supermacroporous cryogels. Journal of Chromatography A 1190 (2008) 18–26.
34. Odabaşi M, Say R, Denizli A. Molecular imprinted particles for lysozyme purification. Materials Science and Engineering: C 27 (2007) 90–99.
35. Tamahkar E, Bereli N, Say R, Denizli A. Molecularly imprinted supermacroporous cryogels for cytochrome c recognition. Journal of Separation Science 34 (2011) 3433–3440.
36. Asliyuce S, Uzun L, Say R, Denizli A. Immunoglobulin G recognition with Fab fragments imprinted monolithic cryogels: Evaluation of the effects of metal–ion assisted–coordination of template molecule. Reactive and Functional Polymers 73 (2013) 813–820.
37. Qin L, He X–W, Zhang W, Li W–Y, Zhang Y–K. Macroporous Thermosensitive Imprinted Hydrogel for Recognition of Protein by Metal Coordinate Interaction. Analytical Chemistry 81 (2009) 7206–7216.
38. Liu J, Yang K, Deng Q, Li Q, Zhang L, Liang Z and Zhang Y. Preparation of a new type of affinity materials combining metal coordination with molecular imprinting. Chemical Communications 47 (2011) 3969–3971.
39. Kryscio D, Fleming M, Peppas N. Conformational studies of common protein templates in macromolecularly imprinted polymers. Biomedical Microdevices 14 (2012) 679–687.
40. Özcan AA, Say R, Denizli A, Ersöz A. l–Histidine Imprinted Synthetic Receptor for Biochromatography Applications. Analytical Chemistry 78 (2006) 7253–7258.
41. Lei W, Meng Z, Zhang W, Zhang L, Xue M, Wang W. “Induced fit” recognition of proteins by surface imprinted silica with “soft” recognition sites. Talanta 99 (2012) 966–971.
42. Ertürk G, Bereli N, Ramteke P, Denizli, A. Molecularly Imprinted Supermacroporous Cryogels for Myoglobin Recognition. Applied Biochemical Biotechnology 173 (2014) 1250–1262.
43. Ertürk G, Bereli N, Tümer MA, Say R, Denizli A. Molecularly imprinted cryogels for human interferon–alpha purification from human gingival fibroblast culture. Journal of Molecular Recognition 26 (2013) 633–642.
44. Baydemir G, Andaç M, Perçin I, Derazshamshir A, Denizli A. Molecularly imprinted composite cryogels for hemoglobin depletion from human blood. Journal of Molecular Recognition 27 (2014) 528–536.
45. Saylan Y, Üzek R, Uzun L, Denizli A. Surface imprinting approach for preparing specific adsorbent for IgG separation. Journal of Biomaterials Science, Polymer Edition 25 (2014) 881–894.
46. Kartal F, Denizli, A. Surface molecularly imprinted magnetic microspheres for the recognition of albumin. Journal of Separation Science 37 (2014) 2077–2086.
47. Derazshamshir A, Baydemir G, Andac M, Say R, Galaev IY, Denizli A. Molecularly Imprinted PHEMA–Based Cryogel for Depletion of Hemoglobin from Human Blood. Macromolecular Chemistry and Physics 211 (2010) 657–668.

Hittite Journal of Science and Engineering, 2014, (1) 1 27-36
ISSN NUMBER: 2149-2123
DOI: 10.17350/HJSE19030000005

Thermodynamic Analysis of A Heat Pump for Different Refrigerants

Saban Tamdemir and Ali Kilicarslan[*]
Hitit University, Department of Mechanical Engineering, Corum, TURKEY

Article History:
Received: 2014/11/22
Accepted: 2014/12/24
Online: 2014/12/31

***Correspondence to**: Ali Kilicarslan,*
Hitit University, Faculty of Engineering,
Department of Mechanical Engineering,
Corum, Turkey
Tel: +90 (364) 227-4533 (1236)
Fax: +90 (364) 227-4535
E-Mail: alikilicarslan@hitit.edu.tr

ABSTRACT

In this study, the air to air heat pump that was installed to a room having dimensions of 6000x4000x3800 mm, was tested between the outdoor temperatures of -5°C and 5°C for different refrigerants , namely R134a, R404A, R407C and R410A. The electric power drawn by the compressor, indoor unit and outdoor unit fans, temperatures and pressures at the state points were measured. Experiments at the same outdoor temperatures were repeated three times under the controlled conditions. Analyses of the results obtained from the experiments were carried out by the computer code that was developed by means of Engineering Equation Solver (EES-V9.172-3D). The power consumed by the compressor, heating capacity of indoor unit, the absorbing heat capacity of outdoor unit, coefficient of performance of the heat pump, suction and discharge pressures of the compressor were investigated according to the outdoor temperatures. As the outdoor air temperature increased, the power consumed by the compressor increased whereas the indoor unit and outdoor unit capacities and coefficient of performance of the heat pump decreased on average. R134a is the most favourable refrigerants among the refrigerants under study due to consuming the least compressor power and having the highest coefficient of performance

Key Words:
Refrigeration; Heat Pump; Performance; Energy Analysis

INTRODUCTION

Heat pumps are the systems delivering the heat from the low temperature source, to the high temperature source. According to the second law of thermodynamics, the heat does not spontaneously flow from a sink at a lower temperature to a source a at higher temperature source. The energy is required to provide this heat flow. Heat pump supplies this energy by using the electrical energy (mechanical heat pump) or heat energy (thermal heat pumps) [1].

Heat pumps are used in the areas of heating, refrigerating and air conditioning. Furthermore, they are used for meeting the hot water needs. Heat pumps differ from each other in terms of the source that they used (air, water, soil, etc.) and the heat that they conduct [2]. Air source heat pumps are employed with the applications of different heating systems such as a floor heating system, radiator heating system for homes, etc. and provide an optimum comfort conditions. The hot water needs are met throughout the year. In addition to the ease of installation, they also do not require a high-cost drilling. They are used in the limited areas because of having a small outdoor unit [3]. The performance of a heat pump was experimentally carried out by using R432a as a refrigerant instead of R22 and it was observed that the performance and heating capacity of the heat pump increased between 8.5% - 8.7% and 1.9% - 6.4%, respectively [4].

The performance of a heat pump using a near azeotropic refrigerant R431a that is a mixture of 71% propane and 29% R152a was experimentally compared with that of a heat pump using R22 as refrigerant. According to the experimental results, it was seen that the performance of the heat pump with R431a is higher by 3.5% - 3.8% than that of the heat pump with R22 at the same operating conditions [5]. The effects of two different airflow consisting of 75% and 100% of nominal air flow and refrigerant R410a charge, namely 75%, 100%, and 125% of regular value of an air on the performance of an source heat pump were experimentally carried out. It was observed that the increase in refrigerant charge while keeping the airflow constant at the rated value increased the COP by 5% at the heating season. However, the decrease in both air flow and refrigerant charge decreased the COP by 10% [6]. In a case study carried out in Beijing, China, a different prototype air source heat pump (ASHP) was designed and manufactured, it was observed that ASHP has a higher performance and heating capacity with the snowy days having high relative humidities and temperatures of around -12 °C.

In this study, the performance of a air source heat pump was experimentally carried out for refrigerants R134a, R404a, R407c and R410a at various outdoor air temperatures. It was seen from the literature survey that there are few studies concerning with ASHP in which R407c and R410a are used as refrigerants. Furthermore, it was seen that the performance of heat pumps were compared in terms of refrigerants as the studies in the literature was investigated. But this study also aims to observe the coefficient of performance of ASHP at different outdoor temperatures.

THEORETICAL STUDY

The first law of thermodynamics for a control volume can be written as [8],

$$\dot{Q}_{cv}=(dE_{cv} / dt) + \sum\dot{m}_e (h+(v^2/2)+gz)_e - \sum\dot{m}_i (h+(v^2/2)+gz)_i + \dot{W}_{cv} \quad (1)$$

Where;

dE_{cv} / dt: change of energy with respect to time within a control volume
$\dot{W}_{cv}$: work done per unit time by a control volume
$\dot{Q}_{cv}$: heat rate delivered to a control volume
h_i : enthalpy of the refrigerant at a control volume inlet
h_e : enthalpy of the refrigerant at a control volume exit

The following assumptions are valid for the air source heat pump (ASHP) under consideration,

- The flow of refrigerant throughout ASHP occurs at steady-state and steady-flow process.
- The heat transfer from the compressor is negligible.
- The electrical energy rate driven by the compressor is equal to the compression work per unit time.
- The changes in kinetic and potential energies in the elements of ASHP are negligible.
- Sub cooling occurs in the indoor unit, the pressure losses are negligible.

As the assumptions mentioned above are taken into consideration, the energy required for the compressor can be derived from Equation 1,

$$\dot{W}_{comp}=\dot{m}_r(h_2-h_1) \quad (2)$$

Where, $\dot{W}_{comp}$ is the energy rate driven by the compressor and is measured by the energy analyser, is the mass flow rate of the refrigerant throughout the ASHP, is the specific enthalpy at the compressor inlet and is the specific enthalpy at the compressor exit.

The capacity of the indoor unit $\dot{Q}_{iu}$ can be expressed as,

$$\dot{Q}_{iu}=\dot{m}_r(h_3-h_4) \quad (3)$$

Where, h_3 and h_4 are the specific enthalpies of the refrigerants at the inlet of the indoor unit and exit, respectively.

The heat transfer rate absorbed by the outdoor unit of the ASHP $\dot{Q}_{ou}$ can be written as

$$\dot{Q}_{ou}=\dot{m}_r(h_5-h_1) \quad (4)$$

Where, h_5 is the specific enthalpy of the refrigerant at the inlet of the indoor unit.

Coefficient of performance of the heat pump (COP_{hp}), a measure of ASHP, can be written as

$$COP_{hp} = \dot{Q}_{iu} / (\dot{W}_{comp} + \dot{W}_{iu} + \dot{W}_{ou}) \quad (5)$$

Where, W_{iu} and W_{ou} are the energies consumed by the fans of indoor and outdoor units, respectively. These energies are also measured by the energy analyser as in the energy consumed by the compressor. The number of revolutions per minute is constant for these fans, so the consumed energies by these fans are constant and given below,

$\dot{W}_{iu}$ = 0.176 kW

$\dot{W}_{ou}$ = 0.088 kW

EXPERIMENTAL

Experimental studies were performed in the one of the laboratories of the Department of Mechanical Engineering of Hitit University, having dimensions of 6000x4000x3800 mm and facing North.

The heating load of this laboratory is 5472 kcal. The indoor unit of the ASHP is shown in Figure 1 while the outdoor unit is shown in Figure 2.

Figure 1 also shows the energy analyser, data logger, manometers and thermocouple connections

ASHP mainly consists of semi hermetic compressor, air forced indoor and outdoor units, capillary type expansion valve. The auxiliary elements of the ASHP include four-way valve, high and low pressure switches and filter drier.

Uncertainty analysis of the study

There is a certain degree of uncertainty and error in every experiment. If the experiments are organized very precisely, the uncertainties and errors can be minimized in the experimental results. Three errors causing the uncertainty in the experimental results are presented by [9] as the error caused by person during reading the result from the experimental apparatus, the errors related to the primary and secondary part of the measuring apparatus.

Figure 1. Indoor unit of the ASHP

According to the uncertainty analysis, R is the parameter that must be measured during the experiments, and x_1, x_2, x_3 …………,x_n are the independent parameters affecting R. R can be expressed as a function of the independent parameters [10],

Figure 2. Outdoor unit of the ASHP

$$R= R(x_1,x_2,x_3 \ldots\ldots\ldots x_n) \quad (6)$$

w_1, w_2, w_3,…………, w_n are the uncertainty values related to every independent parameters and W_R , the uncertainty value of measured parameter R, can be written as

$$W_R=[(\partial RW_1/\partial x_1)]^2+ [(\partial RW_2/\partial x_2)]^2+\ldots\ldots+[(\partial RW_n/\partial x_n)]^2 \quad (7)$$

During the experiments that were carried out, the uncertainty values associated with the measured values were inserted into Equation 7 and the total values of the uncertainties were obtained as it is shown in Table 1.

RESULTS AND DISCUSSION

Air source heat pump (ASHP) was tested for different refrigerants including R134a, R404a, R407c and R410a at different outdoor air temperatures between -5°C and 5°C. A computer code was developed to analyze results by using Engineering Equation Solver (EES-V9.729-3D) that is commonly used in thermal systems [11]. The heating capacity of indoor unit, the amount of heat absorbed by outdoor unit, the energy consumed by the compressor, coefficient of performance of the ASHP, compressor suction and discharge pressures were investigated as a function of outdoor air temperatures for different refrigerants.

Figure 3 shows the change of compressor suction (inlet) pressure of ASHP with respect to the outdoor air

Table 1. Total uncertainties occurring in the experiments

Total uncertainties related to the measured parameters	Total value of uncertainty
Total uncertainties associated with the mass flow rate (W_m)	3.1%
Total uncertainties associated with the capacity of indoor unit (W_{Qiu})	3.1%
Total uncertainties associated with the capacity of outdoor unit (W_{Qou})	3.1%
Total uncertainties associated with the compressor power (W_{Wcomp})	1.3%
Total uncertainties associated with the coefficient of performance (W_{CoPhp})	3.3%

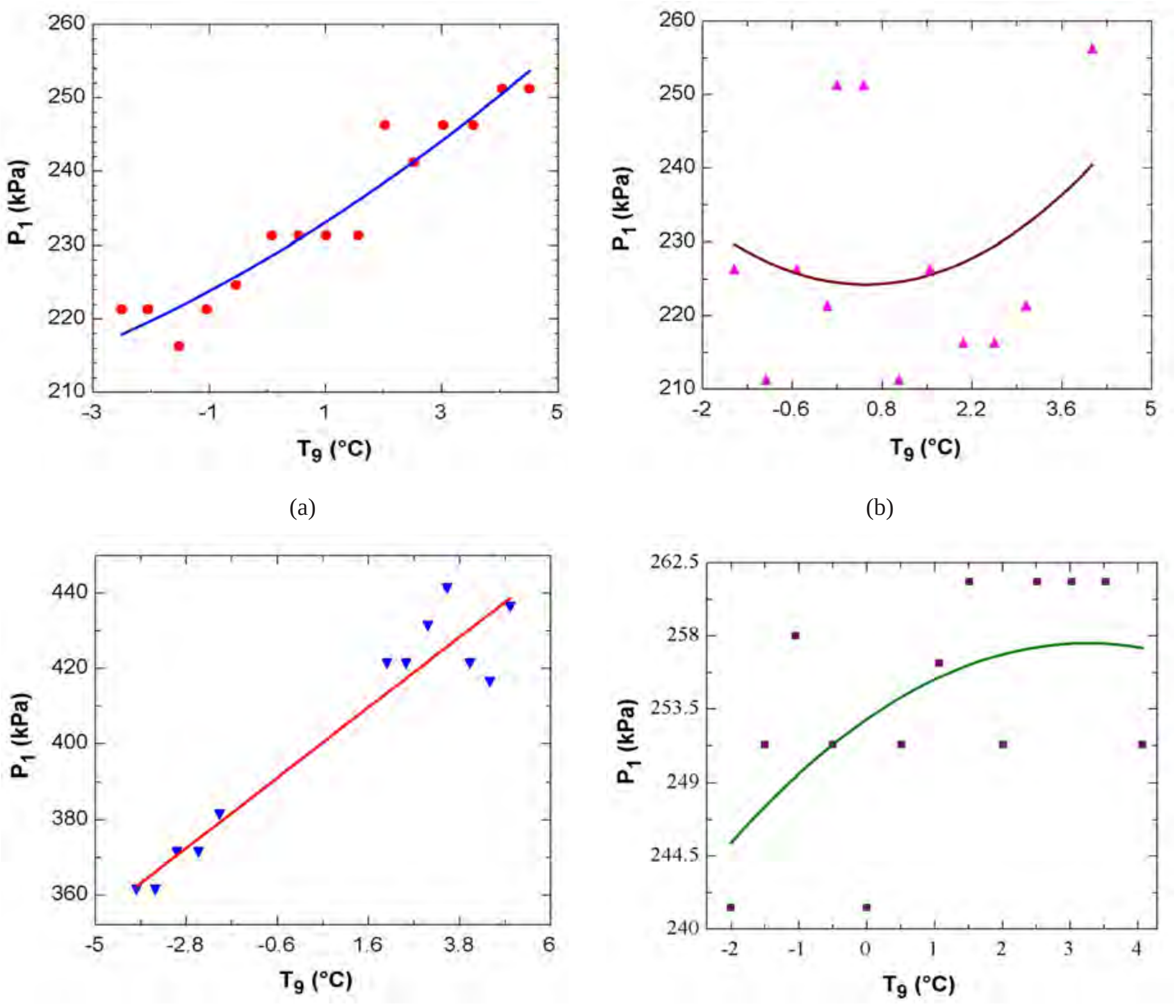

(a) (b)

(c) (d)

Figure 3. Compressor suction pressure as a function of outdoor air temperature a) R134a, b) R404a, c) R407c, d) R410a

temperature for various refrigerants. As it is shown in Figure 3 that as the outdoor air temperature increases, the suction pressure of ASHP increases for all of the refrigerants except for refrigerant R404a under the study. The suction pressure firstly decreases and reaches to a minimum value increase, then increases for refrigerant R404a. As the outdoor air temperature increases, the amount of heat transfer to the outdoor coil increases, thereby increasing the saturation temperature of the refrigerant. This causes the saturation pressure, in other words, compressor inlet pressure corresponding to this temperature to increase. As shown in Figure 3a for refrigerant 134a, as the outdoor air temperature changes between -2.5°C and 4.5°C, the suction pressure of ASHP changes between 221 kPa and 251 kPa. In the case of R404a, when the outdoor air changes from -1.5°C to 4.0°C, the compressor suction pressure changes from 225 kPa to 235 kPa. The increase in suction pressure for refrigerant R134a is 13.5% while it is 4.44% for R404a as it is shown in Figure 3b.

Figure 3c shows that the experimental measurements were not obtained at the outdoor air temperatures between -2.0°C and 2.0°C because of weather conditions. As shown in Figure 3c, at the temperatures between -4.0°C and 5.0°C, the compressor suction pressure varies from 355 kPa to 430 kPa for refrigerant R407c and the increase in the pressure is 20% while the increase in the suction pressure is 5.52% for refrigerant R410a for the temperatures between -2.0°C and 4.0°C (Figure 3d). Figure 3 also shows that the maximum values of compressor suction pressures are obtained for R407c while the minimum ones are obtained for R404a.

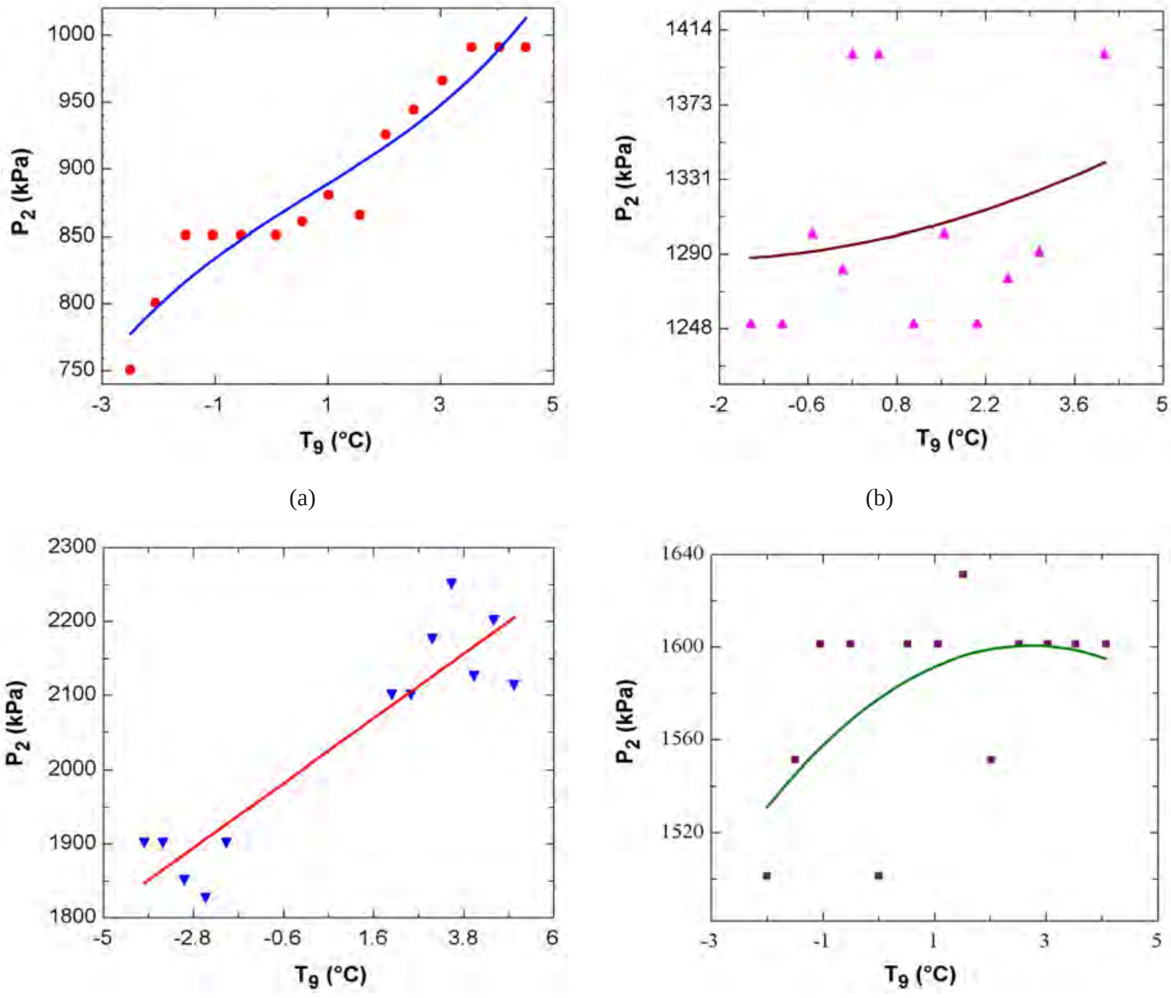

(a) (b)

(c) (d)

Figure 4. Compressor discharge pressure as a function of outdoor air temperature a) R134a, b) R404a, c) R407c, d) R410a

The change of compressor discharge pressure of the ASHP with respect to the outdoor air temperature for the refrigerants including R134a, R404a, R407c and R410a is depicted in Figure 4. The heat transfer to the refrigerant because of increasing outdoor air temperature also causes the compressor discharge pressure to increase for all the refrigerants as in the case of the compressor suction pressure as it is shown in Figure 4. The maximum compressor discharge pressures, changing between 1850 kPa and 2200 kPa, are obtained as refrigerant 407c is used in the ASHP cycle while the minimum ones, changing between 7750 kPa and 1025 kPa, are obtained by using R134a as refrigerant in the cycle.

Figure 4 also shows that the discharge pressures of the ASHP lie in the middle range for the refrigerants, namely R404a and R410a. The discharge pressure values change between 1290–1345kPa for refrigerant R404a and 1520 –1610 kPa for refrigerant R410a. The maximum rate of increase in compressor discharge pressure occurs by using R134a as refrigerant in the cycle at the outdoor temperatures between -2.5°C and 4.5°C while the minimum occurs by using R410a at the temperatures between -1.5°C and 4°C.

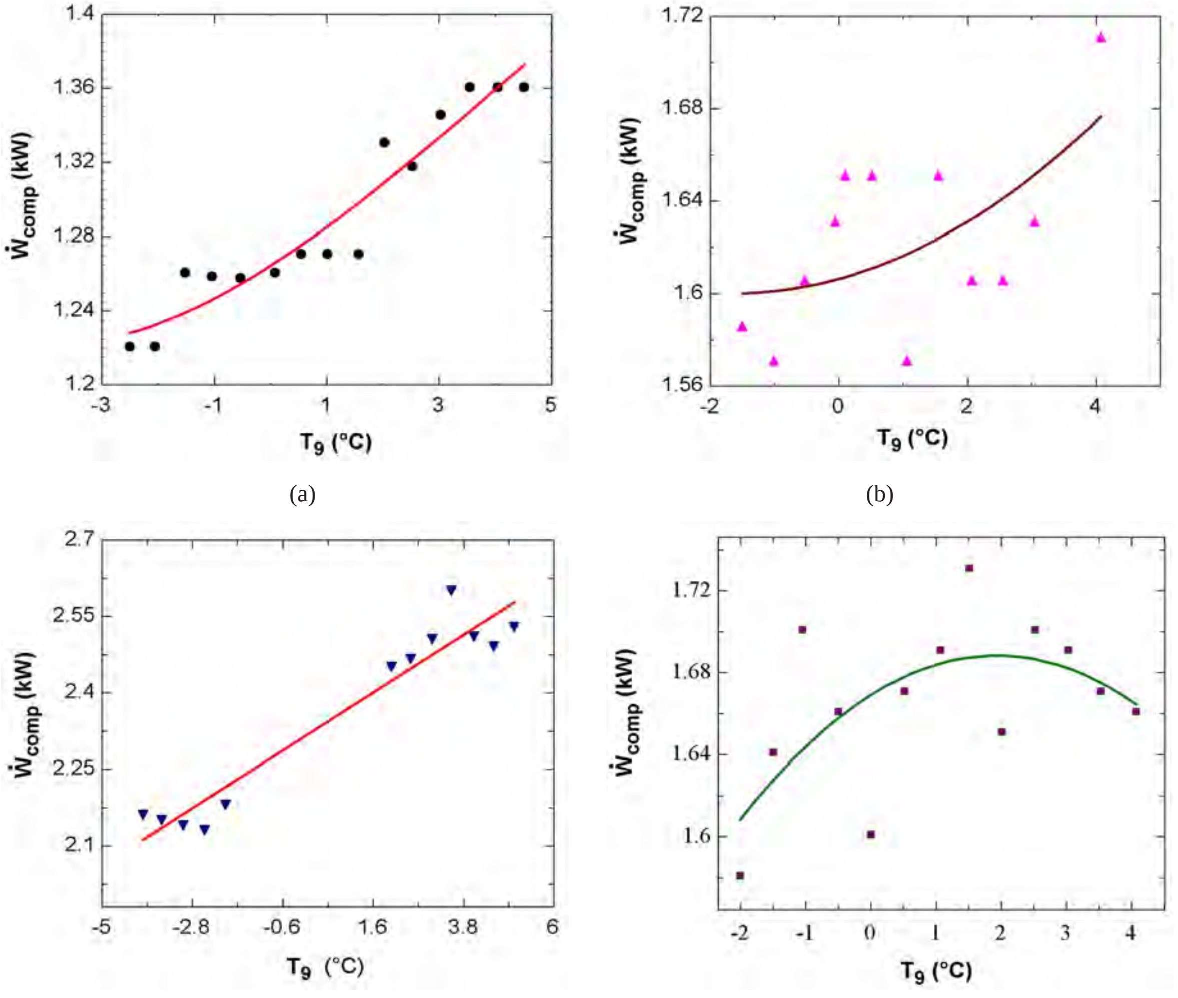

(a) (b)

(c) (d)

Figure 5. The power required for the compressor versus outdoor air temperature a) R134a, b) R404a, c) R407c, d) R410a

The variation of the power required for the compressor as a function of outdoor air temperature for refrigerants R134a, R404a, R407c and R410a is depicted in Figure 5. As the outdoor air temperature increases, the pressure ratio across the compressor also increases. This causes the power required for the compressor to increase as shown in Figure 5. At the outdoor air temperatures between -2.5°C and 4.5°C, the power consumed by the compressor increases by 11.4% as refrigerant R134a is used in the ASHP cycle as shown in Figure 5a whereas the power increases by 5% for refrigerant R404a as depicted in Figure 5b. The maximum amount of power, namely approximately 2.5 kW is consumed in the ASHP cycle as refrigerant 407c is used as refrigerant at an outdoor temperature of 5°C as it is shown in Figure 5c while the minimum power, namely approximately 1.23 kW is consumed in the cycle for refrigerant R134a at an outdoor temperature of -2.5°C.

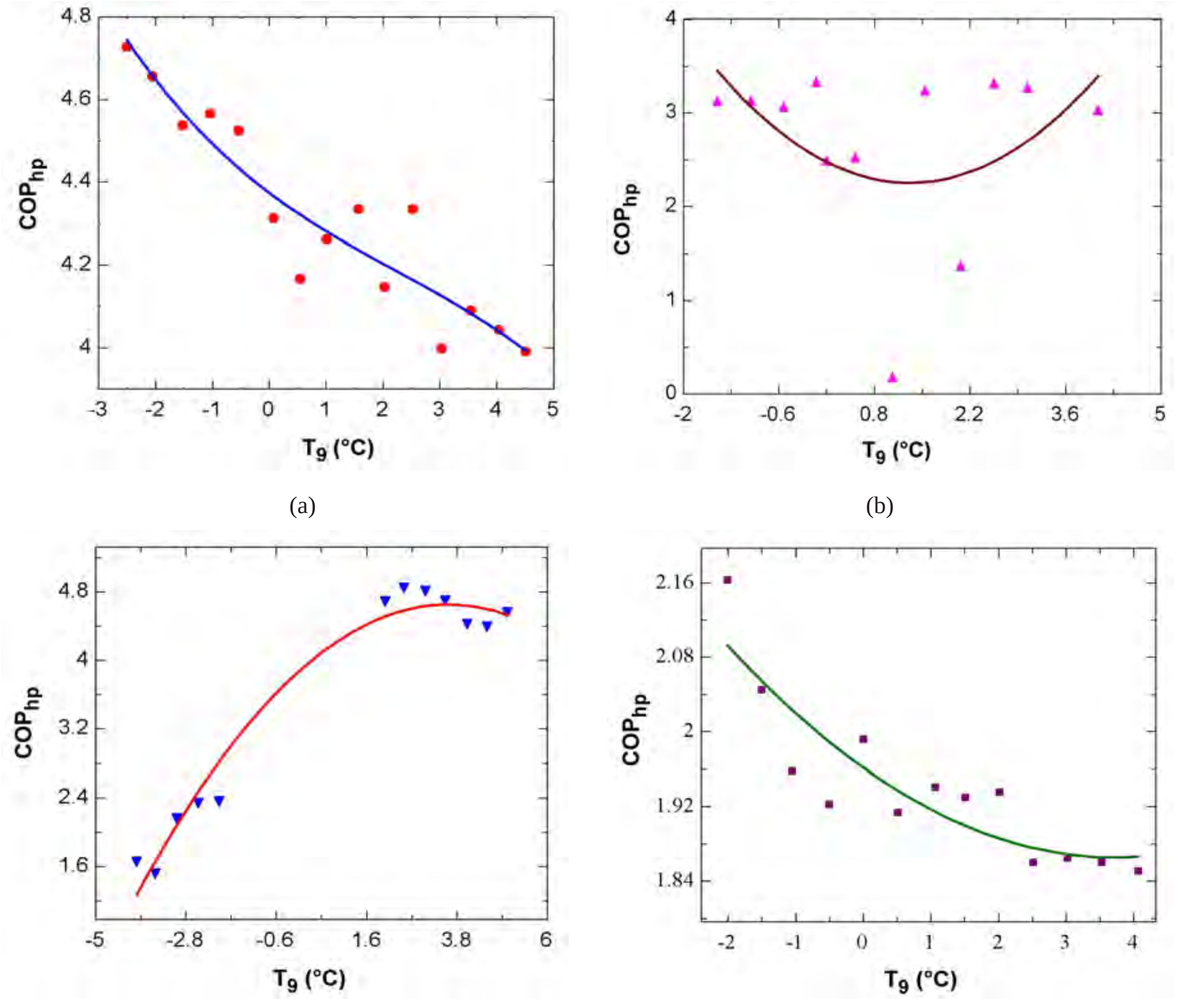

(a) (b)

(c) (d)

Figure 6. The coefficient of performance of the ASHP versus outdoor air temperature a) R134a, b) R404a, c) R407c, d) R410a

Figure 6 shows the coefficient of performance of the ASHP as a function of outdoor air temperature for refrigerants R134a, R404a, R407c and R410a. The coefficient of performance of the ASHP increases for all the refrigerants except for refrigerant R407c as the outdoor air temperature increases. At the increasing values of outdoor temperatures, the energy required for the compressor increases, but the capacity of indoor unit decreases, thereby decreasing the coefficient of performance of the ASHP as it is shown in Figures 6a, 6c and partly 6b. But, for refrigerant R407c, the coefficient of performance of ASHP decreases because of increasing the capacity of indoor unit at higher outdoor temperatures.

The coefficient of performance firstly decreases between until the outdoor temperature reaches 1°C and then increases between 1.0°C and 4.0°C for refrigerant R404a. The coefficients of performance of the ASHP ranging from 4 to 4.8 are obtained by using R404a as a refrigerant in the cycle while those ranging from 1.85 to 2.1 are obtained by using R410a.

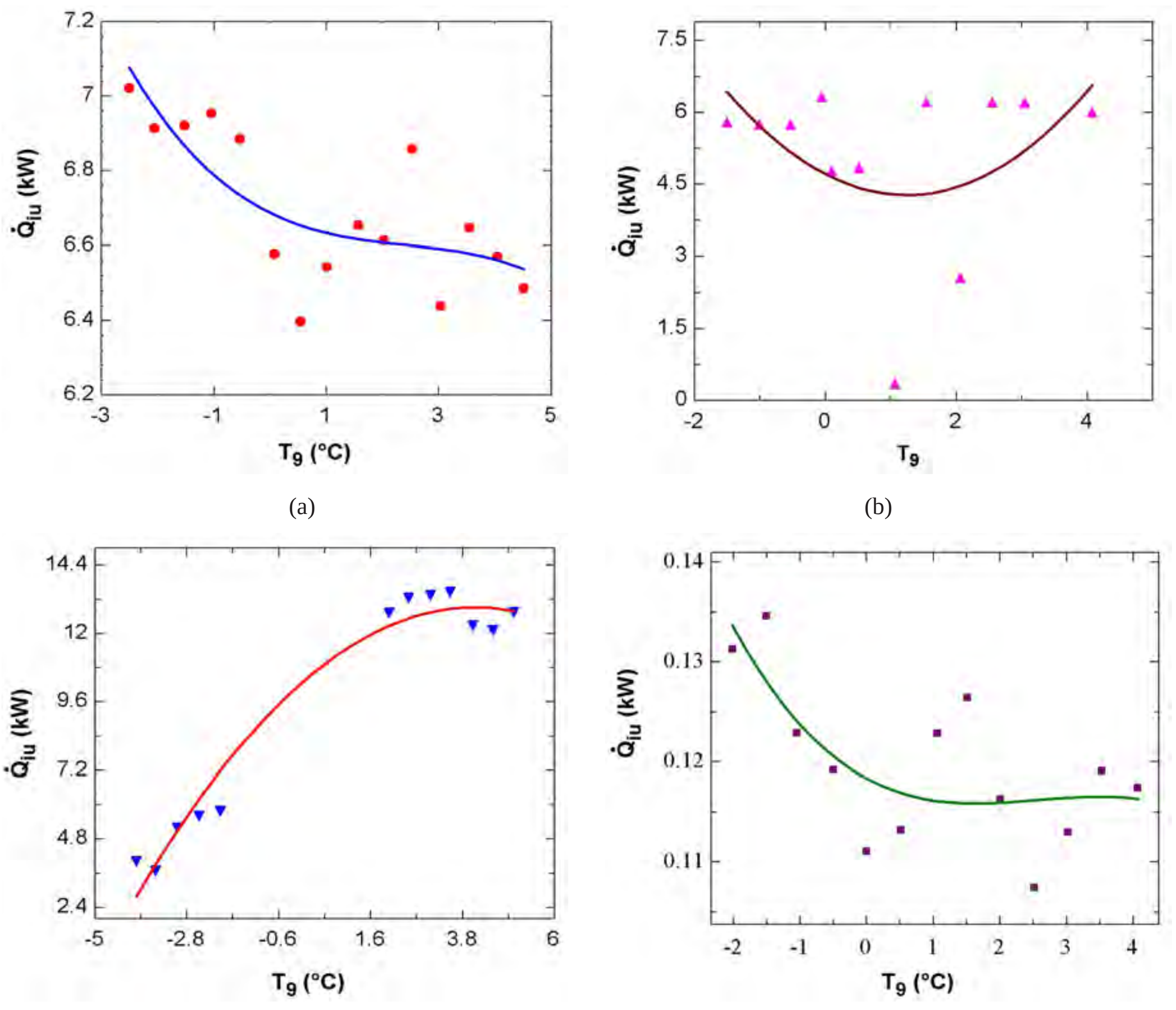

(a)

(b)

(c)

(d)

Figure 7. The capacity of indoor unit of the ASHP versus outdoor air temperature a) R134a, b) R404a, c) R407c, d) R410a

The change of the capacity of the indoor unit of the ASHP as a function of outdoor air temperature for refrigerants R134a, R404a, R407c and R410a is depicted in Figure 7. The capacity of the indoor unit decreases at the outdoor air temperatures between -2.5°C and 4.5°C for refrigerant R134a as it is depicted in Figure 7a. In the mentioned temperature range above, the capacity decreases on average by 7.60%. For refrigerant R404a, the capacity firstly decreases between the temperatures of -1.5°C and 1.0°C and it has a minimum value of 4kW corresponding of 1.0°C and then increases between 1.0°C and 4.0°C as shown in Figure 7b. Figure 7c shows that the capacity of indoor unit ranges from 3 and 13 kW for refrigerant R407c at the outdoor air temperatures between -4.0°C and 5°C. At the outdoor air temperatures between -2.0°C and 1.5°C, the capacity of indoor unit decreases on average by 14.81 and there is a small increase in the capacity after a temperature of 2.0 °C for refrigerant R410a as it is shown in Figure 7d.

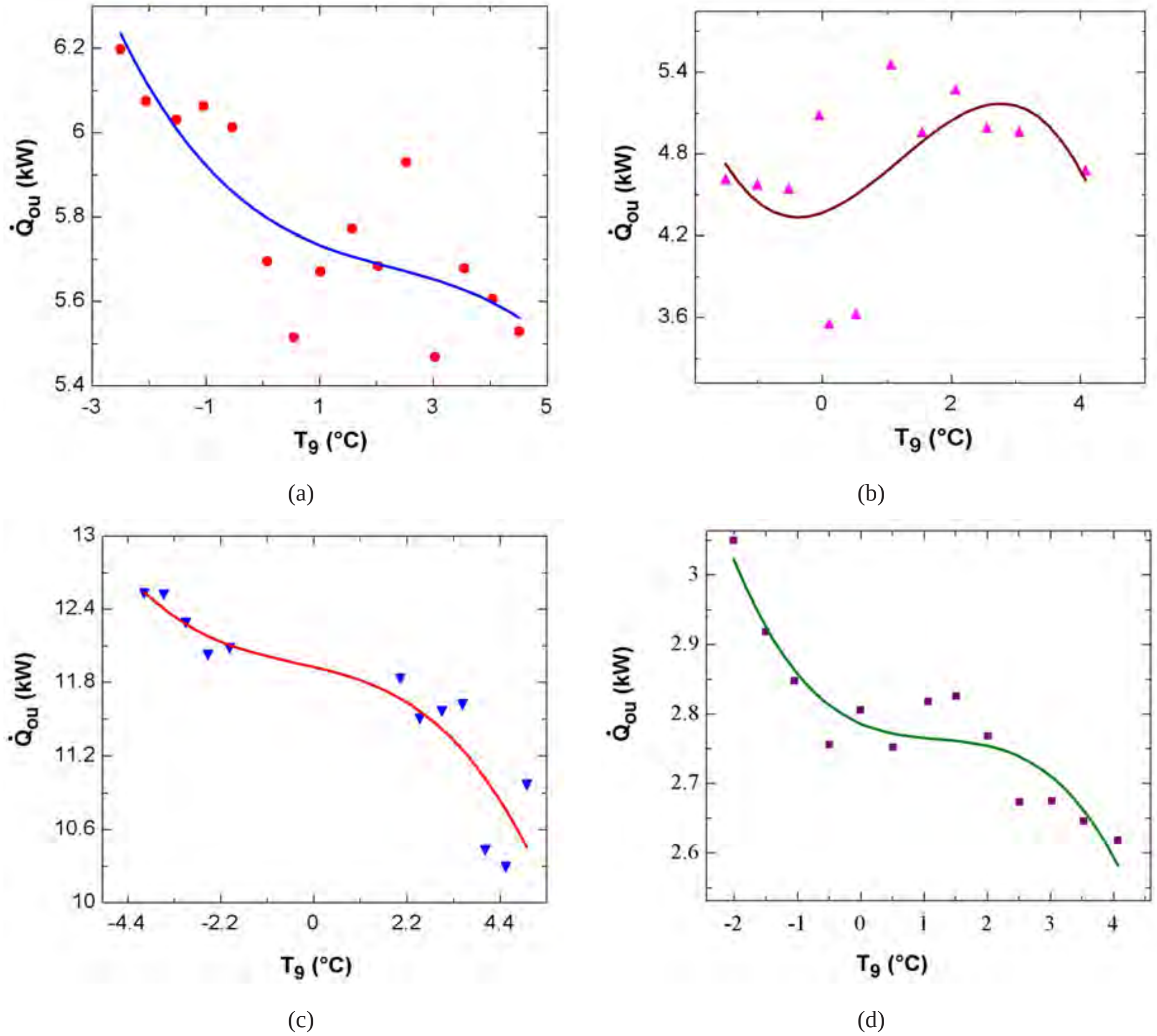

Figure 8. The capacity of outdoor unit of the ASHP versus outdoor air temperature a) R134a, b) R404a, c) R407c, d) R410a

Figure 8 depicts the change of the capacity of outdoor unit of the ASHP with respect to the outdoor air temperature for refrigerants R134a, R404a, R407c and R410a. The capacity of the outdoor unit decreases for all the refrigerants except for refrigerant R404a as the outdoor air temperature increases. The capacity of outdoor unit firstly decreases and then increases on average for refrigerant R410a as the outdoor air temperature increases. As it is shown in Figure 8a that the outdoor unit capacity has a maximum value, namely 6.2 kW at an outdoor temperature of -2.5°C for refrigerant R134a and then the capacity decreases, and approximately reaches a minimum value of 5.5 kW at an outdoor temperature of 5°C. Among the refrigerants under study, the maximum outdoor unit capacities ranging from 10.5 kW to 12.5 kW are obtained by employing R407c as a refrigerant in the ASHP cycle as depicted in Figure 8c while the minimum values ranging from 2.6 kW to 3 kW are obtained with refrigerant R410a (Figure 8d).

CONCLUSIONS

An air source heat pump was tested for refrigerants R134a, R404a, R407c and R410a at outdoor air temperatures ranging from -5°C to 5°C. The main conclusions are summarized below.

Compressor suction pressure of the ASHP increases as the outdoor air temperature increases. The maximum pressure increase in the compressor suction pressure, namely 21.4% is obtained by employing R407c as a refrigerant in the ASHP cycle while the minimum increase, namely 4.44% is obtained with refrigerant R404a. The values of increase in the compressor suction pressure for refrigerants R134a and R410a are 13.5% and 5.52%, respectively. The compressor suction pressure ranges from 355 to 430 kPa for refrigerant R407c and from 355 to 430 kPa for refrigerant R404a.

- Compressor discharge pressure of the ASHP also increases at increasing values of outdoor air temperatures. The maximum pressure increase in the compressor suction pressure, namely 32% is obtained by employing R134a as a refrigerant in the ASHP cycle while the minimum increase, namely 4.74% is obtained with refrigerant R404a. The values of increase in the compressor suction pressure for refrigerants R407c and R410a are 18.91% and 5.92%, respectively.
- The electrical power delivered to the compressor (compressor power) increases parallel to the pressure ratio of the compressor as the outdoor air temperature increases. The compressor power has the maximum value of increase ratio, namely 21.4% for refrigerant R407c while the minimum ratio, 3.65% is obtained for R410a and it ranges from 2.1 to 2.55 kW for R407c and from 1.63 to 1.69 kW for R410a.

  The increase ratio in the compressor power is 11.4% for refrigerant R134a and 5% for refrigerant R404a, respectively.
- The heating capacity of indoor unit, in other words, the heat rejected to the room to be heated, has a maximum value of 15 kW for refrigerant R407c and a minimum value of 0.115 kW for refrigerant R410a.
- The heat absorbed from the outdoor air (the outdoor unit capacity) is maximum, namely 12.5 kW for refrigerant R407c and is minimum, 2.65kW, for refrigerant R410a.

ACKNOWLEDGMENTS

We are grateful to Hitit University Scientific Research Projects Unit for supporting this project numbered (MUH03.12.001)

REFERENCES

1. Dursun B. Soğuk iklim koşullarında ısı pompalarının kullanımı, Yüksek Lisans Tezi, Atatürk Üniversitesi Fen Bilimleri Enstitüsü Makine Mühendisliği Ana Bilim Dalı, Erzurum, 2006.
2. Ceylan T. İki katlı bir binanın güneş enerjisi destekli hava kaynaklı ısı pompası ile ısıtılması ve sıcak su eldesinin analizi. Yüksek Lisans Tezi, Gazi Üniversitesi Fen Bilimleri Enstitüsü, Ankara, 2010.
3. Özyirmidokuz MH. Hava kaynaklı ısı pompası ve ekserji analizi. Yüksek Lisans Tezi, Erciyes Üniversitesi Fen Bilimleri Enstitüsü, Kayseri, 2010.
4. Park KJ, Shim YB, Jung D. Experimental performance of R432A to replace R22 in residential air–conditioners and heat pumps. Applied Thermal Engineering, 29 (2009) 597-600.
5. Park KJ, Shim YB, Jung D. A 'drop–in' refrigerant R431A for replacing HCFC22 in residential air–conditioners and heat pumps. Energy Conversion and Management, 50 (2009) 1671-1675.
6. Palmiter L, Kim JH, Larson B, Francisco PW, Groll E. A.l, Braun J.E. Measured effect of airflow and refrigerant charge on the seasonal performance of an air–source heat pump using R–410A, Energy and Building, 43 (2011) 1802–1810.
7. Wang R, Xie G, Wu Q, Wu Y, Yuan J. An air source heat pump with an advanced cycle for heating buildings in Beijing, Energy Conversion and Management, 52 (2011), 1493-1500.
8. Wylen GJV, Soontag RE. Fundamentals of Classical Thermodynamics, John Wiley&Sons, New York, 1985.
9. Schenck Jr H. Theories of Engineering Experimentation, McGraw–Hill Book Company, USA, 1968.
10. Kline SJ, McClintock FA. Describing uncertainties in single–sample experiments. Mechanical Engineering, 75 (1953) 3–8.
11. Klein SA. Engineering Equation Solver (EES), Professional version V9.723–3D, F–Chart Software (2010).

Hittite Journal of Science and Engineering, 2014, (1) 1 37-41
ISSN NUMBER: 2149-2123
DOI: 10.17350/HJSE19030000006

Antioxidant and Antimicrobial Activities with GC/MS Analysis of the *Morus alba* L. Leaves

Asiye Aslı Emniyet[1], **Emre Avcı**[2], **Burcin Ozcelik**[1,*], **Gulcin Alp Avcı**[2] **and Dursun Ali Kose**[3]
[1] Hitit University, Department of Biology, Corum, TURKEY
[2] Hitit University, Department of Molecular Biology and Genetics, Corum, TURKEY
[3] Hitit University, Department of Chemistry, Corum, TURKEY

ABSTRACT

Morus alba L. (Moraceae) leaves are used effectively to treat fever, protect liver from damage, strengthen the joints, facilitate discharge of urine in Turkey folk medicine. In this study we aimed to determine in vitro antioxidant and antimicrobial activity with GC/MS analysis of the *Morus alba* L. leaves. Dried plant leaves samples are milled and extracted with distilled water and ethanol in Soxhlet machine. After extraction, extract samples were concentrated in rotary evaporator machine. Total antioxidant status values were determined as mmol Trolox Equivalent/L spectrophotometrically by using Erel's method. Sterile extracts were used to avoid contamination in antimicrobial activity test. As test microorganisms *Escherichia coli* (ATCC 25922), *Staphylococcus aureus* (ATCC 25923), *Enterococcus faecalis* (ATCC 29212), *Pseudomonas aeroginosa* (ATCC 27853), *Candida albicans* (ATCC 90028) were used. Antimicrobial activity was determined with disc diffusion method. We used ethanol extracts of samples in GC/MS analysis. Ethanol and distilled water extracts showed antioxidant activity in different rate. Besides, ethanol extracts have an antimicrobial activity but water extracts have not antimicrobial activity on our test microorganisms. We determined four compounds (9,12,15-octadecatrienoic acid, ethyl ester, linolenic acid ethyl ester, gibberellic acid) with GC/MS analysis in ethanol extracts.

In this research we enlightened antimicrobial and antioxidant activities with GC/MS analysis of *Morus alba* L. leaves. So this research supports of using this plant leaves in pharmacological and medical processes.

Key Words:
Antioxidant activity; Antimicrobial activity; GC/MS analysis; *Morus alba* L.; Extraction

Article History:
Received: 2014/11/11
Accepted: 2014/12/29
Online: 2014/12/31

Correspondence to: *Burcin Ozcelik,*
Hitit University, Faculty of Arts and Science,
Department of Biology, Corum, Turkey
Tel: +90 (364) 227 70 00 (1715)
Fax: +90 (364) 227 70 05
E-Mail: burcinozclk@gmail.com.tr
burcinozcelik@hitit.edu.tr

INTRODUCTION

Morus alba L. belongs to the Moraceae family, is widely cultivated and naturalized elsewhere and is one of the most important medicinal plant [1]. The mulberry (*Morus alba* L.) fruit is widely regarded as a nutritious food. Root, stem barks, twigs and leaves of mulberry have long been used in traditional medicine to treat fever, inflammation, hepatitis, cancer, diabetes, dislipidemia, diarrhoea, dyspepsia, hypertension, anthelmintic and to protect the liver, improve eyesight, strengthen joints, facilitate discharge of urine, and lower blood pressure. Different parts of the mulberry have been extensively investigated for their various health benefits, including antioxidative, hypolipidemic and antiatherogenic effects [2-4].

Besides, this genus is known to be rich in flavonoids [5].

Reactive oxygen species (ROS) are produced in metabolic and physiological processes, and causes different chronic diseases like cancer and heart diseases [6]. Antioxidant molecules prevent such these harmful reactions [7]. All biological systems, including human beings, have antioxidant defence mechanisms. Since these natural antioxidant mechanisms can be inefficient, dietary intake of antioxidant compounds is important [8]. Mulberry leaf extract has been demonstrated to contain several substances that can act as potent antioxidants or free radical scavengers such as flavonoids and moracins [9].

Many plants contain a diverse array of compounds such as phenolic acids, flavonoids, tannins, vitamins, and terpenoids that account for their biological properties and the antioxidant and antimicrobial abilities [10,11]. In addition, plant and plant products can be used for isolating health-promoting bioactive compounds that have antioxidant, hypoglycemic, hypotensive and hypocholesterolemic effects [12]. For a few years, many researchers have intensively investigated antimicrobial properties of plant extracts and natural products as the demand for safe and new pharmaceuticals which has increased due to the misuse of antibiotics and an increase in immuno-deficiency [13].

In the present study, we aimed 1) to examine the antioxidant capacities of distilled water and ethanol extracts of *Morus alba* L. leaves, 2) to measure the antimicrobial activity of leaf extracts against five test microorganisms, 3) to determine main components of extracts with GC/MS analysis method.

MATERIALS AND METHODS

Plant Sample Collection

Morus alba L. leaves were collected from natural areas. Samples were identified by plant taxonomist Prof. Dr. Murat Ekici of the Department of Biology, Gazi University, Ankara. All plant samples were dried at room temperature in a few days.

Preparation of Extracts

Dry leaves were milled. To prepare extract two different solvent were used, ethanol and distilled water respectively, and 10 g sample weigh for each extraction. Extraction was made with soxhlet machine during 8 hours. After from extraction process, solvents were concentrated in rotary evaporator machine. Sterile extracts were used to avoid contamination in antimicrobial activity test. For this reason, extracts were filtered with micro filter which has 0.45 micrometer pore diameter. Extracts were protected from light and kept in +4°C until executing the experiments.

Determination of Total Antioxidant Status (TAS)

The total antioxidant status (TAS) was determined using a TAS Assay Kit (Rel Assay Diagnostics®, Gaziantep, Turkey) according to a novel automated measurement method developed by Erel in 2004 [7]. In this method, a hydroxyl radical was produced by the Fenton reaction and reacted with the colourless substrate o-dianisidine to produce the bright yellowish-brown dianisyl radical. For this procedure, 500 µL of reagent 1 was placed in the cell, and 30 µL of sample (standard) was added. The initial absorbance at 660 nm for the first absorbance point was measured in a spectrophotometer (Shimadzu UV mini-1240, Kyoto, Japan). Subsequently, 75 µL of reagent 2 was added to the cell and incubated for 10 min at room temperature. The absorbance at 660 nm was read for a second time. The results obtained from this process were calculated with the following formulas:

Results = [(ΔAbs Std 1)–(ΔAbs Sample)]/ [(ΔAbs Std 1)–(ΔAbs Std2)]

ΔAbsorbance Standard 1= (Second Absorbance of Std 1-First Absorbance of Std 1)

ΔAbsorbance Standard 2= (Second Absorbance of Std 2-First Absorbance of Std 2)

Δ Sample Absorbance = (Second Absorbance of Sample-First Absorbance of Sample)

The results were expressed as milimolar Trolox equivalents per liter (mmol Trolox Eq/L).

Determination of Antimicrobial Activity

As test microorganisms *Escherichia coli* (ATCC 25922), *Staphylococcus aureus* (ATCC 25923), *Enterococcus faecalis* (ATCC 29212), *Pseudomonas aeroginosa* (ATCC 27853), *Candida albicans* (ATCC 10231) were used. All strains were obtained from culture collection at Hitit University, Faculty of Science and Arts, Department of Molecular Biology and Genetic, Microbiology Research Laboratory Culture Collection.

The antimicrobial activities were evaluated by disc-diffusion method. Microorganisms were activated two times in nutrient broth and incubated for 16-24 hours at 37°C temperature. After activation of cultures, optical density (OD) arranged spectrophotometrically in 600 nanometer wavelength. Activated ($OD_{600} \approx 600$) microorganisms were inoculated nutrient agar and were spread all agar surface with drigalski bar. Sterile discs which were prepared from Whatman Filter paper were put and extracts were added to these discs in different volume, 10 and 20 microliter respectively. These petri dishes were incubated for 16-24 hours at 37°C temperature. When incubation time completed, all petri dishes were investigated. All antimicrobial activity zones were measured with ruler.

Gas Chromatography/Mass Spectrometry (GC/MS) Analysis of Extracts

The chemical compositions of the plant extracts were analysed by using GC–MS technique and the fragmentation analysis was performed. The mass spectrometer was Thermo Scientific DSQ II Single Quadrupole GC/MS in the electron impact (EI) ionization mode (70 eV) and HP- 5MS (bonded and cross-linked 5% phenyl-methylpolysiloxane, 30mm x 0.25 mm, coating thickness 0.25 μm) capillary column (Restek, Bellefonte, PA). Injector and detector temperatures were set at 220°C. The oven temperature was held at 50°C for 30 min, then programmed to 240°C at rate of 3°C/min. Helium (99.99%) was the carrier gas at a flow rate of 1 mL/min. The molecular weight of decomposition products scan 60-200 g/mol range were performed. Diluted samples (1/100 in chloroform, v/v) of 1.0 μL were injected manually. The identification of components was based on the comparison of their mass spectra with those of Wiley 7 N (contains 392.086 compounds spectra), NIST 2002 (contains 174.948 compounds spectra) and flavor (contains 419 compounds spectra) libraries and as well as by comparison of their retention times.

Statistical Analysis

All experiments were done in triplicate. The results were expressed as average ± standard deviations (SD). Statistical analysis was performed on the data by SPSS 15.0 Bivariate Correlation Analysis (SPSS Inc., Chicago). Between ethanol and distilled water extracts were found significant statistically correlation at the 0.01 level.

RESULTS AND DISCUSSION

Determination of Total Antioxidant Status (TAS) of Extracts

Antioxidant components of plants have attracted great interest for the prevention and treatment of complex diseases such as cardiovascular diseases, cancer, diabetes, AIDS, Alzheimer's diseases [14]. Additionally, it was stated in the literature that several types of plant materials such as vegetables, fruits, leaves, seeds, roots and stem barks are the potential sources of antioxidant compounds [15]. The TAS values of *Morus alba* L. leaves for ethanol and distilled water extracts were shown in Table 1. TAS values of ethanol extract of *Morus alba* L. leaves displayed higher capacity than distilled water extract. While TAS values of leaf-ethanol extract was found as 1.56 mmol Trolox Eqv./L, TAS values of leaf- distilled water extract were found as 1.45 mmol Trolox Eqv./L. While the recent report that suggests the antioxidant activity of distilled water extract was better than ethanol extract with DPPH assay, we found better TAS value for ethanol extract with Erel's method [16].

Table 1. TAS levels in *Morus alba* L. leaves extracts

Extracts samples	Total Antioxidant Status*
Ethanol	1,56
Water	1,45

*Total Antioxidant Status were calculated as mmol Trolox Equivalent./L.

Determination of Antimicrobial Activity of Extracts

In this study, it was used two different soluble solutions as ethanol and distilled water. The antimicrobial activity of leaves of *Morus alba* L. is presented in Table 2. The inhibition zones of our test microorganisms were measured as mm and were seen in different rate. The ethanol extracts of leaves were more effective than distilled water extracts. Distilled water extracts have no any inhibition zone. The maximum zone of inhibition was against *Pseudomonas aeroginosa* (13.5±0.5 mm), followed by *Escherichia coli* (9.7±0.9 mm) and *Enterococcus faecalis* (9.5±1.2 mm). The minimum zone of inhibition was obtained against *Candida albicans* and *Staphylococcus aureus*, (8.7±0.9 and 8.7±0.8 mm respectively). It was reported that methanol and chloroform extracts of different species of Morus exhibited antimicrobial activity against *Pseudomonas aeroginosa*, *Proteus vulgaris, Bacillus subtilis, Salmonella typhi, Shigella flexneri*, *Candida albicans* and *Aspergillus niger* [17]. In another study, leaves, stems and fruits of *Morus alba* L. were extracted with ethanol and water. The ethanol extracts exhibited stronger antimicrobial activities than the distilled water extracts. Among the ethanol extracts, leaves had most effective inhibition activity with the IC_{50} 7.11 ± 1.45 mg/mL value [16]. Our results supported the previous studies.

Table 2. Inhibition rate of herbal extracts from *Morus alba L.* leaves in our test microorganisms

Extracts samples	Strains				
	S.aureus	*E.faecalis*	*P.aeroginosa*	*E.coli*	*C.albicans*
Ethanol	8,7 ± 0.8	9,5 ± 1,2	13,5 ± 0,5	9,7 ± 0,9	8,7 ± 0,9
Water	ND	ND	ND	ND	ND

ND: Not determined

Values are mean of triplicate readings (mean ±S.D).

Gas Chromatography/Mass Spectrometry (GC/MS)

The extract cleavage products GC/MS spectrum was obtained according to the observed peaks (Figure 1). Structural formulas of the diagram are the appropriate degradation products are displayed on the peaks. The extract components were identified the aid of gas chromatography and decomposition products were characterized by mass analyser detector GC/MS. The mass spectrum shows that there were three components in extracts, 9,12,15-octadecatrienoic acid ethyl ester, linolenic acid ethyl ester and gibberallic acid respectively, and the giberellic acid is main one. According to Saravanan et al. [18], as a result of GC/MS analysis of *Ficus religiosa* L. which is same family member with *Morus alba* L. (Moraceae), 13 different compounds were determined. Some of the compounds

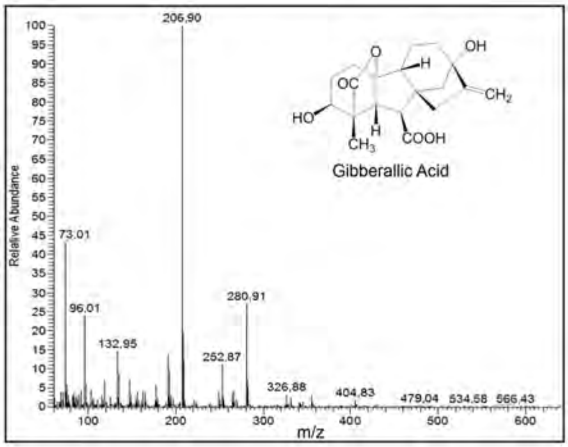

Figure 1. GC/MS spectra and fragmentation patterns of extract

that have antioxidant and antimicrobial activity were phenol, 4-methoxy phenol, ethyl isoallocholate and octadecanoic acid. In another study, GC/MS analysis showed the presence of 9,12,15-octadecatrienoic acid in *Vitis sitosa*. It was reported that this compound possesses many biological activities such as anti-inflammatory, hypocholesterolemic, cancer preventive, hepatoprotective, nematicide, antihistaminic, antieczemic, antiacne, antiandrogenic, antiarthritic, anticoronary, insectifuge properties and acts as an antimicrobial agent [19].

CONCLUSIONS

In this research we enlightened antioxidant and antimicrobial activities with GC/MS analysis of *Morus alba* L. leaves. Our study indicates promising results for the antioxidant and antimicrobial activity of ethanol extracts of *Morus alba* L. leaves. In present study, four different compounds were identified in the ethanol extracts of leaves by GC/MS analysis. Especially, giberellic acid contributed more percentage than other components. But other components such as 9,12,15-octadecatrienoic acid was reported for many biological activities. So, antioxidant and antimicrobial activity can be related to these molecules. Therefore, this research supports of using this plant's leaves for future development of novel antioxidant and antimicrobial agents.

It is also important to emphasize those further biological studies to determine the mechanism of antimicrobial action and to elucidate the other activities of components such as anti-inflammatory, anticancer must be conducted.

ACKNOWLEDGEMENTS

We are thankful to Department of Biology, Gazi University, Prof. Dr. Murat EKICI for identification plants samples.

REFERENCES

1. Salem MZM, Aly H, Gohar Y, El–Sayed AW. Biological activity of extracts from *Morus alba* L., *Albizzia lebbeck* L. Benth. and *Casuarina glauca* Sieber against the growth of some pathogenic bacteria. Journal of Agricultural and Food Chemistry 2 (2013) 9–22.
2. Chang LW, Juang LJ, Wanga BS, Wang MY, Tai HM, Hung WJ, Chen YJ, Huang MH. Antioxidant and antityrosinase activity of mulberry (*Morus alba* L.) twigs and root bark. Food and Chemical Toxicology 49 (2011) 785-790.
3. Zhishen J, Mengcheng T, Jianming W. The determination of flavonoid contents in mulberry and their scavenging effects in superoxide radicals. Food Chemistry 64 (1999) 555-559.
4. Harauma A, Murayama T, Ikeyama K, Sano H, Arai H, Takano R, Kita T, Hara S, Kamei K, Yokode M. Mulberry leaf powder prevents atherosclerosis in apolipoprotein E–deficient mice. Biochemical and Biophysical Research Communications 358 (2007) 751-756.
5. Dua J, Hea Z–D, Jianga RW, Yeb WC, Xua HX, But PPH. Antiviral flavonoids from the root bark of *Morus alba* L. Phytochemistry 62 (2003) 1235-1238.
6. Prakash D, Upadhyay G, Sing BN, Sing HB. Antioxidant and free radical scavenging activities of seeds and agri–wast of some varieties of soybean. Food Chemistry 104 (2007) 783.
7. Erel O. A novel automated direct measurement method for total antioxidant capacity using a new generation more sable ABTS radical cation. Clinical Biochemistry 37(4) (2004) 277–85.
8. Khan MA, Rahman AA, Islam S, Khandokhar P, Parvin S, Islam B, Hossain M, Rashid M, Sadik G, Nasrin S, Mollah MNH, Alam K. A comparative study on the antioxidant activity of methanolic extracts from different parts of *Morus alba* L. (Moraceae). BMC Research Notes (2013) 6–24.
9. Naowaboota J, Pannangpetcha P, Kukongviriyapana V, Kukongviriyapanb U, Nakmareongb S, Itharatc A. Mulberry leaf extract restores arterial pressure in streptozotocin–induced chronic diabetic rats. Nutrition Research 29 (2009) 602-608.
10. Oh J, Jo H, Cho AR, Kim SJ, Han J. Antioxidant and antimicrobial activities of various leafy herbal teas. Food Control 31 (2013) 403–409.
11. Exarchou V, Nenadis N, Tsimidou M. Antioxidant activities and phenolics composition of extracts from Greek oregano, Greek sage and Summer savory. Journal of Agricultural and Food Chemistry 50 (19) (2002) 5294–5299.
12. Salvamani S, Gunasekaran B, Shaharuddin NA, Ahmad SA, Shukor MY. Antiartherosclerotic effects of plant flavonoids. BioMed Research International 2014 (2014) 1–11.

13. Sohn HY, Son KH, Kwon CS, Kwon GS, Kang SS. Antimicrobial and cytotoxic activity of 18 prenylated flavonoids isolated from medicinal plants: *Morus alba* L., *Morus mongolica Schneider*, *Broussnetia papyrifera* (L.) Vent, Sophora flavescens Ait and Echinosophora koreensis Nakai. Phytomedicine 11 (2004) 666-672.
14. Muthumani GD, Vijay Anan A, Manikandan A. Antioxidant, antihelmintic and antimicrobial activity of *Euphorbia thymifolia* Linn whole plant. International Journal of Current Microbiology and Applied Sciences 2 (2013) 66.
15. Kahkonen MP, Hopia AI, Vuorela HJ, Rauh JP, Pihlaja K, Kujala TS, Heinonen M. Antioxidant activity of plant extracts containing phenolic compounds. Journal of Agricultural and Food Chemistry 47 (1999) 3954–3962.
16. Wang W, Zu Y, Fu Y, Efferth T. In vitro antioxidant and antimicrobial activity of extracts from Morus alba L. leaves, stems and fruits. The American Journal of Chinese Medicine 40(2) (2012) 349–356.
17. Aditya Rao SJ, Ramesh CK, Riaz M, Prabhakar BT. Anthelmintic and antimicrobial activities in some species of mulberry. International Journal of Pharmacy and Pharmaceutical Sciences 4 (2012) 335–338.
18. Saravanan P, Chandramohan G, Mariajancyrani J, Shanmugasundaram P. GC–MS analysis of phytochemical constituents in ethanolic bark extract of *Ficus religiosa* LINN. Int. J. Pharm. Sci. 6 (2014) 457–460.
19. Gobalakrishnan R, Manikandan P, Bhuvaneswari R. Antimicrobial potential and bioactive constituents from aerial parts of *Vitis setosa* Wall. Journal of Medicinal Plants Research 8(11) (2014) 454–460.

Hittite Journal of Science and Engineering, 2014, (1) 1 43-50
ISSN NUMBER: 2149-2123
doi: 10.17350/HJSE19030000007

Separation and Purification of Lipase Using Cu Nanoparticle Embedded Poly(HEMA-MATrp) Cryogels

Kadir Erol[1], Kazım Kose[2,*], Dursun Ali Kose[1], Gulcin Alp Avcı[3] and Lokman Uzun[4]
[1]Hitit University, Department of Chemistry, Corum, TURKEY
[2]Hitit University, Scientific Technical Research and Application Center, Corum, TURKEY
[3]Hitit University, Department of Molecular Biology and Genetics, Corum, TURKEY
[4]Hacettepe University, Department of Chemistry, Ankara, TURKEY

Article History:
Received: 2014/11/26
Accepted: 2014/12/15
Online: 2014/12/31

***Correspondence to**: Kazim Kose,*
Hitit University Scientific Technical Research and Application Centre, Corum, Turkey.
Tel: +90 (364) 227-7000 (2866)
Fax: +90 (364) 227-7005
E-Mail: kazim8080@gmail.com

ABSTRACT

Quality and efficiency of techniques to be used for separation and purification lipase enzymes are commercially important enzyme. Among such techniques, adsorption methods are highly preferred. Cryogels have been quite extensively used as the adsorbents due to their macropores and interconnected flow channels. In this study, adsorption of lipase enzyme onto copper nanoparticles embedded poly(2-hydroxyethyl methacrylate-N-methacryloyl-L-tryptophan), poly(HEMA-MATrp) cryogels was studies for conditions with varying pH, interaction time, lipase enzyme initial concentration, temperature and ionic strength. Maximum lipase enzyme adsorption capacity of cryogels was determined as 183.6 mg/g. Fourier transform infrared spectrometer (FTIR) and scanning electron microscopy (SEM) were used for characterization of cryogels. At the end of the adsorption process, in order to be sure that the purity of lipase enzyme desorbed from cryogels, SDS-PAGE analyses were performed and molecular weight of the lipase enzyme was determined as 58 kDa. Adsorption characteristic of cryogels were determined according to the results of Langmuir and Freundlich adsorption isotherm models. As a result of calculation run for adsorption isotherm models, Langmuir isotherm model was determined to be more appropriate.

Key Words:
Lipase; Cupper; Cryogel; Adsorption.

INTRODUCTION

Lipase (EC 3.1.1.3) is a commercially important enzyme and play an important role in bio catalytic transformation reactions [1-5]. Lipase enzymes digest triacylglycerol into glycerol, free fatty acid, monoacylglycerol and diacylglycerol [6-7]. These enzymes are also able to catalyze esterification, interesterification, transesterification, aminolysis, thiotransesterification and oximolysis reactions [6-8]. Lipase enzyme has been utilized several fields such as production and degradation of biopolymer, pharmaceutical, agrochemical, biolubricants, cosmetic, flavours and fragrances, oil-rich water treatment and esterification via short chain alcohols and biodiesel production using transesterification reactions [11-17].

In recent years, for separation and purification of enzymes, adsorption technique has been preferred. Synthetic and natural adsorbents have been used for adsorption experiments. Cryogels have a great place among synthetic adsorbents due to their advantages such as easy preparation, being cost-friendly, having large pores, and interconnected flow channels. These polymeric structures formed as a result of freezing of solvent initially and de-freezing again at room temperature have hydrophilic character. High porosity of these structures provide them almost sponge-like structure. Reusability feature of these structures is also quite efficient. Due to these features and their elastic properties provide a great advantage for cryogel structures [18-25].

Cu nanoparticles were embedded into poly(2-hydroxyethyl methacrylate-N-methacryloyl-L-tryptophan) cryogel structure synthesized in this study and adsorption of lipase enzyme from aqueous solution was examined using this synthetic material. Cu nanoparticles are considered to increase the electrostatic character of interactions emerge during adsorption reaction. Therefore, a positive contribution of this effect is expected for the adsorption capacity as increasing. The method used in this study is considered to be an efficient alternative for techniques in the literature used for separation and purification of lipase enzyme.

MATERIALS AND METHODS

Lipase (from *Candida cylindracea*), 2-hydroxyethyl methacrylate (HEMA), ethylene glycol dimethacrylate (EGDMA), L-tryptophan, methacryloyl chloride, sodium nitrite ($NaNO_2$), potassium carbonate (K_2CO_3) and ethyl acetate were purchased from Aldrich (St. Louis, MO, USA). N, N, N', N'- tetramethyl ethylene diamine and ammonium persulphate compounds were obtained from Sigma (Munich, Germany). Ascorbic acid was from Fluka (St. Gallen, Switzerland). Diethyl ether, cyclohexane, and copper (II) sulphate penta hydrate ($CuSO_4.5H_2O$) compounds were purchased from Sigma-Aldrich (St. Louis, MO, USA). UV-VIS Double Beam PCR 8 Scanning Auto Cell UVD-3200 (Labomed, INC.) (USA) device was used for spectrometric determinations at UV-VIS region. N-methacryloyl-L-tryptophan compound was synthesized in laboratory in accordance with literature [26]. All other chemicals were of analytical grade.

MATrp Synthesis

As a first step, L-tryptophan of 5 g and $NaNO_2$ of 0.2 g compounds were dissolved in an aqueous solution of K_2CO_3 of 30 mL 5% (w/v) and just then the solution was cooled to 0°C. After that step, 4 mL of methacryloyl chloride was added drop wise in nitrogen gas (N_2) environment. The solution obtained was stirred for 2 hours at room temperature using magnetic stirrer and then the pH of solution was adjusted to 7. The solution was subjected to extraction process using ethyl acetate. The liquid phase was removed via evaporator and MATrp was obtained by crystallization with diethyl ether and cyclohexane [26].

Poly(HEMA-MATrp) Cryogel Synthesis

2-Hydroxyethyl methacrylate (HEMA, 2.5 mL) as a structural monomer and N-methacryloyl-L-tryptophan (MATrp, 50 mg) as a functional monomer were dissolved in 2.5 mL distilled water. The mixture of 0.5 g sodium lauryl sulphate (SLS), 0.6 mL ethylene glycol dimethacrylate (EGDMA) and 9.4 mL distilled water was added to the solution obtained previously. Last mixture was stirred with a magnetic stirrer until obtaining a homogeneity and was remained in an ice bath for approximately 15 minutes. In the final stage, ammonium persulphate (APS) of 10 mg and N, N, N', N'- tetramethyl ethlyenediamine (TEMED) of 50 μL were added and were remained at -12°C for 24 hours. Cryogels synthesized was gone disk-shape cut (membrane) and washed with distilled water several times until all unwanted particles were removed.

Cu Nanoparticle Synthesis

$CuSO_4.5H_2O$ of 0.001 mole and ascorbic acid of 0.011 mole were dissolved in 100 mL distilled water. pH of the solution was adjusted to about 6.5 using NaOH solution and the solution was stirred in a flask with a magnetic stirrer at 1000 rpm at 85°C for 1 hour [27]. Towards the end of the process, color of solution was turned from orange to brown. The solution obtained was centrifuged at 12000 rpm for 30 minutes. Copper nanoparticles precipitated was dried on watch-glass in an oven. Chemical reduction reactions occurring in this process were as follows:

$Cu^{2+} + 2OH^- \rightarrow Cu(OH)_2$

$Cu(OH)_2 + C_6H_8O_6 \rightarrow Cu(k) + C_6H_6O_6 + 2H_2O$ [28]

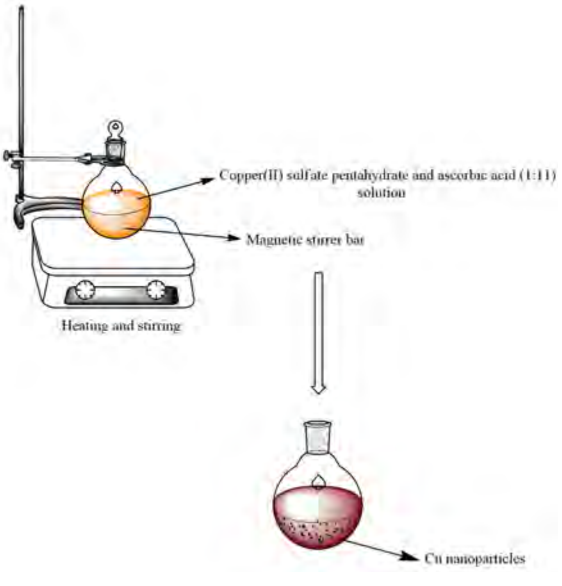

Figure 1. Schematic diagram for Cu nanoparticle synthesis.

Embedding of Cu Nanoparticles into Structure of poly(HEMA-MATrp) Cryogels

For this operation, Cu nanoparticles were incorporated into cryogel structure with the concentration of 100 mg/L in distilled water of 25 mL and this solution was stirred with magnetic stirrer continuously for 2 hours. As a result of these processes, colour of the solution was turned from white to light yellow and to get rid of unwanted particles cryogels were washed several times with distilled water (Figure 2).

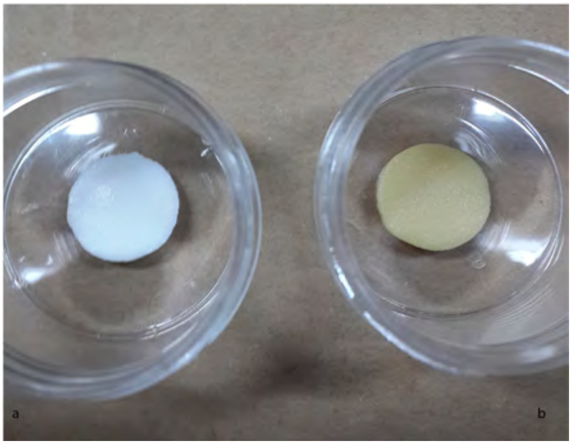

Figure 2. Photos of cryogels a) before and b) after embedding of Cu nanoparticles into the structure.

Characterization of poly(HEMA-MATrp) Cryogels

Swelling Test

Firstly, a cryogel sample was dried by lyophilisation and then was carefully weighed. To understand the swelling ratio dry sample was placed in a baker of distilled water within the isothermal water bath at 25°C for 30 minutes to obtain fully swelled cryogel membrane. At the end of this process the swelled cryogel sample was re-weighed carefully and water retention capacity of the membrane was determined by the following equation:

Water retention capacity% = $[(W_s - W_o) / W_o] \times 100$ (1)

In this equation, W_o and W_s stand for weights (g) of dry and swelled cryogels.

Surface Morphology

To determine the surface morphology of cryogels, scanning electron microscopy (SEM) (Carl Zeiss AG - EVO® 50 Series, Germany) was used. For this operation, as a first step, cryogel samples were dried and lyophilized for SEM analysis. Then a sufficient amount of sample was placed on SEM holder and analysed after coated with a thin gold layer at vacuum and at the end images were taken.

FTIR Analysis

For this operation, Fourier transform infrared spectroscopy (Thermo Scientific, Nicholet IS10, USA) was used. Pellets had been prepared primarily for analysis. To prepare pellets, dry cryogel sample of 2 mg and dry KBr powder of 98 mg were used and then FTIR analysis was performed.

Adsorption Studies

Adsorption studies were carried out via batch system. Adsorption medium was prepared with the use of lipase solution of 1 mL and buffer solution of 4 mL. Before adding cryogel membranes lipase and buffer solution was stirred at magnetic stirrer for 15 min. and equilibrated.

To calculate the adsorption capacity following equations is utilized.

$$q = [(C_i - C_f) \times V] / m \quad (2)$$

wherein, q is adsorption capacity (mg/g), C_i is the concentration of lipase enzyme before adsorption (mg/L), C_f is the concentration of lipase enzyme after completion of adsorption (mg/L), V is the volume of the adsorption medium (L), and m is the mass of cryogel (g).

Desorption and Reusability

Batch experiments were preferred for desorption of lipase adsorbed on cryogels. For this operation, lipase adsorbed cryogels were stirred continuously with magnetic stirrer for 1 hour in desorption medium having HCl solution (0.1 M, 10 mL) for 1 hour. To examine the reusability of cryogels, adsorption-desorption cycle was repeated 5 times with the same cryogel membrane. Cryogel used was washed with NaOH solution (0.1 M) of 10 mL for 30 minutes and to equilibrate this solution pH:6.0 buffer solution of 10 mL was used to treat cryogels 30 minutes. Desorption rate was calculated by the following equation.

Desorption rate (%) = (Amount of Enzyme Desorbed / Total Amount of Enzyme)x100 (3)

RESULTS AND DISCUSSION

Characterization of poly(HEMA-MATrp)

Swelling Test

Swelling test was performed the method mentioned before. Weight of dry and water swelled cryogel membranes was determined as 29.6 and 164.3 mg/disc, respectively. According to these results, water retention capacity of cryogels was calculated as in Equation 2.1 and found as 455%.

Surface Morphology

To determine surface morphology of cryogels, SEM images of membranes were taken (Figure 3). As the figure shows, a macroporous structure containing interconnected flow channels was obtained.

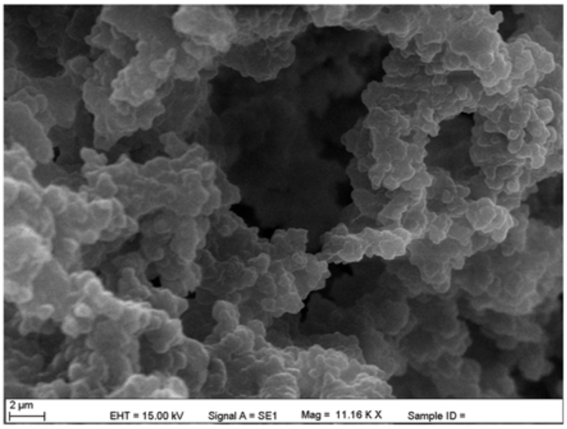

Figure 3. SEM image of poly(HEMA-MATrp) cryogels.

FTIR Analysis

Molecular structure and FTIR spectrum of poly(HEMA-MATrp) cryogels are shown by Figure 4 – 5, respectively. From spectrum, 3424 cm^{-1} (OH stretching), 2941 cm^{-1} (CH stretching for aliphatic alkyl), 1710 cm^{-1} (C=O stretching), 1649 cm^{-1} (C=C stretching), 1446 and 1381 cm^{-1} (C-N stretching for amide) and 1147 cm^{-1} (aromatic ring bending) bands are quite noteworthy. Existence of some of functional groups corresponding these bands (C=C stretching, C-N stretching for amide, aromatic ring bending) within MATrp structure denotes that MATrp monomer was successfully incorporated into HEMA structure.

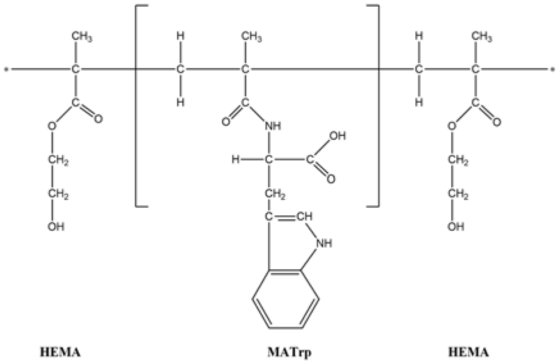

Figure 4. Molecular structure of poly(HEMA-MATrp) cryogels.

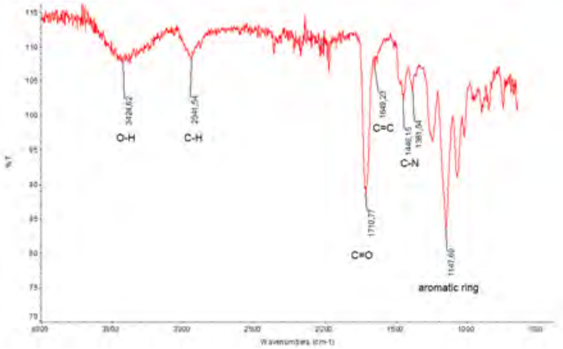

Figure 5. FTIR spectrum of poly(HEMA-MATrp) cryogels.

Adsorption Studies

Effect of pH

To determine the effect of pH on the lipase adsorption capacity of cryogels, pH of solutions used for adsorption studies was changed in the pH range of 3.0-10.0. According to the consideration of results, adsorption capacity of cryogels was maximum at pH: 6.0. It is concluded that lipase molecules are interacted with Cu nanoparticles bound indol ring at the functional monomer (MATrp) via electrostatic interactions. These interactions are directly related with charge distribution of polar groups (aspartate, lysine, arginine, etc.) on lipase enzymes, and these interactions are most stable at pH: 6.0 and suitable for electrostatic interactions. Therefore, it is determined that interactions at pH: 6.0 are the most effective so this pH is set at optimum pH value.

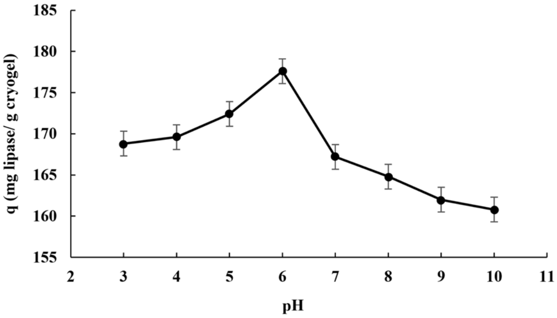

Figure 6. Effect of pH on the adsorption of lipase enzyme onto Cu nanoparticles embedded cryogels. C_{lipase}: 1.5 mg/mL, Interaction time: 30 min., T: 25°C.

Effect of Interaction Time

To investigate the effect of interaction time on the adsorption of lipase onto cryogels, adsorption experiments were performed at the time range of 5-75 minutes. At the end of the experiments, it was determined that equilibrium adsorption capacity was

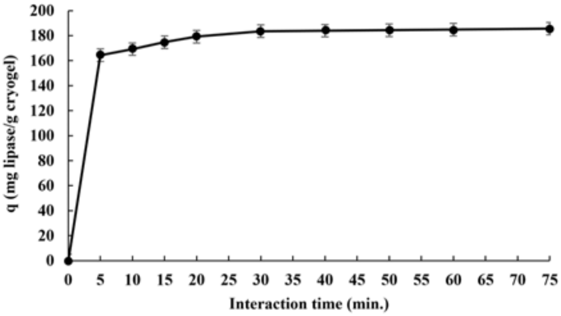

Figure 7. Effect of interaction time on the adsorption of lipase enzyme onto Cu nanoparticles embedded cryogels. C_{lipase}: 1.5 mg/mL, pH: 6.0, T: 25°C.

achieved at 30th minute (Figure 7). Porous structure and interconnected flow channels of Cu embedded cryogels synthesized enable interaction to be occurred rapidly. Therefore, optimal interaction time was determined as 30 min. and all remaining studies were performed with respect to this time period.

Effect of Initial Concentration of Lipase Enzyme

To determine the effect of initial concentration on the lipase adsorption capacity of Cu embedded cryogels, adsorption studies were performed for the amount of lipase concentration of 0.5-3 mg/mL. As a result of the experiments, it was observed that adsorption capacity of cryogels was increased with increased initial concentration lipase enzyme for the beginning of adsorption process, but a bit after there was a steady state on the adsorption (Figure 8). The reason for this might be that lipase binding sites of cryogels had been reached the saturation after certain concentration.

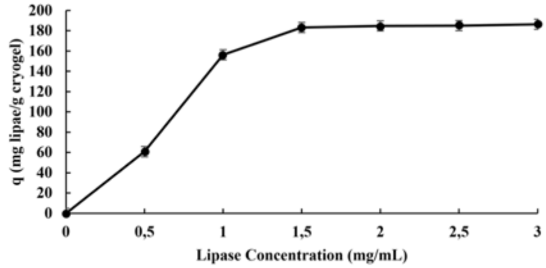

Figure 8. Effect of initial concentration on the adsorption of lipase enzyme onto Cu nanoparticles embedded cryogels. pH: 6.0, interaction time: 30 min., T: 25°C.

Effect of Temperature

In order to determine the effect of temperature on the adsorption of lipase, adsorption experiments were conducted at four different temperatures (7, 20, 30 and 40°C). As a result of experiments conducted, adsorption capacities of cryogels were decreased with increasing temperature as expected (Figure 9). The reason for this is that coordinated covalent bonds, interactions occurring via shared electron are weakened and reduced as a result of severances [29].

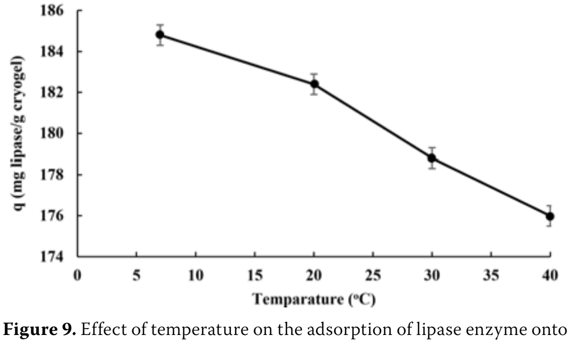

Figure 9. Effect of temperature on the adsorption of lipase enzyme onto Cu nanoparticles embedded cryogels. pH: 6.0 interaction time: 30 min., C_{lipase}: 1.5 mg/mL.

Effect of Ionic Strength

In this study, NaCl solutions with concentration range of 0.5-4.0 M were used to determine the effect of ionic strength on the adsorption of lipase enzyme. Considering Figure 10, the adsorption capacity was decreased with increasing salt concentration. This is because of presence of ions (Na^+ and Cl^-) coming from NaCI molecules in the medium and thus these ions effect the charge distribution of groups such as aspartate, lysine, arginine on the surface of lipase enzyme. Na^+ and Cl^- ions are interacted with these groups electrostatically, and so limit by masking the interaction having potential to occur between Cu nanoparticles and lipase enzyme. Therefore, the adsorption capacity decreases with increasing ionic strength.

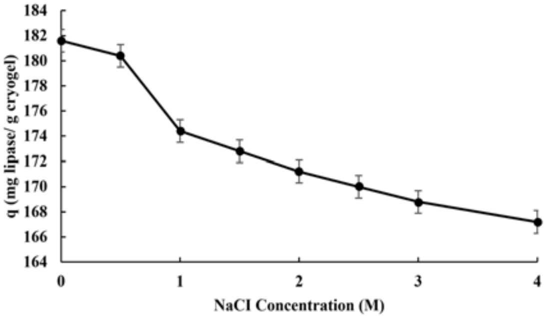

Figure 10. Effect of ionic strength on the adsorption of lipase enzyme onto Cu nanoparticles embedded cryogels. H: 6.0, interaction time: 30 min., C_{lipase}: 1.5 mg/mL, T: 25°C.

Desorption and Reusability

In order to determine the reusability feature of cryogels, adsorption - desorption cycle was repeated 5 times using same cryogels. As a result of this study, desorption ratio of cryogels was determined as 78% and there was no significant decrease observed in the adsorption capacity (from 172.8 mg / g to 164.8 mg / g) (Figure 11). Considering these results, it is concluded that Cu nanoparticle embedded cryogels are interacted specifically and reversibly with lipase enzyme, and can be said to have high reusability ratio.

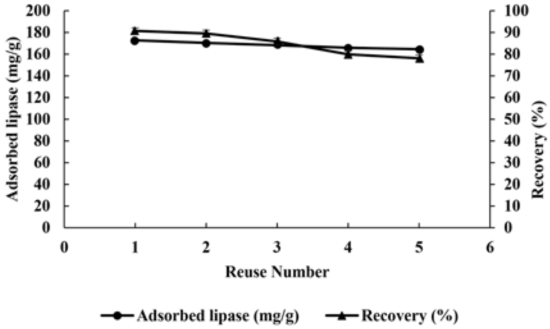

Figure 11. Reusability of Cu nanoparticle embedded poly(HEMA-MATrp) cryogels. pH: 6.0, interaction time: 30 min., C_{lipase}: 1.5 mg/L, T: 25°C.

SDS-PAGE Analysis

SDS-PAGE analysis of lipase purified using Cu nanoparticle embedded poly(HEMA-MATrp) cryogels is shown at Figure 12. Because the distance of lipase desorbed from cryogels synthesized in this study covered on poly acrylamide SDS gel is exactly same with the distance covered by lipase marker (58 kDa), it can be concluded that purity of lipase desorbed from cryogels is quite acceptable and adsorption - desorption performance achieved successfully using Cu nanoparticle embedded poly(HEMA-MATrp) cryogels.

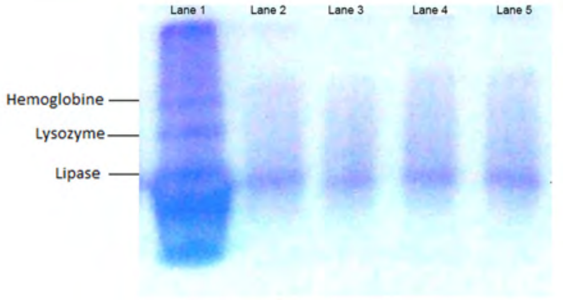

Figure 12. SDS-PAGE image for lipase enzyme desorbed from *Candida cylindracea*. Lane 1: Marker (Lipase, Lysozyme, Hemoglobine) Lane 2: Lipase marker, Lane 3: Initial lipase solution [(Before adsorption for Cu nanoparticle embedded poly(HEMA-MATrp) cryogels], Lane 4: Final lipase solution [(After adsorption for Cu nanoparticle embedded poly(HEMA-MATrp) cryogels], Lane 5: Desorbed sample [(After desorption from Cu nanoparticle embedded poly(HEMA-MATrp) cryogels.

Adsorption Isotherms

Adsorption isotherms were investigated to characterize the lipase adsorption process performed using Cu nanoparticle embedded poly (HEMA-MATrp) cryogels. According to the Langmuir adsorption model, adsorption is considered as a monolayer (homogeneous) on the surface [30]. However, Freundlich adsorption isotherm model provides multi-layer adsorption layer so thus heterogeneous [31]. For Langmuir and Freundlich adsorption isotherms, following equations are used:

$1/Q_{eq} = [1/(Q_{max.}\ b)][1/C_{eq}] + [1/(Q_{max})]$ Langmuir equation (4)

In this equation, $1/Q_{max}$ and $1/Q_{max}.b$ can be calculated from using y - intercept point and slope obtained from the graph of $1/C_{eq}$ versus $1/Q_{eq}$, respectively (Figure 13). In this equation, Q_{eq} is the adsorption capacity (mg/g), C_{eq} is the lipase concentration at equilibrium, b is the Langmuir adsorption constant (L/mg), and Q_{max} is the maximum adsorption capacity (mg/g).

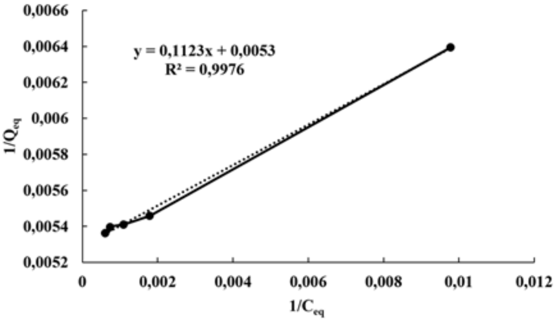

Figure 13. Langmuir adsorption isotherm plotted from experimental values.

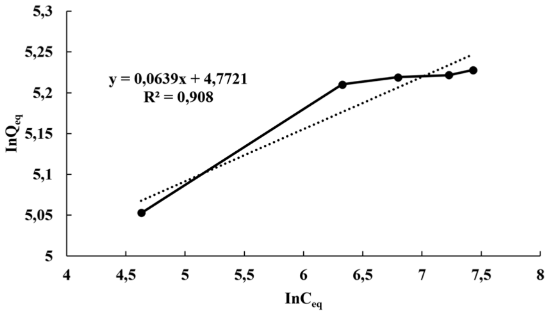

Figure 14. Freundlich adsorption isotherm plotted from experimental values.

$\ln Q_{eq} = \ln K_f + (n \times \ln C_{eq})$ Freundlich equation (5)

In this equation, K_F and n represent Freundlich adsorption isotherm constants. $\ln K_F$ and n can be calculated using y - intercept point and slope from the graph $\ln Q_{eq}$ versus $\ln C_{eq}$, respectively (Figure 14).

Regression coefficient obtained from the graph plotted for Langmuir isotherm model (0.9976) is higher than that (0.9080) from the graph plotted for Freundlich isotherm model (Table 1). Therefore, it can be concluded that Langmuir adsorption isotherm model is more suitable for the adsorption reaction of lipase onto Cu nanoparticles embedded poly(HEMA-MATrp) cryogels. In other words, adsorption reaction was achieved on the surface as mono-layer (homogeneous).

Table.1. Parameters estimated from Langmuir and Freundlich adsorption isotherms.

Langmuir Constants				Freundlich Constants			
Q_{epx}(mg/g)	Q_{max}(mg/g)	b (L/mg)	R^2	K_f	n	1/n	R^2
183.6	188.68	0.047	0.9976	118.17	0.0639	15.65	0.9080

CONCLUSIONS

In this study, adsorption of lipase enzyme onto Cu embedded poly (HEMA-MATrp) cryogels was ensured by electrostatic interactions. Moreover, decreasing adsorption capacity with increasing temperature and ionic strength confirm the presence of this kind of interaction in this study. Because interactions such as coordinate covalent bond, occur via shared electrons, ionic interactions are inversely proportional with temperature and ionic strength. In conclusion, it is determined that the Langmuir adsorption model is more appropriate model for adsorption for this study. In other words, adsorption was achieved on the surface as mono-layer but not as multi-layer.

REFERENCES

1. Morcillo F, Cros D, Billotte N, Ngando–Ebongue G. Domonhédo H, Pizot M. Improving palm oil quality through identification and mapping of the lipase gene causing oil deterioration. Nature Communications 4 (2013) 2160-2164.
2. Das S, Eder S, Schauer S, Diwoky C, Temmel H, Guertl B. Adipose triglyceride lipase contributes to cancer–associated cachexia. Science 333 (2011) 233-238.
3. DiCosimo R, McAuliffe J, Poulose A, Bohlmann G. Industrial use of immobilized enzymes. Chemical Society Reviews 42 (2013) 6437-6474.
4. Hasan F, Shah AA, Hameed A. Industrial applications of microbial lipases. Enzyme and Microbial Technology 39 (2006) 235-251.
5. Houde A, Kademi A, Leblanc D. Lipases and their industrial applications. Applied Biochemistry and Biotechnology 118 (2004) 155-170.
6. Sarda L, Desnuelle P. Action de la lipase pancreatique sur lês esteres enemulsion. Biochimica et Biophysica Acta 30 (1958) 513-521.
7. Reis P, Holmberg K, Watzke H, Leser ME, Miller R. Lipases at interfaces: a Review. Advances in Colloid and Interface Science 147-148 (2009) 237-250.
8. Zaks A, Klibanov AM. Enzyme–catalysed processes in organic solvents. Proceedings of the National Academy of Sciences 82 (1985) 3192-3196.
9. Adlercreutz P. Immobilisation and application of lipases in organic media. Chemical Society Reviews 42 (2013) 6406-6436.
10. Kapoor M, Gupta MN. Lipase promiscuity and its biochemical applications. Process Biochemistry 47 (2012) 555-569.
11. Mendes AA, Oliveira PC, Castro HF, Properties and biotechnological applications of porcine pancreatic lipase. Journal of Molecular Catalysis B: Enzymatic 78 (2012) 119-134.
12. Fernandez–Lafuente R. Lipase from Thermomyces lanuginosus: uses and prospects as an industrial biocatalyst. Journal of Molecular Catalysis B: Enzymatic 62 (2010) 197-212.
13. Sharma D, Sharma B, Shukla AK. Biotechnological approach of microbial lipase: a review. Biotechnology 10 (2011) 23-40.
14. Hasan F, Shah AA, Hameed A. Industrial applications of microbial lipases. Enzyme and Microbial Technology 39 (2006) 235-251.
15. Chesterfield DM, Rogers PL, Al–Zaini EO, Adesina AA, Production of biodiesel via ethanolysis of waste cooking oil using immobilised lipase. Chemical Engineering Journal 207-208 (2012) 701-710.
16. Olivares–Carrillo P, Quesada–Medina J, de los Ríos AP, Hernández–Fernández FJ, Estimation of critical properties of reaction mixtures obtained in different reaction conditions during the synthesis of biodiesel with supercritical methanol from soybean oil. Chemical Engineering Journal 241 (2014) 418-432.
17. Umare SS, Chandure AS. Synthesis, characterization and biodegradation studies of poly(ester urethane)s. Chemical Engineering Journal 142 (2008) 65-77.
18. Wang C, Dong XY, Jiang Z, Sun Y. Enhanced adsorption capacity of cryogel bed by incorporating polymeric resin particles. Journal of Chromatography A 1272 (2013) 20–25.
19. Zhao W, Zhang S, Lu M, Shen S, Yun J, Yao K, et al. Immiscible liquid slug flow characteristics in the generation of aqueous drops within a rectangular microchannel for preparation of poly(2–hydroxyethylmethacrylate) cryogel beads. Chemical Engineering Research and Design 2014. http://dx.doi.org/10.1016/j.Cherd.2014.01.012 [*in press*].
20. Uzun L, Armutcu C, Biçen O, Ersöz A, Say R, Denizli A. Simultaneous depletion of immunoglobulin G and albumin from human plasma using novel monolithic cryogel columns. Colloids and Surfaces B: Biointerfaces 112 (2013) 1–8.
21. Yuna J, Jespersen GR, Kirsebom H, Gustavsson PE, Mattiasson B, Galaeva IY. An improved capillary model for describing the microstructure characteristics, fluid hydrodynamics and breakthrough performance of proteins in cryogel beds. Journal of Chromatography A 1218 (2011) 5487–5497.
22. Eichhorn T, Ivanov AE, Dainiak MB, Leistner A, Linsberger I, Jungvid H, et al. Macroporous composite cryogels with embedded polystyrene divinylbenzene microparticles for the adsorption of toxic metabolites from blood. Journal of Chemistry ttp://dx.doi.org/10.1155/2013/348412.
23. Hajizadeh S, Xu C, Kirsebom H, Ye L, Mattiasson B. Cryogelation of molecularly imprinted nanoparticles: a macroporous structure as affinity chromatography column for removal of b–blockers from complex samples. Journal of Chromatography A 1274 (2013) 6–12.
24. Plieva FM, Kirsebom H, Mattiasson B. Preparation of macroporous cryostructurated gel monoliths, their characterization and main applications. Separation Scientific 34 (2011) 2164–2172.
25. Plieva FM, Galaev IY, Noppe W, Mattiasson B. Cryogel applications in microbiology. Trends in Microbiology 16 (2008) 543–551.
26. Yilmaz F, Bereli N, Yavuz H, Denizli A. Supermacroporous hydrophobic affinity cryogels for protein chromatography. Biochemical Engineering Journal 43 (2009) 272-279.
27. Zhang W, Luan C, Yang Z, Liu X, Zhang D, Yang S. Preparation and optical properties of Cu 2O hollow microsphere film and hollow nanosphere powder via a simple liquid reduction approach. Applied Surface Science 253 (2007) 6063–6067.

28. Qing–Ming L, Yasunami T, Kuruda K, Okido M. Preparation of Cu nanoparticles with ascorbic acid by aqueous solution reduction method. Transactions of Nonferrous Metals Society of China 22 (2012) 2198–2203.
29. Asliyuce S, Uzun L, Say R, Denizli A. Immunoglobulin G recognition with Fab fragments imprinted monolithic cryogels: Evaluation of the effects of metal–ion assisted–coordination of template molecule. Reactive and Functional Polymers. 73 (2013) 813–820.
30. Langmuir I. The adsorption of gas on plane surfaces of glass, mica and platinum. Journal of the American Chemical Society 40 (1918) 1361-1370.
31. Freundlich HMF, Uber die adsorption in losungen. Zeitschrift für. Physikalische Chemie. 57(1906) 385-471.

Hittite Journal of Science and Engineering, 2014, (I) 1 51-57
ISSN NUMBER: 2149-2123
DOI: 10.17350/HJSE19030000008

Mixed Ligand Complexes of Acesulfame/Nicotinamide with Earth Alkaline Metal Cations Mg^{II}, Ca^{II}, Ba^{II} and Sr^{II}. Synthesis and Characterization

Omer Yurdakul and Dursun Ali Kose
Hitit University, Department of Chemistry, Corum, Turkey

ABSTRACT

In the scope of this study, acesulfame (ace, acs)-nicotinamide (na) mixed ligand complexes of Mg(II), Ca(II), Sr(II) and Ba(II) were synthesized for the first time. Possible formulas for complexes were determined as $[Mg(H_2O)_4(na)_2](acs)_2$, $[Ca(H_2O)_6(na)_2](acs)_2$, $[Sr(H_2O)_7(na)_2](acs)_2$, $[Ba(H_2O)_7(na)_2](acs)_2$). It was observed that acesulfame ligands within structure were located two moles each at outer surface of coordination sphere acting as counter-ion allowing the charge balance of structure. The solubility of compounds gaining ionic character in this way was determined as quite well as compared to complex structures. Characterizations of complexes synthesized were performed via melting point analysis, elemental analysis, mass spectroscopy and FT-IR spectroscopy methods. Thermal properties of complexes obtained were determined with tandem TG-DTG and DTA techniques. It was found that the coordination spheres of metal cations within compounds obtained in this study were filled with nicotinamide and aqua ligands.

Article History:
Received: 2014/11/23
Accepted: 2012/12/30
Online: 2014/12/31

Correspondence to: *Dursun Ali Kose, Hitit University, Faculty of Arts and Science, Department of Chemistry, Corum, Turkey*
Tel: +90 (364) 227 7000
Fax: +90 (364) 227 7005
E-Mail: dalikose@hitit.edu.tr

Key words:
Acesulfame; Nicotinamide; Earth Alkaline Metals; Coordination Compound; Thermal Properties.

INTRODUCTION

The compound (Figure 1) with the trade name of acesulfame ($C_4H_4KNO_4S$, 201.242 g / mol), and with the nomenclature such as 6-methyl-1,2,3-oksotiaz-4 (3H) -on-2,2-dioxide, 6-methyl-2,2-dioksooksotiaz-4-on (IUPAC) is oxatiazinon dioxide. Moreover, it is also known as 6-methyl-3,4-dihydro-1,2,3-oksotiaz-4-on 2,2-dioxide, 1,2,3-oksotiazin-4(3H)-on-6-methyl-2,2-dioxide [1]. There are nitrogen and oxygen (in the ring); sulphonyl, methyl and carbonyl groups within the acesulfame structure. Because hydrogen atom bounded to nitrogen is quite acidic (pKa: ~ 2), it easily forms potassium salt. Today, use of acesulfame as a sweetener in beverages and food products is permitted. Potassium acesulfame is not metabolized in the body and does not produce energy. Acesulfame solution of 3% is 200 times sweeter than table sugar (sucrose) [2].

Nicotinamide is the compound with the chemical formula of $C_6H_6N_2O$ (Figure 1), molecular weight of 122.12 g/mol and the IUPAC name of 3-pyridine carboxamide. Basically, being an amide derivative of nicotinic acid, nicotinamide is also called as niacinamide, niacin, nicotinic acid amide, Vitamin PP and Vitamin B3. Nicotinamide with a peculiar smell and taste is a colourless crystalline substance. Because nicotinamide has pyridine ring, it gives characteristic pyridine reactions [3-7].

First metal complexes of acesulfame have been reported at 2005 [8,9]. Bis (acesulfamato-κ^2N^3,O^4) bis (2-aminopyirimidine-κN^1) copper (II) acesulfame is the

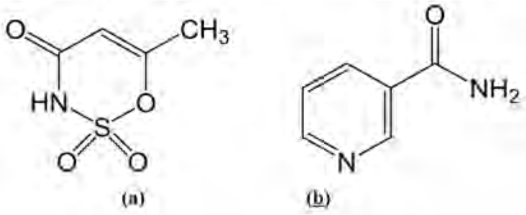

Figure 1. a) Acesulfame, **b)** Nicotinamide

first mixed ligand complex in the literature. The structure analysis of the complex was performed using X-Ray method and it was determined that acesulfame ligands are located at trans position and behave as bidentate ligand through nitrogen of imine and oxygen of carbonyl. It was also observed that 2-aminopyrimidine, secondary ligand, in the complex is almost planar.

It was detected that the molecular geometry of the complex is distorted octahedral due to Jahn-Teller effect and the effect of four membered chelate ring. The other conclusion obtained from experimental data is the hydrogen bonding between carbonyl oxygen of acesulfamato and 2-aminopirimidine ligand. Bis(acesulfamato-κ^2N^3, O^4) bis(2-aminopyrimidine-κN^1) copper (II) complex having four membered chelating ligand has the octahedral geometry [8]. The ring nitrogen of the acesulfamate ligand is more extended and in the axial position. Acesulfamate ligand within the structure at trans position acts as bidentate ligand via binding to Cu(II) ion through nitrogen of the ring and carbonyl oxygen. Octahedral geometry was achieved by the two neutral 2-aminopyrimidine ligand behaving as monodentate ligand. $[Ni(dmen)_2(H_2O)_2](acs)_2$ complex was the first complex within which acesulfamate anion acts as charge balancer [10]. At a comprehensive study performed for acesulfame metal complexes, details about synthesis, structure and properties of complexes with the general formula of $[M(acs)_2(H_2O)_4]$(M:Mn^{2+}, Co^{2+}, Ni^{2+} and Cu^{2+}, $[M(acs)_2(H_2O)_2]$(M: Zn^{2+} and Cd^{2+}) were investigated [11]. Crystalline structure of $[Co(acs)_2(H_2O)_4]$, one of the complexes synthesized, was investigated and it was determined that acesulfamato ligand is coordinated to Co(II) ion at trans position through imine nitrogen. For $[Co(acs)_2(H_2O)_4]$ complex, it was observed that there is intermolecular interaction (hydrogen bonding) between sulphonyl oxygen atoms of acesulfamato ligand and hydrogen atoms of aqua ligands and also both intermolecular and intramolecular interaction (hydrogen bonding) between carbonyl oxygen atoms of acesulfamato and hydrogen atoms of aqua ligands. Some complex structures stated have thermochromic, solvatochromic and ionochromic properties depending on deaquation [12]. Also, the alkaline earth metal cation complexes with organic ligands were studied and investigated their bonding parameters by lots of researcher [13-18]

The importance of studies related with transition metal complexes of nicotinamide acting as vitamin B_3 and used in drug preparation has been increased recently. As a result of spectral investigation of complexes between nicotinamide and these metals, it was determined that it has ability to bind as monodentate ligand through pyridine nitrogen. [19-21].

MATERIALS AND METHODS

In the synthesis of complex, $Ca(ClO_4)_2.4H_2O$ and $Sr(ClO_4)_2$ were obtained from Aldrich, $Mg(ClO_4)_2.2H_2O$ and $Ba(ClO_4)_2$ were obtained from Merck, potassium acesulfame (Kacs, Kace), and nicotinamide were obtained from Fluka, and ethanol was obtained from Aldrich. Pure water was used as a solvent.

For the synthesis of complex, metal perchlorate and potassium acesulfame were used sufficient amount at molar ratio of 1:2 (typically molar ratio of 0.01: 0.02) and dissolved within separate beaker. Resulting solutions were stirred slowly and, as shown in the following reaction, precipitation of $KClO_4$ salt and the formation of complexes were provided.

$$M(ClO_4)_2 + 2\ K(acs) \rightarrow 2\ KClO_4 + [M(acs)_n(H_2O)_x]$$

The mixed ligand complexes were obtained after synthesis of $[M(acs)_n(H_2O)_x]$ complex via mixing of both aqueous solutions of each component (metal, nicotinamide) with metal/nicotinamide ratio of 1:2.

$$[M(acs)_n(H_2O)_x] + 2\ \text{nicotinamide} \rightarrow [M(acs)_n(H_2O)_y(na)_m]$$

8 complexes having the following formula were synthesized by these methods:

$[Mg(H_2O)_4(na)_2](acs)_2$, $[Ca(H_2O)_6(na)_2](acs)_2$, $C_8H_{10}SrN_2O_9S_2$, $Ba(H_2O)_7(na)_2](acs)_2$

Resulting complexes were characterized by analytical

Table 1. Data obtained from elemental analysis of complexes

		%C	%H	%N
Compounds	Molecular Weight (g/mol)	Experimental (Theoretical)	Experimental (Theoretical)	Experimental (Theoretical)
$[Mg(H_2O)_4(na)_2](acs)_2$	664,83	35,84(36,13)	5,67(4,25)	12,69(12,64)
$[Ca(H_2O)_6(na)_2](acs)_2$	717,31	33,16(33,49)	4,99(4,5)	10,91(11,72)
$[Sr(H_2O)_7(na)_2](acs)_2$	782,15	31,24(30,7)	4,21(4,4)	9,66(10,75)
$[Ba(H_2O)_7(na)_2](acs)_2$	831,87	27,65(28,88)	4,11(4,12)	8,67(10,1)

methods such as IR spectroscopy, X-ray single crystal diffraction, thermal analysis, melting point determination, mass spectroscopy and elemental analysis methods.

RESULTS AND DISCUSSION

Elemental analysis results obtained for metal-aqua-nicotinamide-acesulfame salt-type mixed ligand complexes are given by Table 1. Being in harmony with the calculated values of the experimental results obtained by elemental analysis supports the validity of the proposed formula.

Melting points of complexes were determined by heating at the temperature interval of 20-300°C with 5°C/min heating rate using Stuart SMP30 device. As can be seen from Table 2, potassium acesulfame melts at 225°C, whereas it was observed that salt-type complex structure decomposes accompanied by darkening without melting.

Table 2. Melting points of potassium acesulfame and complexes

Compound	Temp. (°C)	Observations
Potassium Acesulfame	225	Melting
$[Mg(H_2O)_4(na)_2](acs)_2$	121-132	Darkening/Decomposition
$[Ca(H_2O)_6(na)_2](acs)_2$	210-235	Darkening /Decomposition
$[Sr(H_2O)_7(na)_2](acs)_2$	257-269	Darkening /Decomposition
$[Ba(H_2O)_7(na)_2](acs)_2$	206-250	Darkening /Decomposition

Infrared Spectra

As can be seen from FT-IR spectra given by Figure 2 for salt-type complex compounds synthesized, there are O-H stretching vibrations at 3565 and 3431 cm^{-1} for the compound $[Mg(H_2O)_4(na)_2](acs)_2$. There are stretching vibrations observed at 3369 and 3303 cm^{-1} for N-H, at 3211 cm^{-1} for aromatic C-H and at 3075 cm^{-1} for aliphatic C-H. Vibrations for carbonyl (C=O) groups were observed at $1688_{(amide)}$ and $1651_{(acs)}$ cm^{-1}. N-H group bending and C=C stretching vibrations were observed at 1599 and 1550 cm^{-1}, respectively. Asymmetric and symmetric stretching vibrations for sulphonyl group were observed at 1311 and 1169 cm^{-1}, respectively. Asymmetric and symmetric stretching vibrations for C-N-S were observed at 939 and 1396 cm^{-1}, respectively. Metal-oxygen and metal-nitrogen bonds were observed in order of at 517 and 560 cm^{-1}.

Sharp bands observed at 3518 and 3423 cm^{-1} for $[Ca(H_2O)_6(na)_2](acs)_2$ complex are belongs to O-H stretching vibrations. Stretching vibrations for N-H (NH_2 group) can be seen at 3368 and 3296 cm^{-1}. Aromatic and aliphatic C-H stretching vibrations can be observed at 3060 and 2960 cm^{-1}, respectively. Another data obtained from spectra are stretching vibration of the carbonyl group at $1678_{(amide)}$ and $1650_{(acs)}$ cm^{-1}, N-H bending vibrations at 1600 cm^{-1}, C=C vibrations at 1578 cm^{-1}. Moreover, asymmetric and symmetric stretching vibrations for sulphonyl and C-N-S groups are observed at 1270 and 1176 cm^{-1}, and at 936 and 1385 cm^{-1}, respectively.

It was determined that $[Sr(H_2O)_7(na)_2](acs)_2$ complex also gives sharp O-H stretching vibration bands at 3577 and 3520 cm^{-1}. The bands observed at 3370 and 3290 cm^{-1} correspond to N-H stretching vibration. Aromatic and aliphatic C-H stretching vibrations are observed at 3143-3070 and 2824 cm^{-1}, respectively. Sharp bands observed at $1706_{(amide)}$, 1675 and $1656_{(acs)}$ are belongs to carbonyl

Table 4.2. Characteristic FT-IR vibration values (cm^{-1}) for Acesulfame/Nicotinamide-Metal complexes (cm^{-1}).

Compound	ν(OH)	ν_{ger}(NH)	ν(C-H)	ν(C=O)	ν_{eg}(NH)	ν(C=C)	$\nu_{as}(SO_2)$	$\nu_s(SO_2)$	ν_s(CNS)	ν_{as}(CNS)	M-O/M-N
$[Mg(H_2O)_4(na)_2](acs)_2$	3565 3431	3369 3303	3211 3075	1688 1651	1599	1550	1311	1169	1396	939	517/560
$[Ca(H_2O)_6(na)_2](acs)_2$	3518 3423	3368 3296	3060 2960	1678 1650	1600	1579	1270	1176	1385	936	520/557
$[Sr(H_2O)_7(na)_2](acs)_2$	3577 3520	3370 3300	3142 2824	1675 1656	1610	1588	1251	1160	1358	936	518/570
$[Ba(H_2O)_7(na)_2](acs)_2$	3592 3527	3367	3110 2923	1676 1652	1600	1558	1320	1176	1368	941	523/563

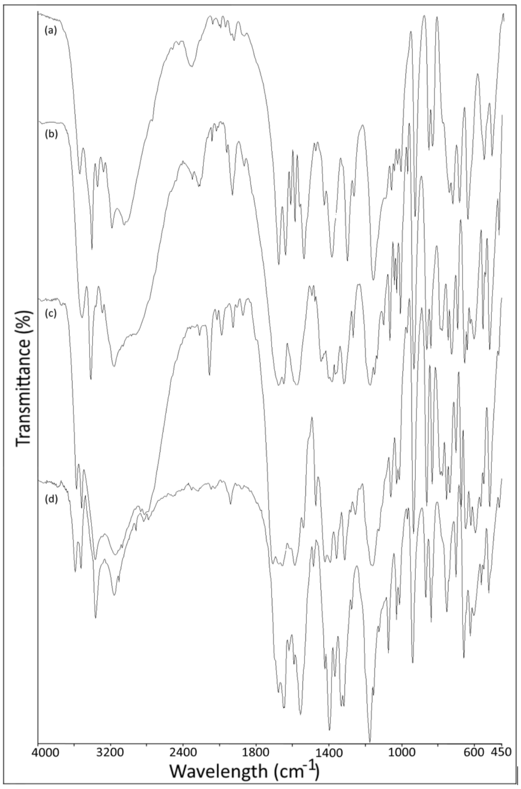

Figure 2. FT-IR spectra for a) $[Mg(H_2O)_4(na)_2](acs)_2$; b) $[Ca(H_2O)_6(na)_2](acs)_2$; c) $[Sr(H_2O)_7(na)_2](acs)_2$; d) $[Ba(H_2O)_7(na)_2](acs)_2$ complexes.

(C=O) group stretching vibrations. Bending vibration of NH_2 group and C=C double bond stretching vibration are observed at 1610 and 1588 cm^{-1}, respectively. Asymmetric and symmetric stretching vibrations for sulphonyl (SO_2) and C-N-S group are observed at 1251 and 1160 cm^{-1}, and 936 and 1358 cm^{-1}, respectively.

According to the FT-IR spectra analyzed for $[Ba(H_2O)_7(na)_2](acs)_2$, sharp bands observed at 3592 and 3527 cm^{-1} may be attributed to O-H stretching vibration. While one of the bands due to N-H stretching belongs to NH_2 can be observed at 3367 cm^{-1}, other band could not be seen due to the expansion of the aromatic C-H band. C-H stretching vibrations can be observed at 3161-3110 (aromatic) and 2923 (aliphatic) cm^{-1}. Stretching vibration of Carbonyl (C = O) group can be seen at $1676_{(amide)}$ and $1652_{(acs)}$ cm^{-1}. There are other vibrations observed for N-H bending at 1600 cm^{-1}, for C=C double bond stretching at 1558 cm^{-1}, asymmetric and symmetric stretching for sulphonyl group at 1320 and 1176 cm^{-1}. Asymmetric and symmetric stretching vibration bands for C-N-S groups were observed at 941 and 1368 cm^{-1}, respectively.

Thermal Analysis

Figure 3a shows thermal analysis curves for $[Mg(H_2O)_4(na)_2](acs)_2$ complex. The complex having four

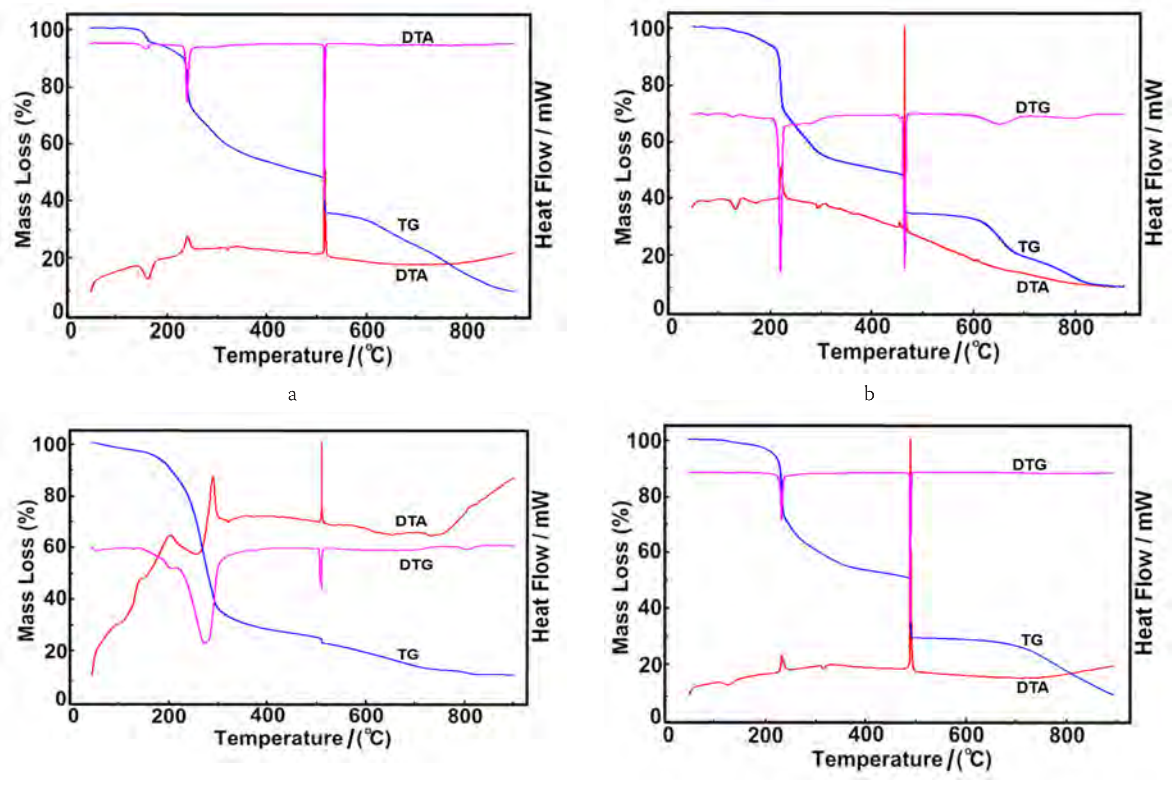

a

b

c

d

Figure 3. TG/DTG and DTA curves for a) $[Mg(H_2O)_4(na)_2](acs)_2$; b) $[Ca(H_2O)_6(na)_2](acs)_2$; c) $[Sr(H_2O)_7(na)_2](acs)_2$; d) $[Ba(H_2O)_7(na)_2](acs)_2$ complexes

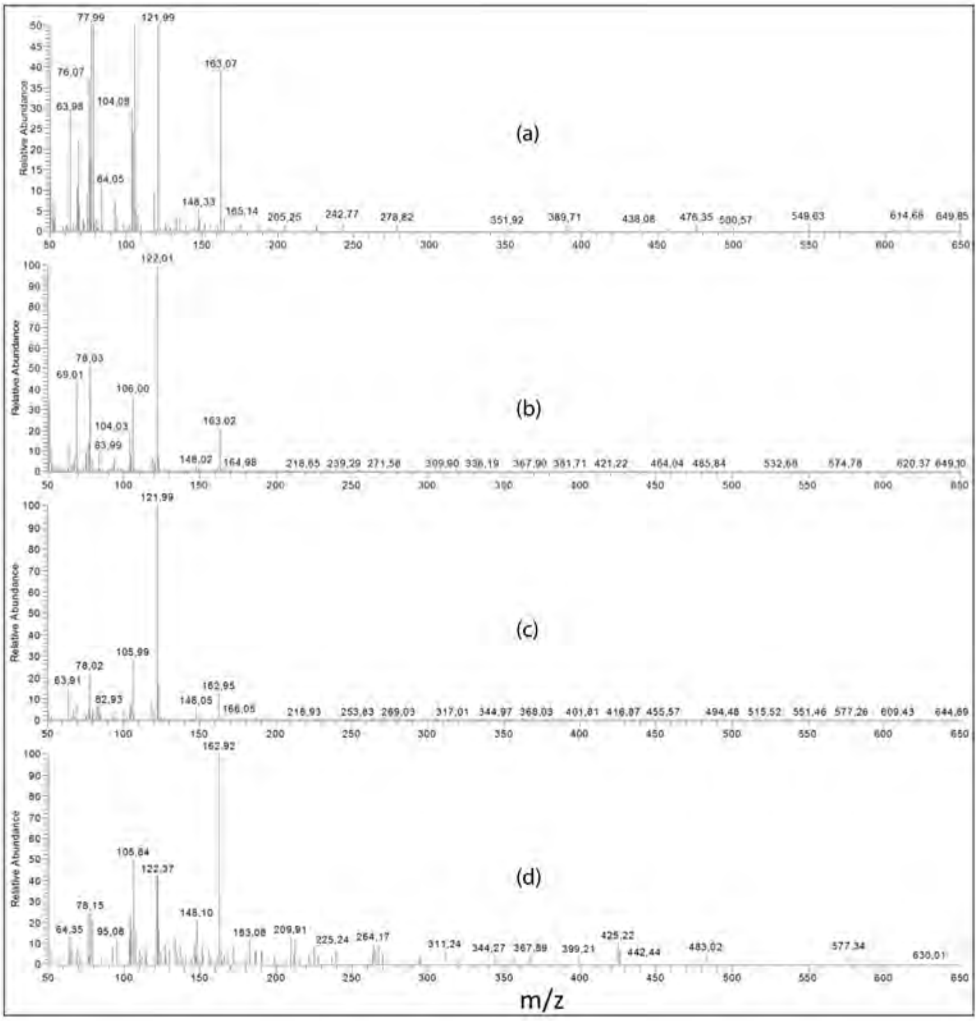

Figure 4. Mass spectra for a) $[Mg(H_2O)_4(na)_2](acs)_2$; b) $[Ca(H_2O)_6(na)_2](acs)_2$; c) $[Sr(H_2O)_7(na)_2](acs)_2$; d) $[Ba(H_2O)_7(na)_2](acs)_2$ complexes.

moles aqua ligand within its structure was subjected to two-step deaquation. 5.38% and 5.32% mass loss observed at the temperature range of 20-150°C and 150-214°C, respectively, are due to the leaving of two moles of aqua ligands (Theoretical: 5.4%). Next step is the leaving of nicotinamide ligands one by one. 18.43% and 18.34% mass losses observed at the temperature range of 214-234°C and 234-388°C, respectively, are due to the leaving of one mole of nicotinamide ligand (Theoretical: 18.37%). At this point, existence of $Mg(acs)_2$ was considered. The resulting compound was degraded at high temperature, and converted to MgO compound with leaving of organic part (acs) (Experimental: 5,97-Theoretical: 6.02%). Leaving of acesulfamate ions was corresponded to experimental mass of 45.6%. This value is theoretically 46.4%.

According to the thermal analysis curve belonging to $[Ca(H_2O)_6(na)_2]$ $(acs)_2$ complex given by Figure 3b, decomposition of structure was happened at two stages. The first stage is occurred at deaquation range corresponding to leaving of six mol aqua ligand (at 15-220°C range, Experimental: 14.7%, Theoretical: 14.2%), the second stage is the leaving of nicotinamide ligands (at 220-405°C range, Experimental: 33.97%, Theoretical: 34.05%). The final product corresponds to CaO compound (Experimental: 8.8%, Theoretical: 7.8%). From DTG curve, sharp peaks were observed where weight loss was happened. Therefore, it is evident for both the aqua and nicotinamide ligands are leaving from the complex structure very quickly.

Decomposition of $[Sr(H_2O)_7(na)_2](acs)_2$ structure takes place at two stages (Figure 3c). The first stage is deaquation. 7 moles of aqua ligand leave from the structure at the temperature range of 69-204°C (Experimental: 16.37% - Theoretical: 16.13%). The second stage is the leaving of nicotinamide which is the other neutral ligand. Two moles of nicotinamide are leaving from the structure at the temperature range of 204-255°C (Experimental: 31.26% - Theoretical: 31.23%). It is estimated that the final product is SrO compound. Broaden DTG curve shows that the leaving ligands are moving away from the structure slowly.

Thermal analysis curve for $[Ba(H_2O)_7(na)_2](acs)_2$ can be seen at Figure 3d. Complex decomposes at three steps. First stage of the decomposition is deaquation. Seven moles of aqua ligand are leaving at the temperature range of 25-223°C (Experimental: 15.05-Theoretical: 15.15%). The next stage of the decomposition is the leaving of 2 moles nicotinamide ligands at one step at the temperature range of 223-387°C (Experimental: 29.17% - Theoretical: 29.36%). At this stage, $Ba(acs)_2$ salt is formed. This salt was began to decompose at around 650°C. BaO compound is thought to be the final product (Experimental: 13.40% - Theoretical: 18.40%). From the DTG curve, there are sharp peaks where the weight loss was observed. This means that the leaving groups were moved away from the structure very quickly.

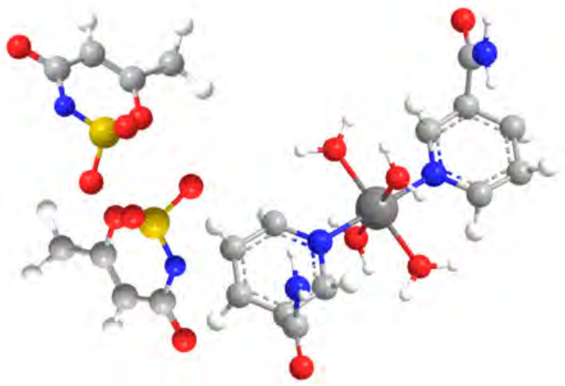

Figure 5. Proposed structure of $[Mg(H_2O)_4(na)_2](acs)_2$ complexes.

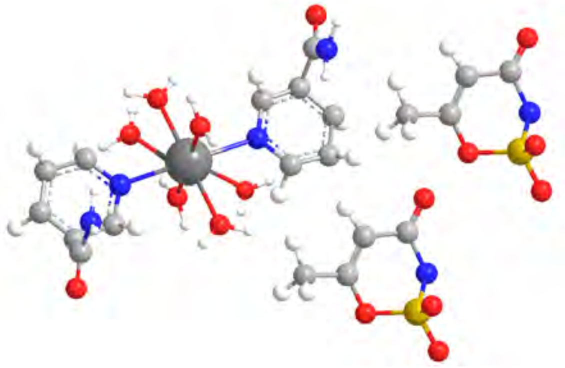

Figure 6. Proposed structure of $[Ca(H_2O)_6(na)_2](acs)_2$ complexes.

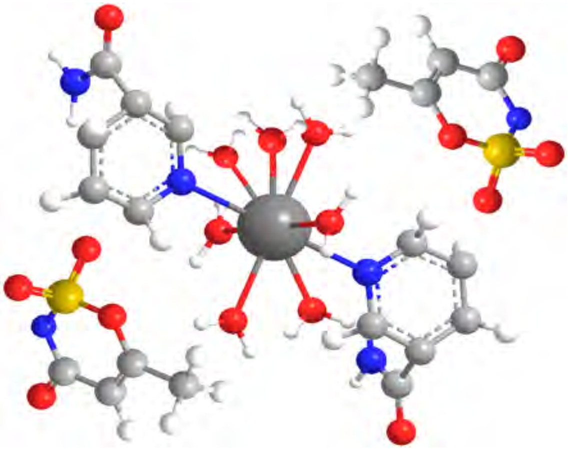

Figure 7. Proposed structure of $[Sr(H_2O)_7(na)_2](acs)_2$ and $[Ba(H_2O)_7(na)_2](acs)_2$ complexes.

Mass Spectra

Mass spectra for $[Mg(H_2O)_4(na)_2](acs)_2$, $[Ca(H_2O)_6(na)_2](acs)_2$, $[S(H_2O)_7(na)_2](acs)_2$ and $[Ba(H_2O)_7(na)_2](acs)_2$ complexes are given at Figure 4a, 4b, 4c and 4d, respectively. Moderate peaks with m/z ratio of 63.98; 64.00; 63.91 and 64.35 may be attributed to the leaving of SO_2 group. Peaks reason of which thought to be leaving of nicotinamide from metal-nicotinamide-acesulfame complexes are observed at 121.99, 122.01, 121.99 and 122.37 cm^{-1}, respectively. These peaks observed at mass spectra offer strong evidence for incorporation of ligands into coordination compounds.

CONCLUSIONS

Within the structure of complex, estimated 3D structure of which was given at Figure 5, 2 nicotinamide ligands were coordinated to Mg^{II} ions at trans position. For complex with octahedral geometry, while the other four coordinate was provided with aqua ligands, acesulfamato ions acted as counter-ions. From thermal analysis of the complex, it can be concluded that the decomposition was taken place through in order of leaving of two moles aqua, two moles aqua, a mole nicotinamide and a mole nicotinamide.

While Ca^{II} metal cation, coordination of which was estimated as 8, completes coordination through 2 moles of nicotinamide ligand and 6 moles of aqua, +2 charged cation was balanced with 2 moles acesulfamate anions acting as counter ion (Figure 6).

Coordinations of complexes formed by isostructural Sr^{II} and Ba^{II} metal cations was completed to 9 through seven moles of aqua and 2 moles of nicotinamide ligands (Figure 7). The charge balance of metals was ensured through mono-anionic acesulfamate anions located outside of coordination sphere as done in other complex structures. Conductivity tests were performed to determine whether acesulfamate anions act as counter-ion for all complexes, and structures are salt-type complex structures.

REFERENCES

1. Clauss K, Jensen H. Oxatiazinon dioxides– a new group of sweetening agents. Angewandte Chemie International Edition in English 12 (1973) 869–942.
2. Hodgin G. The history, synthesis, metabolism and uses of artificial sweeteners. Atlanta, GA: Emory Center for Interactive Teaching, Emory University, 2002.
3. Sertçelik M, Delibaş NÇ, Necefoğlu H, Hökelek T. Diaquabis(4–formylbenzoato–κO ^{1}) bis(nicotinamide–κN ^{1})nickel(II) Acta Crystallographica Section E 68 (2012) 946-947.
4. Şahin O, Büyükgüngör O, Köse DA, Necefoglu H. trans–diaquabis(3–hydroxybenzoato–κO1)bis(nicotinamide–κN1) copper(II). Acta Crystallographica Section C 63 (2007) 510-512.
5. Köse DA, Necefoğlu H, İçbudak H. Synthesis and characterization of the nicotinamide–acetylsalicylato complexes of Co(II), Ni(II), Cu(II) and Zn(II). Hacettepe Journal of Biology and Chemistry 35(2) (2007) 123–128.
6. Köse DA, Gökçe G, Gökçe S, Uzun İ. bis(N,N–diethylnicotinamide) p–chlorobenzoate complexes of Ni(II), Zn(II) and Cd(II). Synthesis and characterization. Journal of Thermal Analysis and Calorimetry 95(1) (2009) 247-251.
7. Köse DA, Öztürk B, Şahin O, Büyükgüngör O. Mixed ligand complexes of coumarilic acid/nicotinamide with transition metal complexes. Synthesis and structural investigation. Journal of Thermal Analysis and Calorimetry 115 (2014) 1515-1524.
8. Bulut A, İçbudak H, Sezer G, Kazak C. bis(acesulfamato–κ^{2}N^{3}, O^{4}) bis (2–aminopyirimidine – κN^{1}) copper(II). Acta Crystallographica Section C 61 (2005) m228–m230.
9. İcbudak H, Heren Z, Köse DA, Necefoglu H. bis(Nicotinamide) and bis(N,N–diethylnicotinamide)p–hydroxybenzoate complexes of Ni(II), Cu(II) and Zn(II). Spectrothermal studies. Journal of Thermal Analysis and Calorimetry 76 (2004) 837-851.
10. İçbudak H, Bulut A, Çetin N, Kazak C. bis(acesulfamate) tetraaquacobalt(II). Crystal Structure Communications C61 (2005) 1–3.
11. İçbudak H, Heren Z, Uyanık A, Odabaşoğlu M. Prediction of the decomposition pathway of diaquabis(N,N′–dimethyl–1,2–ethanediamine)nickel(II) acesülfamate by thermal and mass spectroscopic data. Journal of Thermal Analysis and Calorimetry 82(2) (2005) 303–306.
12. Çetin N. Synthesis, structure, spectroscopic, thermal, chromothropik properties of some acesulfame complexes with transition metals. Master's Thesis, Ondokuz Mayıs University, Science Institute, Samsun, 2005.
13. Wojtczak WA, Fleig PF, Hampden–Smith M. A review of group 2(IIA)(Ca,Sr,Ba) metal–organic compounds as precursors for chemical vapour deposition. Advances in Organometallic Chemistry 40 (1996) 215–340.
14. Murugavel R, Kumar P, Walawalkar MG, Mathialagan R. A double helix is the repeating unit in a luminescent calcium 5–aminoisophthalate supramolecular edifice with water–filled hexagonal channels. Inorganic Chemistry 46(17) (2007) 6828–6830.
15. Cates MS, Teodoro ML, Phillips GNJr. Molecular mechanisms of calcium and magnesium binding to parvalbumin. Biophysical Journal 2002, 82, 1133–1146.
16. Matsumura H, Shiba T, Inoue T, Harada S, Kai Y. A novel mode of target recognition suggested by the 2.0 Å structure of holo S100B from bovine brain. Structure 6 (1998) 233-241.
17. Murugavel R, Karambelkar VV, Anantharaman G, Walawalkar MG, Synthesis, spectral characterization and structural studies of 2–aminobenzoate complexes of divalent alkaline earth metal ions: X–ray crystal structures of [Ca(2–aba)$_2$(OH$_2$)$_3$]∞, [{Sr(2–aba)$_2$(OH$_2$)$_2$}·H$_2$O]∞, and [Ba(2–aba)$_2$(OH$_2$)]∞ (2–abaH=2–NH$_2$C$_6$H$_4$COOH). Inorganic Chemistry 39(7) (2000) 1381–1390.
18. Zou JH, Cui HJ, Xu B, Zhu DL, Li QY, Yang GW, Hua YC. Three new alkaline earth coordination compounds based on 5–(2–pyrimidyl)tetrazole–2–acetic acid. Inorganica Chimica Acta 423 (2014) 430–434.
19. Edebalı S. Synthesis and structural properties of complexes of zinc p–florine and p–bromine benzoate with nicotinamide, iso–nicontinamide and N,N′–dietihylnicotinamide. Master's Thesis, Kafkas University, Science Institute, Kars, 2007.
20. Köse DA, Necefoglu H, Şahin O, Büyükgüngör O, Synthesis, structural, spectroscopic characterization, and structural comparison of 3–hydroxybenzoate and nicotinamide / N,N–diethylnicotinamide mixed ligand complexes with Zn(II). Journal of Thermal Analysis and Calorimetry 110 (2012) 1233–1241.
21. Köse DA, Necefoglu H, Şahin O, Büyükgüngör O. Synthesis, spectral, thermal and structural study of monoaquabis (acetylsalicylato–κ–O)bis(nicotinamide–κ–N) copper(II). Journal of Chemical Crystallography 41 (2011) 297–305.

NATIONAL & INTERNATIONAL SCIENTIFIC EVENTS

Tms 2015 144th Annual Meeting & Exhibition
Venue: Orlando, FL, USA
Location: Orlando, FL, USA

BEGINS: March 15, 2015
Ends: March 19, 2015

16th IUMRS-IC
Venue: Suntec, Singapore
Location: Singapore

BEGINS: June 28, 2015
Ends: July 03, 2015

Frontiers of Quantum and Mesoscopic Thermodynamics 2015
Venue: Orea Hotel Pyramida
Location: Prague, Czech Republic

BEGINS: Jul 27, 2015 08:00 AM
Ends: Aug 01, 2015

2015 MRS Spring Meeting & Exhibit
Venue: San Francisco, California
Location: USA

BEGINS: April 06, 2015
Ends: April 10, 2015

15th International Nutrition & Diagnostics Conference
Venue: Hotel DAP
Location: Prague, Prague, Czech Republic

BEGINS: Oct 05, 2015
Ends: Oct 08, 2015

2015 E-MRS Spring Meeting and Exhibit
Venue: Lille
Location: France

BEGINS: May 11, 2015
Ends: May 15, 2015

6th International Conference on Experiments/Process/System Modeling/Simulation/Optimization
Venue: DIVANI CARAVEL HOTEL
Location: Athens, Greece

BEGINS: Jul 08, 2015
Ends: Jul 11, 2015

CMFF'15 Conference on Modeling Fluid Flow

Venue: Danubius Hotel Gellert
Location: Budapest, Hungary

BEGINS: Sep 01, 2015
Ends: Sep 04, 2015

International Conference on Biotechnology, Nanotechnology Environmental Engineering
Venue: Arnoma Hotel Bangkok
Location: Bangkok, Thailand

BEGINS: Apr 22, 2015
Ends: Apr 23, 2015

International Conference on Mechanical Engineering (MEN 2015)
Venue: Bangalore,India
Location: Bangalore, India

BEGINS: Mar 28, 2015
Ends: Mar 29, 2015

International Conference on Biosciences Research (ICBR 2015)
Venue: Suncity Exclusive Hotels Ltd
Location: Awka, Anambra, Nigeria

BEGINS: May 25, 2015
Ends: May 29, 2015

CDSR 2015 - 2nd The International Conference of Control, Dynamic Systems, and Robotics
Venue: University of Ottawa
Location: Ottawa, Ontario, Canada

BEGINS: May 07, 2015
Ends: May 08, 2015

HJSE Official Journal of Graduate School of Natural & Applied Sciences Volume 1, Issue 1, 2014 www.hjse.hitit.edu.tr

JOURNAL OF SCIENCE & ENGINEERING
HITTITE